STUDY OF TURBULENT SPHERICAL FLAMES IN A RECONFIGURABLE FAN-STIRRED FLAME BOMB

A Dissertation

by

ANÍBAL MORONES RUELAS

Submitted to the Office of Graduate and Professional Studies of
Texas A&M University
in partial fulfillment of the requirements for the degree of

DOCTOR OF PHILOSOPHY

Chair of Committee,	Eric L. Petersen
Committee Members,	Gerald L. Morrison
	Waruna D. Kulatilaka
	Adonios N. Karpetis
Head of Department,	Andreas A. Polycarpou

December 2018

Major Subject: Mechanical Engineering

ABSTRACT

Turbulent combustion is a very active and challenging research topic. A spherically expanding flame immersed in a turbulent field is one way to gain fundamental insight on the effect of turbulence in combustion. This kind of experiment is conducted inside a fan-stirred flame bomb, but there is only a handful of these devices around the globe. The list is even shorter if demanding conditions are to be tested, i.e. high pressure, high temperature and intense turbulence. A new fan-stirred flame bomb was designed and built to address this shortage.

Existing fan-stirred flame bombs were studied first to learn their salient characteristics. This literature review was then used as guidance in the design of turbulence generation elements. A few options of impellers were explored. The flow field produced by the chosen impeller was measured with Laser Doppler Velocimetry (LDV). A detailed exposition of the vessel engineering ensued.

Before turbulent experiments were attempted, a validation of the rig accuracy and worthiness was made. The setup demonstrated excellent repeatability and agreement with benchmarks. Finally, a demonstration of the new apparatus was made by testing a lean mixture of syngas. The experiment matrix using hydrogen and H_2/CO mixtures included three levels of pressure (1, 5, and 10 bar) and three levels of turbulence fluctuation rms (1.4, 2.8, and 5.5 m/s). General trends of the effect of turbulence were in line with expectation, but not enough information was obtained to gain insight on the role of pressure.

DEDICATION

To my parents.

ACKNOWLEDGEMENTS

I will be forever grateful for the guidance received during the last 5 years at Dr. Petersen's laboratory. Thanks to him, I enjoyed being part of a community that is at the forefront of combustion science research.

Special thanks must go to FESCO Inc. and James Gallego for their help testing the bomb hydrostatically. Their specialized hardware and generous donation of time ensured the bomb has a sound design and competent construction.

Dr. Miladin Radovic's expert eye troubleshot and diagnose a stress concentration issue in the window cell. His recommendations and observations were incorporated in the final design. Many thanks to him.

Garrick Garza's advice on machining and manufacturability is greatly appreciated and acknowledged.

I must thank my dear wife, Liliana Yadira Nolasco Isaula. She deserves credit for this degree almost as much as I do.

CONTRIBUTORS AND FUNDING SOURCES

Contributors

This work was supervised by a dissertation committee consisting of Professor Eric L. Petersen, Gerald L. Morrison and Waruna D. Kulatilaka of the Department of Mechanical Engineering and Professor Adonios N. Karpetis of the Department of Aerospace Engineering.

The high speed schlieren images were post-processed with the edge finding code written by Travis Glen Sikes.

Travis Glen Sikes and Mattias Turner performed some of the experiments presented here.

Víctor León designed and 3D-printed the radial impeller shown in Figure 11.

All other work conducted for the dissertation was completed by the student independently.

Funding Sources

This work was made possible in part by the U.S. Department of Energy's University Turbine Systems Research (UTSR) program under Grant Number DE-FE0011778 and the National Science Foundation under Grant Number EEC-1263196.

NOMENCLATURE

α	Thermal diffusivity $\left(\alpha = k/\rho c_p\right)$, m^2/s
D	Mass diffusivity m^2/s
LDV/LDA	Laser Doppler Velocimetry / Anemometry
mpg	Miles Per Gallon
NOx	Nitrogen Oxides
PIV	Particle Image Velocimetry
PLA	Polylactic Acid (3D printing filament)
P-LIF	Planar Laser Induced Fluorescence
ρ	density, kg/m^3
rms	Root Mean Square
rpm	Revolutions per minute
S_T	Turbulent Flame Speed
TFB	Turbulent Flame Bomb; the apparatus discussed in this work
$\tilde{u}$	Instantaneous value of speed
u'	Turbulence fluctuation
U	Time averaged speed.

TABLE OF CONTENTS

Page

LIST OF FIGURES

Page

LIST OF TABLES

Page

INTRODUCTION

The rigorous study of the effect of turbulence in combustion is fairly recent [1] despite how ubiquitous and immemorial combustion applications are. In his seminal work, Damköhler offered a few reasons to this tardiness: the lack of a quantitative description of turbulence, which only existed for one simple case at the time; and the disconnect between the communities interested in the study of combustion and turbulence. Damköhler insisted that any attempt to comprehend the effect of turbulence on flame propagation must start with numerical data on the turbulence.

While there is significant progress on the understanding of fundamental aspects turbulent combustion and the underlying physical constitutive relations are known, namely, conservation of species, mass, energy, and momentum, the sheer number of scales and species to be solved is computationally prohibitive for the foreseeable future [2]. There is now a sizeable combustion community working on many fronts to develop a predictive model that can handle relatively unstudied chemical compositions at high pressures and Reynolds numbers [3].

The development of models from canonical flames and idealized laboratory conditions may take longer to impact the technology of practical applications, as opposed to those efforts channeled to improve the performance of a specific device. However, simpler experiments that are amenable for both meticulous measurements and high fidelity modeling provide a more sound approach to build fundamental understanding [4].

The search of a better understanding of turbulent combustion is not driven by purely academic interests. Environmental concerns and resource depletion, among other

factors, are pushing combustion applications to improve performance while reducing pollutant emission. An specific example from the automotive industry illustrates: current regulation for model year 2025 compels vehicle manufacturers to average 54.5 miles per gallon (mpg) among their overall fleet offer [5]. This is an ambitious goal considering that the mileage of best-selling vehicle in the USA averages roughly only half that. Unconventional fuels, novel strategies, and more demanding operating conditions are being considered to close the performance gap [3]. A better understanding of turbulent combustion could help to cope with this exigence.

Spherical flame experiments can support the advance of turbulent combustion science by producing measurements for conditions and species that are outside the borders of current numerical simulation capabilities or for which little is known in literature. Worldwide, there are few fan-stirred flame bombs that are capable of testing conditions higher than ambient temperature and pressure and that are also able to produce turbulent flow fields that are relevant to practical devices. Table 1 offers a summary of the devices found in literature and Figure 1 displays the variety of shapes and sizes encountered in fan-stirred flame bombs.

There are bombs that operate at elevated pressure. An extreme example is the rig built by Weiß machined out of single piece of steel (ID 6 in Table 1). Some others can withstand temperature above ambient and are better suit for the study of liquid fuels. Few can stir with a turbulence fluctuation rms greater than 5 m/s. Only one facility combines all three capabilities and stands out in green in Figure 2 (ID 3 in Table 1).

Table 1 Fan-stirred flame bomb survey.

ID	Institution	Format & dimensions mm	Internal volume liters	Max. temp. K	Max. pressure bar	Turb. rms m/s
1	U Leeds 1st gen. [6]	Cylinder ⌀ 305, L 305	22.3	300	1	16
2	GM/UMI [7-9]	Spheroid ⌀ 260, L 265	10.6	300	5	2.5
3	U Leeds 2nd gen. [10]	Sphere ⌀ 380	28.73	600	15	11.9
4	UMI [11]	Spheroid ⌀ 102	0.8	300	1	1.8
5	Kyushu U [12, 13]	3 intersecting cylinders ⌀ 265	35.0	300	10	3.2
6	KIT [14, 15]	3 intersecting cylinders ⌀ 80, L 190	2.28	300	70	3.5
7	Taiwan NCU [16-19]	Cruciform ⌀ 120, 245, L 600, 420	26.6	300	10	8.3
8	Princeton [20, 21]	Cylinder ⌀ 114, L 127	1.29	300	30	6.0
9	TAMU 1st gen.[22, 23]	Cylinder ⌀ 305, L 356	25.9	300	1	1.5
10	U d'Orléans [24]	Sphere ⌀ 200	4.2	473	10	2.8
11	CNRS-ICARE [25]	Sphere ⌀ 563	93.4	573	20	3.7
12	This work	Spheroid ⌀ 356, L 406	33.8	473	10	5.5

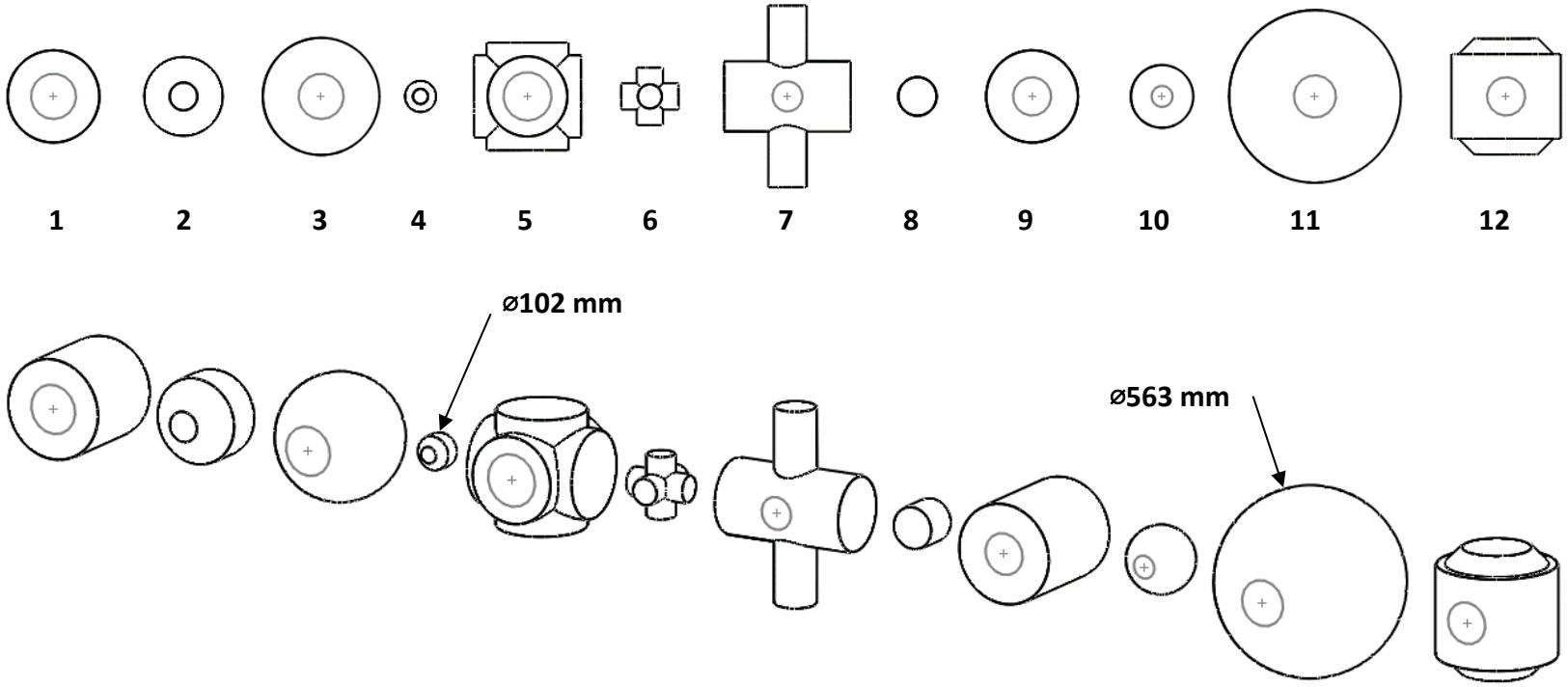

Figure 1 Interior volume of fan-stirred flame bombs. The ID number matches the order listed in Table 1.

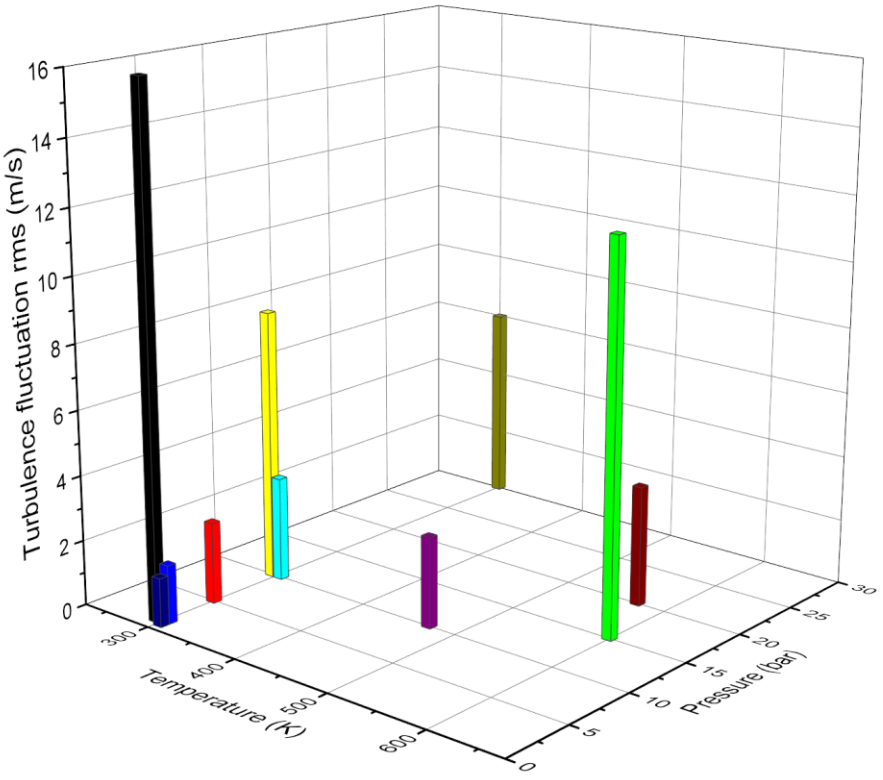

Figure 2 Domain of operating conditions of flame bombs listed in Table 1. The entry of Karlsruhe Institute of Technology has been omitted.

A new apparatus could help bridge the gap in testing facilities. The objective of this thesis was to design and build a fan-stirred flame bomb for the study of turbulent combustion at elevated pressure and temperature. A detailed description of the device design is offered first, followed by a description the turbulence characterization. Then, a study of syngas is presented to demonstrate the capabilities of newly developed device. The results are discussed, and recommendations for future work are offered.

STIRRING OPTIMIZATION

The Turbomachinery Laboratory at Texas A&M University has successfully built and operated two high-pressure laminar flame bombs and one fan-stirred flame bomb. The present work will focus on the optimization of stirring and other unique features of the turbulent flame bomb and refer the reader to previous documents for details shared with quiescent flame bombs [26-28].

Flow characterization methods and conventions

The turbulent field produced by the stirring fan was scanned with a 2-dimensional solid state LDV system in a similar fashion to [23]. The laser velocimeter measures two orthogonal components at one "point" in space. Strictly speaking, the measurements belong to a finite space called probe volume, not to a point, but this is fairly small. The probe volume is the tridimensional ellipsoid defined by the crossing of two laser beams. Every time[1] that a particle crosses the fringe pattern created inside the probe volume, a velocity measurement is made. The probe volume dimensions for the emitting optics used in this study are 3.3-3.5 mm long with a diameter of 161-170 μm. If the region of interest is systematically scanned with these "point" measurements, a statistically stationary ensemble of the flow field can be constructed.

The LDV unit employed combines the emitting and receiving optics in one device. The LDV unit has two solid state lasers (532 and 561 nm) rated at 300 mW each. The

[1] Not each and every particle that crosses the probe volume renders a valid signal. A valid frequency burst of scattered light has to meet certain parameters.

stand-off lens chosen for the emitting optics forms probe volumes 512.3 mm away from the unit. The device collects the backscattered light of particles crossing the probe volume.

A 2-dimensional LDV acquisition produces a pair of orthogonal velocity time series, which will be called $\tilde{u}(\mathbf{x},t)$ and $\tilde{w}(\mathbf{x},t)$. In the convention adopted here, *t* is the time stamp and $\mathbf{x}$ denotes the position vector $\mathbf{x} = x\hat{\mathbf{i}} + y\hat{\mathbf{j}} + z\hat{\mathbf{k}}$; where the origin of the coordinate system coincides with the center of the bomb. Here is also established that $\tilde{w}(\mathbf{x},t)$ should point along the cylindrical axis of the vessel in Figure 3 and $\tilde{u}(\mathbf{x},t)$ is aligned with the X axis of the same figure. Therefore, $\tilde{u}(\mathbf{x},t)$ and $\tilde{w}(\mathbf{x},t)$ are components of the tridimensional velocity $\tilde{\mathbf{a}}(\mathbf{x},t)$ so that $\tilde{\mathbf{a}}(\mathbf{x},t) = \tilde{u}(\mathbf{x},t)\hat{\mathbf{i}} + \tilde{v}(\mathbf{x},t)\hat{\mathbf{j}} + \tilde{w}(\mathbf{x},t)\hat{\mathbf{k}}$. The notation implemented in this work will use tilde ~ to denote instantaneous, **bold** to distinguish vectors, and hat ^ for the orthogonal unity vectors along the *X*, *Y*, and *Z* directions.

The $\tilde{v}(\mathbf{x},t)$ component along the line of sight of the LDV transceiver, i.e. along the *Y* axis in Figure 3, cannot be resolved by this 2-dimensional laser system. In other words, the setup described above only measures velocities in XZ planes of the form $\tilde{\mathbf{c}}(\mathbf{x},t) = \tilde{u}(\mathbf{x},t)\hat{\mathbf{i}} + \tilde{w}(\mathbf{x},t)\hat{\mathbf{k}}$. The missing component, $\tilde{v}(\mathbf{x},t)$, would be best handled by a separate LDV system with an optical axis perpendicular to the first 2D LDV system. It is reasonable to expect, however, that $\tilde{v}(\mathbf{x},t)$ has similar magnitude to $\tilde{u}(\mathbf{x},t)$ due to geometrical symmetry.

A velocity time series, say $\tilde{u}(\mathbf{x},t)$, can be decomposed into a mean value, $U(\mathbf{x})$, and its fluctuations, $u'(\mathbf{x},t)$, about this mean value. This is known as Reynolds

decomposition and is defined in equation (1). The decomposition of an arbitrary set of speed measurements is illustrated in Figure 4 and Figure 5. The mean speed $U(\mathbf{x})$, is simply the arithmetic mean of all the velocity observations at point $\mathbf{x}$ as written in (2). The mean speed of the entire interrogated region, U, is obtained with (3).

$$\tilde{u}(\mathbf{x},t) = U(\mathbf{x}) + u'(\mathbf{x},t) \tag{1}$$

$$U(\mathbf{x}) = \overline{\tilde{u}(\mathbf{x},t)} = \frac{1}{N}\sum^{n=N} \tilde{u}(\mathbf{x},t_n) \tag{2}$$

$$U = \frac{1}{M}\sum^{m=M} U(\mathbf{x}_m) \tag{3}$$

Where

N	is the total number of velocity measurements taken at location $\mathbf{x}$.
M	is the total amount of positions scanned within the region of interest.

The fluctuating part of the local velocity is often reduced to its root mean squared value, as exemplified for $u'(\mathbf{x},t)$ in (4). Global results of turbulence fluctuation rms for all the points measured can be condensed as (5).

$$u'_{rms}(\mathbf{x}) = \sqrt{\overline{u'^2(\mathbf{x},t)}} = \sqrt{\frac{1}{N}\sum^{n=N} u'^2(\mathbf{x},t_n)} \tag{4}$$

$$u'_{rms} = \frac{1}{M}\sum^{m=M} u'_{rms}(\mathbf{x}_m) \tag{5}$$

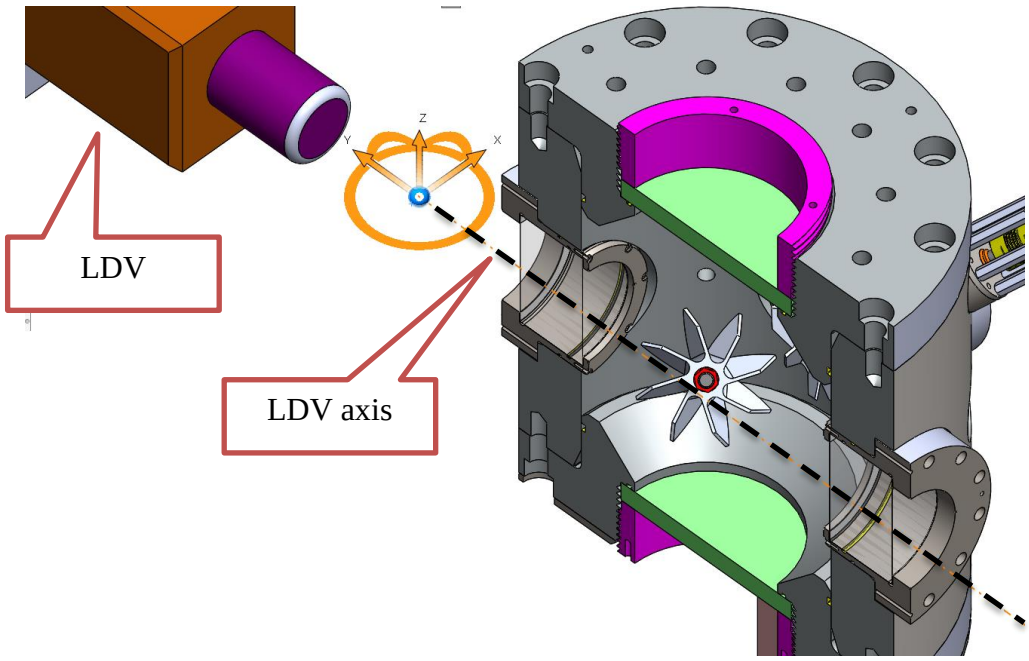

Figure 3 Sketch of LDV transceiver and bomb. The LDV Z axis points along the cylindrical axis of the vessel. The origin of the coordinate system is the bomb center.

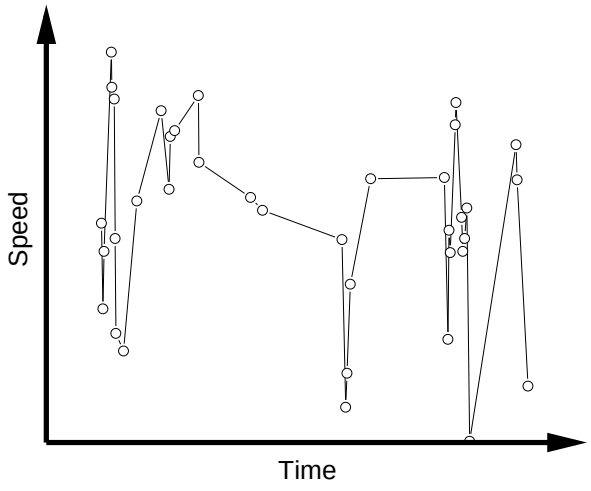

Figure 4 Arbitrary speed time series.

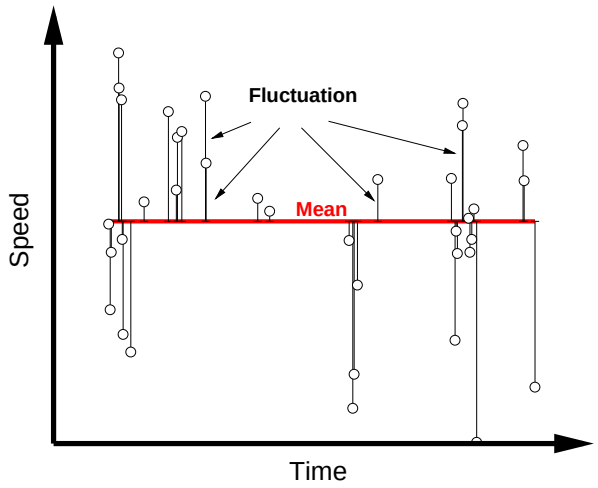

Figure 5 Graphical representation of the Reynolds decomposition of an arbitrary speed time series into a mean value and its fluctuations.

Local planar mean velocity $|C(\mathbf{x})|$ and global planar mean velocity C can be computed with expressions (6) and (7) respectively. A global planar turbulence fluctuation rms c'_{rms} can be computed once u'_{rms} and w'_{rms} are known with (8).

$$|C(\mathbf{x})| = \sqrt{\frac{U^2(\mathbf{x}) + W^2(\mathbf{x})}{2}} \tag{6}$$

$$C = \sqrt{\frac{U^2 + W^2}{2}} \tag{7}$$

$$c'_{rms} = \sqrt{\frac{u'^2_{rms} + w'^2_{rms}}{2}} \tag{8}$$

Effect of impeller diameter in turbulence

A study showed that the first attempt of fan-stirred bomb at Texas A&M University produced modest turbulence fluctuation rms compared to analogous devices elsewhere [23, 29]. Figure 6 collects the response of the turbulent field to the fan rotational speed. A steeper line implies that higher turbulence fluctuation is produced for a given fan speed. The first generation of fan-stirred bomb at Texas A&M University was able to spin relatively fast, but other research groups attained higher levels of turbulence rms even at lower shaft speeds. This fact motivated the search for improved stirrers. The impeller designed for the first generation of fan-stirred flame bomb is shown in Figure 7 while its mounting configuration can be seen in Figure 8.

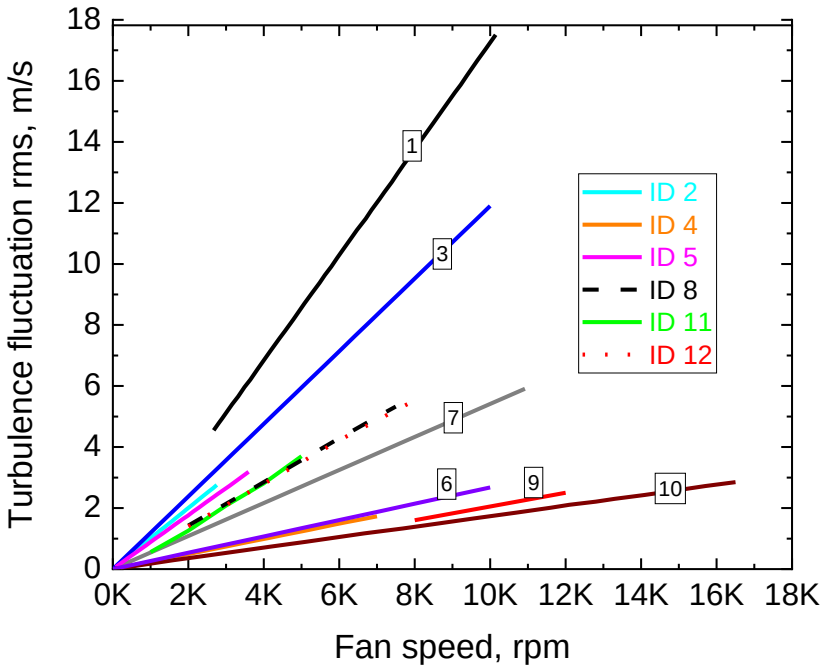

Figure 6 Turbulence fluctuation rms and fan rotational speed of several fan-stirred bombs. ID tags as specified in Table 1.

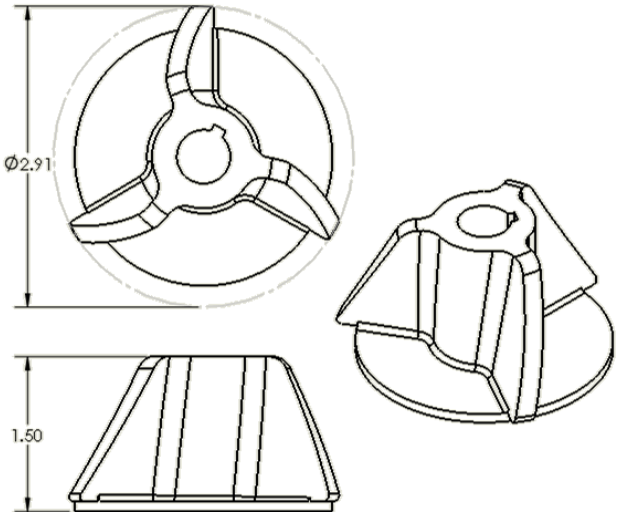

Figure 7 Backward-curved, three-bladed impeller for the first generation of fan-stirred flame bomb at Texas A&M University. The pitch is 20°. Dimensions are in inches.

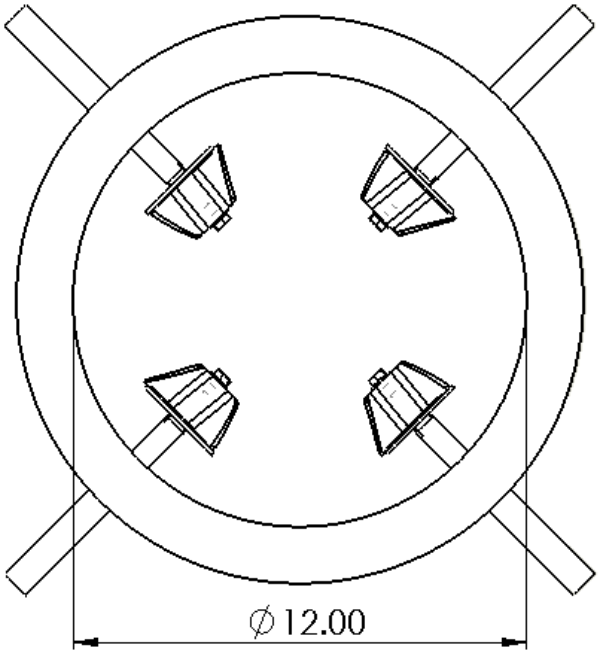

Figure 8 Sketch of the interior of the first generation flame bomb with impellers. The internal length of the bomb cylindrical body, perpendicular to the page, is 14 in. Drawn to scale.

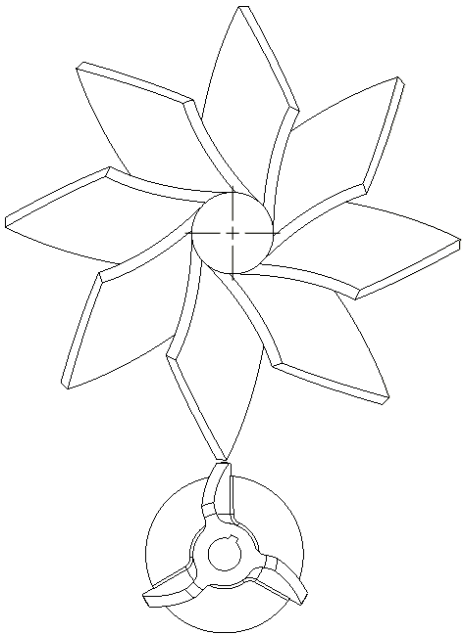

Figure 9 Impeller of University of Leeds versus the three-bladed impeller at Texas A&M University [30].

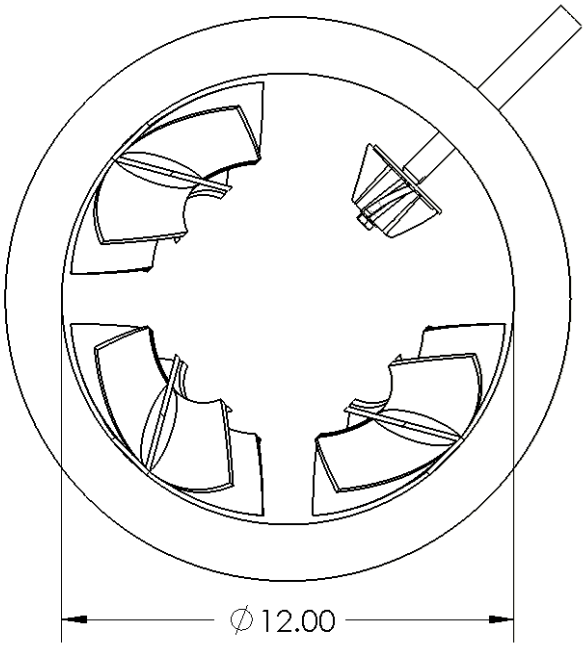

Figure 10 Juxtaposition of impellers in a 12 in diameter bomb. Drawn to scale.

A review of the impellers used in other flame bombs revealed that three-bladed impeller was considerably smaller. The best performer in Figure 6 is the cylindrical bomb built by the University of Leeds [30]. This top performer is compared in Figure 9 side by side with the three-bladed impeller used in the first generation of Texas A&M fan-stirred bomb. Their respective bombs have very similar internal dimensions, but the impeller themselves are contrasting. The comparison is made graphically in Figure 10.

A second impeller was created for the first generation bomb to test the effect of impeller size on turbulence generation. A simple 8-bladed radial design was chosen, Figure 11. This kind of impeller has been used by other groups [12, 19]. The radial impeller diameter was increased 37%, but axial length was kept identical to the three-bladed impeller. The total blade surface area almost folded in five.

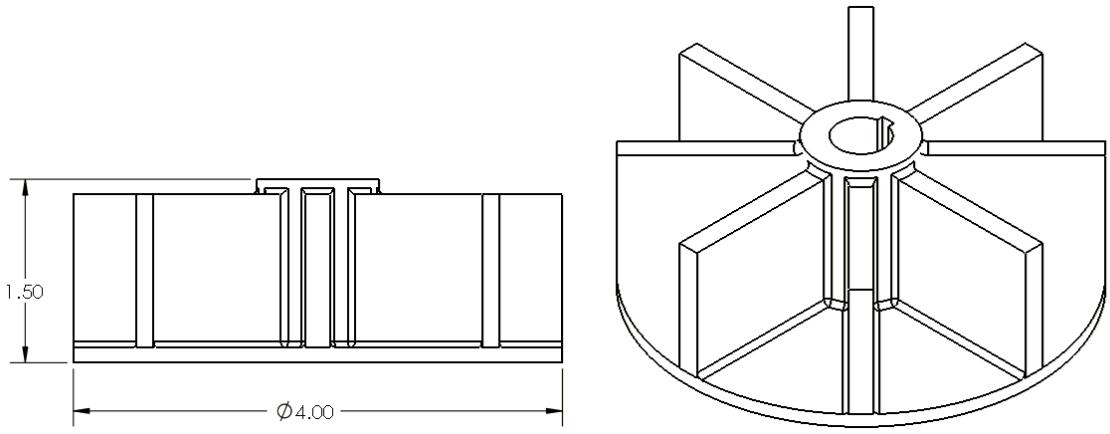

Figure 11 Radial impeller tested in first geneneration flame bomb at TAMU

The flow field driven by the three bladed impeller and radial impeller were qualitatively similar. The radial impeller had significantly higher mean speed in both

measured components. The overall planar mean speed C increased from 0.2 m/s for the original three bladed impeller to 1.2 m/s for radial impellers when both were driven at 8000 rpm. In terms of turbulence fluctuation, radial impeller was also a more vigorous stirrer. The overall average planar of turbulence fluctuation rms c'_{rms}, was increased four folds as it leaped from 1.5 m/s to 6.5 m/s with the alternative set of impellers.

The linear dependence of the turbulence fluctuation rms to the fan rotational speed has been confirmed by the fan-stirred flame bomb literature multiple times in some variant of expression (9) over the years [8, 10, 14, 19].

$$c'_{rms} \sim \omega \tag{9}$$

Where

c'_{rms}	m/s	volumetric average of turbulence fluctuation, a scalar.
ω	rad/s	fan angular velocity.

Equation (10) is the simplest expression that captures the dependence of c'_{rms} on ω. For dimensions to agree, the scaling factor introduced in (10) must have length units. For convenience, we'll name this scaling factor the "effective radius" or r_{eff}. A slope fit to a c'_{rms} Vs. ω curve similar to Figure 6 yields the magnitude of this newly minted effective radius. The effective radii and other figures for the surveyed bombs are listed in Table 2. For the cases presented here, effective radius was found to be a fraction of physical fan radius, approximately 17%.

$$c'_{rms} \approx r_{eff}\,\omega \tag{10}$$

Table 2 Turbulence generation details on several fan-stirred flame bombs.

ID	Institution	Maximum c'_{rms} m/s	Int. Length Scale mm	Impeller diameter mm	Number of fans	Effective radius mm
1	U Leeds cyl. [6]	16	38-42	187.5*	4	16.54†
2	GM/UMI [7-9]	2.2	25-40	135	4	7.26 (9.55‡)
3	U Leeds sph. [10]	11.9	20	150§	4	11.36
4	UMI [11]	1.8	6.9	48	4	2.37
5	Kyushu U [12, 13]	3.2	10.3	200	2	8.84
6	KIT [14, 15]	3.5	3.9	45	8	2.56
7	Taiwan NCU [16-19]	8.3	15-45	116‖	2	5.17
8	Princeton [20, 21]	5.3	4	69	4	6.79
9	TAMU 1st gen.[22, 23]	1.5	20-27	73.9 (101.6#)	4	2.15 (7.76#)
10	U d'Orléans [24]	2.8	3.4	40	6	1.64
11	CNRS-ICARE [25]	3.7	16	130	8	7.48
12	This work	5.5	16	124.5	4	6.60 (10.07Δ)

* The references on this bomb report 147 mm mean diameter. To be consistent with the comparison of other bombs, the outer diameter has been estimated to 187.5 mm. See sketch at appendix.

† Measured with LDV. Previous publications on the apparatus using hot wire anemometry reported significantly lower c' [6, 31]. The effective radius of hot wire measurements is 7.2-7.5 mm.

‡ r_{eff} = 7.26 mm for fans blowing toward the center of the vessel, and r_{eff} = 9.55 mm for reverse operation.

§ Actual diameter is not found in the reference. Outer diameter guessed is offered here based on pictures and dimensions of other features.

‖ This group has several cruciform bombs. To the author knowledge, no detailed characterization has been released for the spherically expanding flame bomb [16, 18], despite the fact that dimensions are not identical to previous downward propagating flame version. Wording in [17] imply that the impeller remained unchanged from [19].

\# Values in parenthesis correspond to the radial impeller, Figure 11.

Δ Values in parenthesis correspond to the plug impeller.

The effective radius artifact makes the comparison among fan-stirred bombs straightforward and seems to make reasonable predictions despite the disparate nature of the fans, bomb shape and dimensions surveyed, as supported by Figure 12. Larger impellers seem associated with more intense turbulence fluctuation rms but at least one apparatus, ID 5 in Table 2, did not conform to the trend showed by the rest of the population. Bomb ID 5 has the largest fan impeller in the table, but only has two fans installed, while most bombs have at least 4 agitators.

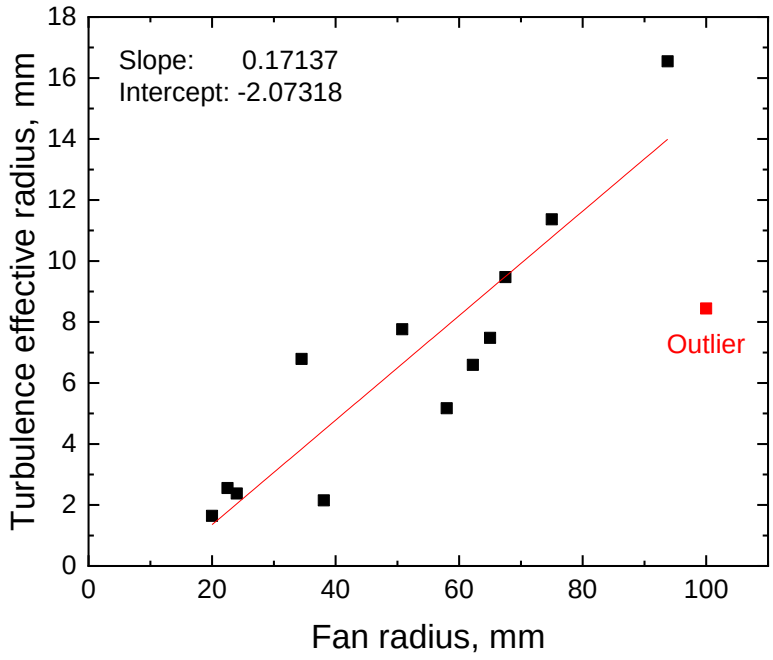

Figure 12 Turbulence effective radius as a function of fan radius. Outliers have been excluded from linear regression.

Figure 13 was made considering the total amount of fans installed in each rig by making the horizontal axis the product of fan count and fan radius. This product is also

correlated to better stirring. Interestingly, the outlier in Figure 12 and Figure 13 is not the same device. The outlier point in Figure 13 is ID 11 in Table 2, the largest bomb by volume. Bomb ID 11 has 8 fans, ⌀ 130 mm each, to agitate 93.4 liters of internal volume. The next largest vessel is 2.7 times less voluminous.

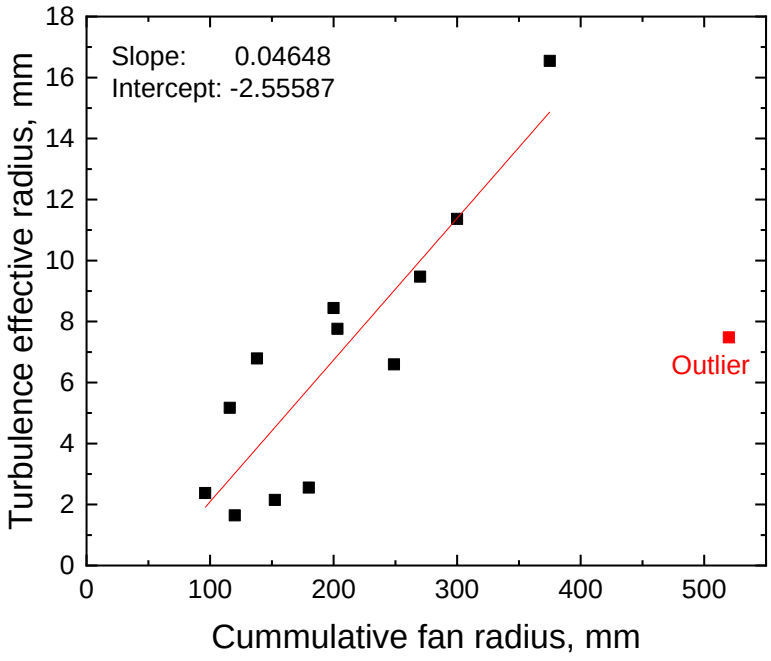

Figure 13 Turbulence effective radius vs the product of fan radius and the total number of fans installed.

Effect of impeller design

The study of other bombs in literature and their stirring fans showed that the impeller should be larger than previously attempted in the first generation of fan-stirred flame bombs at Texas A&M University. There are of course limitations on how large the impeller can be. The impeller should preferably be small enough to fit through the vessel window bore to facilitate assembly, i.e. $\varnothing \leq 6.747$ in. Five impeller designs of similar diameter were evaluated. Four designs were custom made for this study, and their geometries and dimensions are shown in Figure 14.The fifth stirrer was a commercial leaf blower / vacuum impeller, Toro 127-7092. The blower impeller is made of magnesium and has backward curved blades. Its diameter is 4.9 inches and the axial length is 1.96 inches. Only one axial design was tested and the rest were centrifugal fans. It was decided that the maximum velocity would be reduced from 24,000 rpm to 10,000 rpm. A low shaft surface speed permits the second generation fan-stirred bomb to use of lip seals, which are relatively inexpensive and require no ancillary hardware to run. The test conditions were limited by the available power.

Power consumption results are plotted in Figure 15. The radial design, or paddle wheel was the most onerous to run. The axial and backward curved impellers also imposed a load greater than the motor continuous service capacity at 6000 rpm, but they were still manageable momentarily. The plug and blower impellers were chosen for a LDV characterization from 0-6000 rpm.

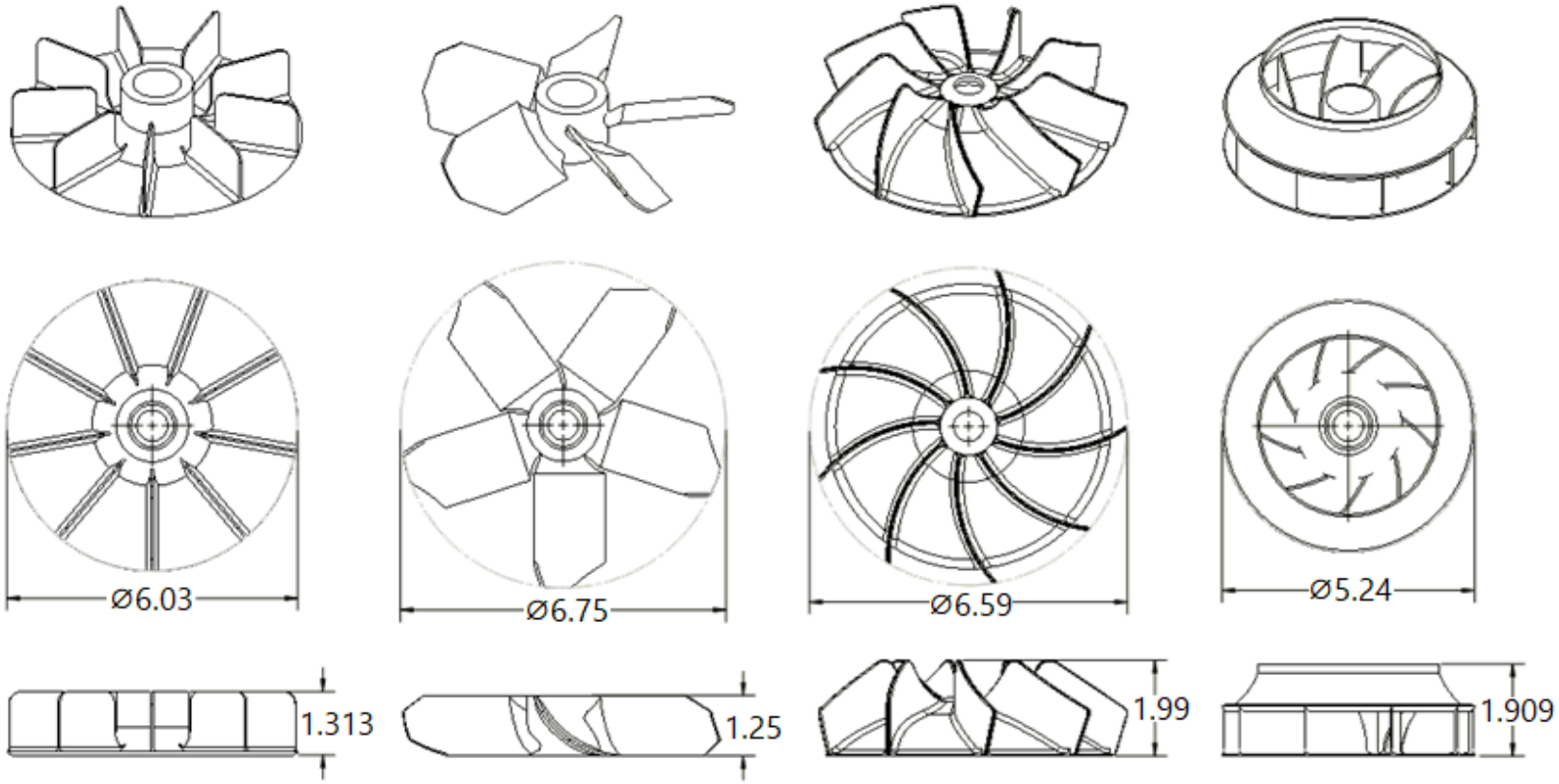

Figure 14 Custom impeller prototypes tested. From left to right radial, axial, backward curved, plug design.

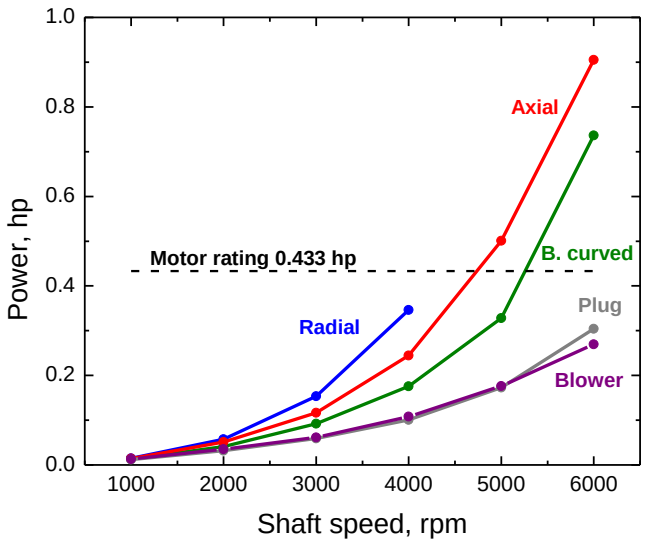

Figure 15 Power consumption of DC motor when driving different impeller candidates. The lip seals were not installed during measurements.

LDV characterization

The flow field of the leaf blower impeller and the custom plug impeller was characterized with LDV measurements inside a central cubic region of 88×88×88 mm with a grid spaced at 22 mm. The plug fan flow field main features are summarized in Table 3. The linear dependence of turbulence fluctuation is evident in u' and w', and in consequence, c'. The same cannot be said about the mean components U and W. The horizontal mean speed U increases geometrically with angular velocity, while the magnitude of W does not even behave monotonically. There is a marked anisotropy in the turbulence fluctuation as u' is only ¾ of w'. The disparity between u' and w' is confirmed by a nonzero shear stress $\overline{u'w'}$. The flow field is however fairly homogenous. In general, the distribution of the turbulence fluctuation around the mean speed resembles a normal

distribution. There is almost no skewness and the flatness is close to 3.0 expected for a normal distribution. The mean velocity becomes larger proportion of the turbulence rms as fan speed increase, shows the inverse turbulence intensity C/c'.

The LDV collected velocity measurements at each location for at least 5 seconds after the flow became statistically stationary. This acquisition period is many times longer than the integral time scale. The measurements can be assembled to form a 2D quiver plot such as Figure 16. The collection of these quiver plots shows the flow towards the suction of the impellers. This is not surprising; in average, the flow will always converge towards the suction and move away the trailing edge of the impeller, if sufficiently long averages are taken. The same pattern was recognized with both impellers (i.e. plug and leaf blower) at all tested motor speeds. The rest of the quiver plots was left as appendix material.

Table 3 Flow field characterization of plug fan. Effective radius r_{eff} = 10.07 mm.

	2k rpm	**4k rpm**	**6k rpm**
U	-0.1784	-0.5354	-1.5134
W	-0.1167	-0.4385	-0.2293
u'	1.6925	3.4937	5.2299
w'	2.2428	4.6451	7.0302
$\overline{u'w'}$	-0.1377	-0.6079	-0.8072
$u'_{skewness}$	-0.0093	0.0153	-0.0072
$w'_{skewness}$	0.0326	0.0206	0.0045
$u'_{flatness}$	3.3017	3.3868	3.2872
$w'_{flatness}$	2.9008	3.0155	2.8892
C	0.1508	0.4893	1.0823
c'	1.9907	4.1157	6.2090
Inverse intensity C/c'	0.0757	0.1189	0.1743
Isotropy u'/w'	0.7600	0.7553	0.7491
Homogeneity std. dev.	0.0827	0.0856	0.0842

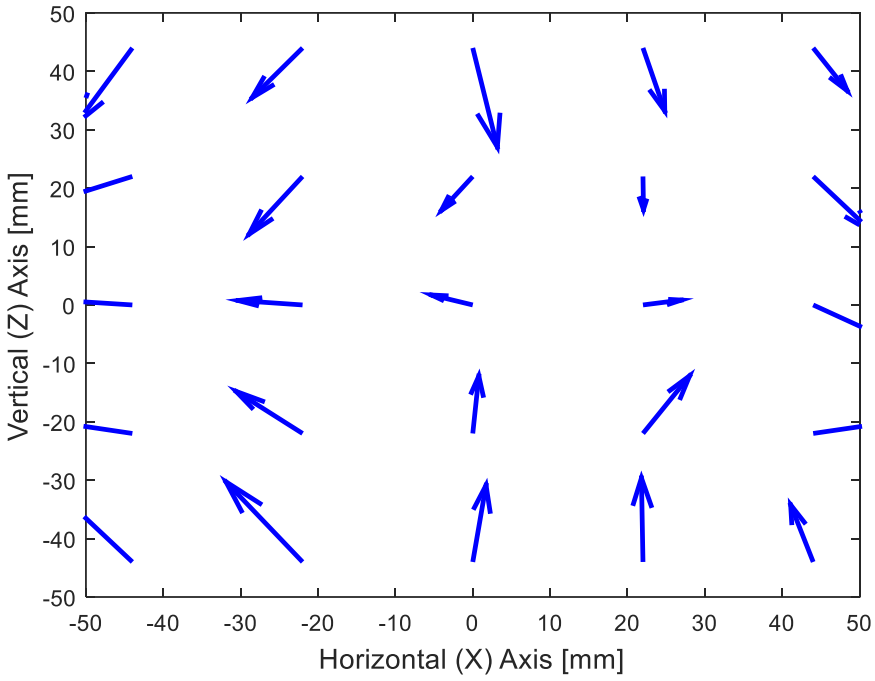

Figure 16 Quiver plot of the mean flow produced by plug fans spinning at 6000 rpm at the central plane. The length of the arrows indicate the relative magnitude.

The plug fan and the other custom prototypes were 3D printed in polylactic acid (PLA), see Figure 17. Excessive vibration was observed at 8000 rpm and for this reason it was not deemed safe to make a characterization at that speed. The leaf blower impeller was installed in two positions along the shaft. The first was at the shaft tip, away from the bomb walls and the second position was close to the wall, leaving only a small clearance between the wall and the impeller blades, as shown in Figure 18

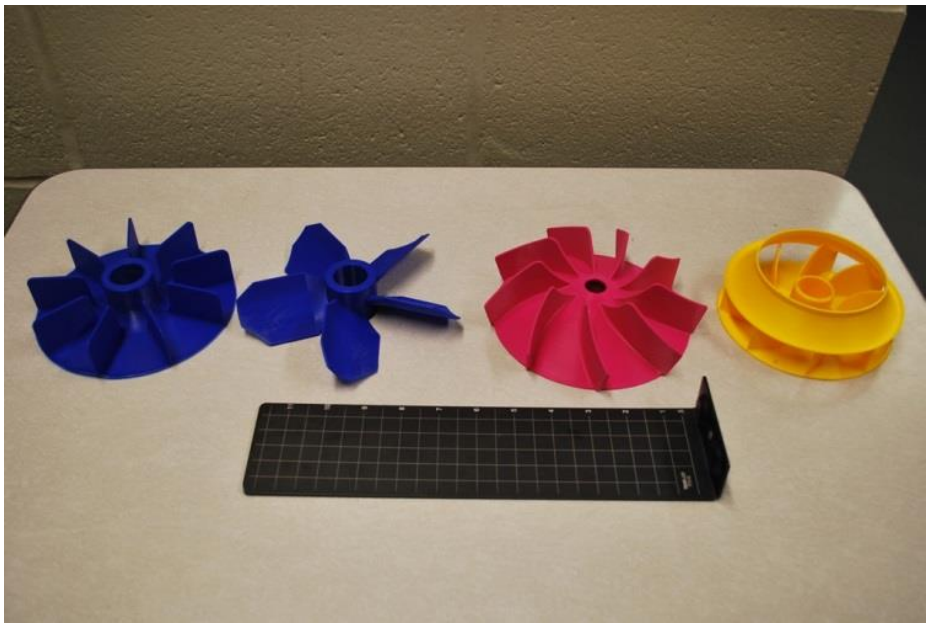

Figure 17 3D printed impeller prototypes.

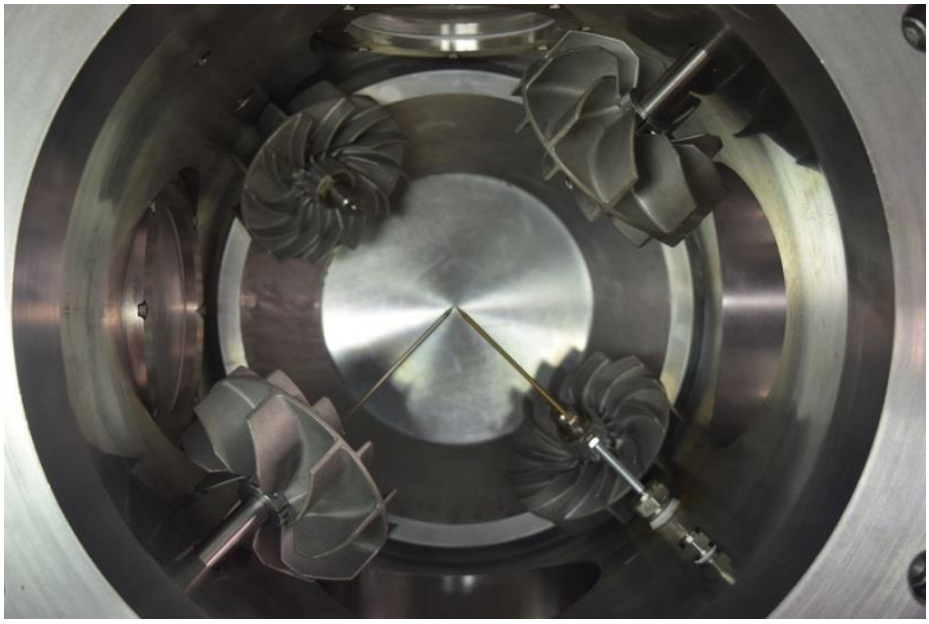

Figure 18 Leaf blower impellers installed in bomb, top view. The top end cap was removed to take this image.

Next on the LDV characterization results is the leaf blower fan, Table 4. A substantially higher mean velocity in the horizontal direction was observed U compared with the plug design. This in turn makes the inverse turbulence intensity C/c' about 21.5% in average. The leaf blower, when installed at the shaft tip, closest to the bomb center of the vessel, generates slightly less anisotropic turbulence fluctuation. Interestingly, u' is larger than w', in contrast with the plug fan case. The characteristic turbulence c' is produced by the leaf blower is markedly lower than that of the plug fan. As a matter of fact, the effective turbulence effective radius is only 6.6 mm compared to 10.07 mm, despite the fact that both impellers pull nearly the same power from the electric grid to run. The standard deviation of the flow field turbulence homogeneity is 10 %.

Table 4 Flow field characterization of blower fan. Effective radius reff = 6.6 mm.

	2k rpm	**4k rpm**	**6k rpm**	**8k rpm**	**8k (wall) rpm**
U	-0.3729	-0.7957	-1.5719	-1.6218	-2.5139
W	-0.0226	-0.0665	-0.0325	0.0572	0.0316
u'	1.5558	3.0794	4.6967	6.0741	5.4113
w'	1.2275	2.4694	3.676	4.9193	5.3317
$\overline{u'w'}$	-0.0075	-0.1081	-0.2822	-0.2149	-0.0908
$u'_{skewness}$	0.0247	0.0777	-0.0029	0.0407	0.0046
$w'_{skewness}$	0.0003	0.0035	-0.0007	0.0054	-0.0025
$u'_{flatness}$	3.0476	3.1399	3.2198	3.1441	3.1312
$w'_{flatness}$	3.1327	3.1078	3.1793	3.0707	3.0235
C	0.2642	0.5646	1.1117	1.1475	1.7777
c'	1.4026	2.7936	4.221	5.5316	5.3769
Inverse intensity C/c'	0.1883	0.2021	0.2634	0.2074	0.3306
Isotropy u'/w'	1.2719	1.2485	1.2786	1.2366	1.0157
Homogeneity std. dev.	0.0957	0.0974	0.1087	0.0971	0.1002

Fan-stirred flame bombs aspire to produce a region of isotropic homogenous turbulence with negligible mean flow. The unbalance between the horizontal and vertical components of the turbulence fluctuation is therefore unfavorable. Fortunately, this kind of cylindrical bomb with tetrahedral fan configuration can adjust the relative importance of the horizontal and vertical rms values by sliding the impeller along the shaft closer or away from bomb center, Figure 19. As the blades come closer to the bomb wall, the later acts as shroud or housing that favors the flow along the cylindrical axis. The first 4 columns in Table 4 were done with the impeller installed at the tip of the shaft. The impellers were then slid towards the wall the measurements at 8000 rpm were repeated. The flow became isotropic while still homogenous. The overall inverse intensity was negatively affected, since it increase from ~21% to 33%.

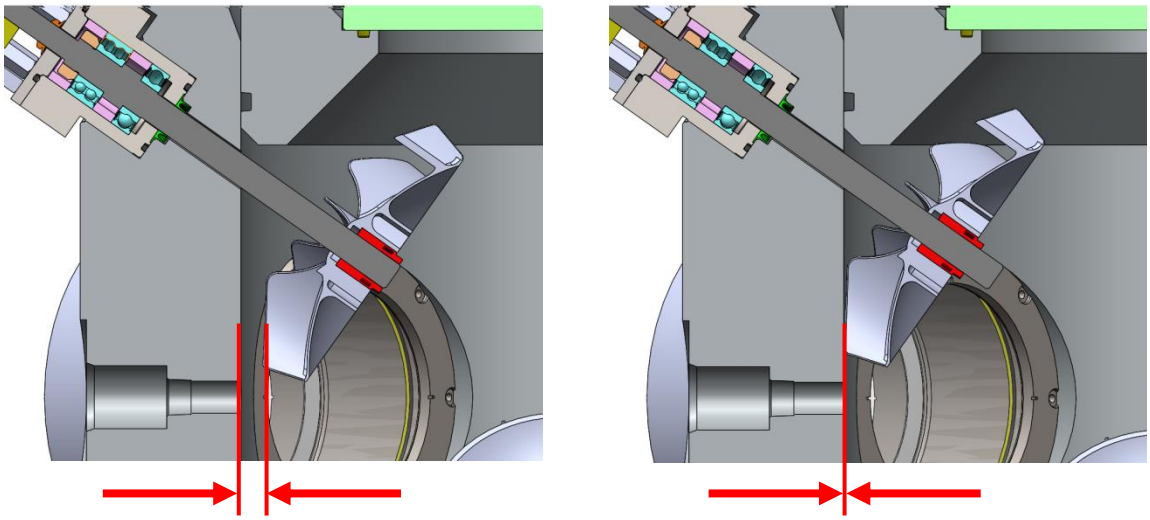

Figure 19 Comparison of impeller installation position. On the left, the impeller is installed at the tip of the shaft, closest to the bomb center. On the right, the impeller has only a small clearance with the bomb cylindrical wall.

The temporal coherence of the flow field was studied by computing autocorrelations, Table 5. A computer program was written in Fortran and the source code has been included in the appendices. It was found that at the center of the bomb, coordinates [0, 0, 0], the integral time scale of both, $u'(\mathbf{x},t)$ and $w'(\mathbf{x},t)$, decreased monotonically with fan shaft speed regardless of the fan design. However, such dependency was not observed at the point [-44, 44, -44], especially in the case of the blower fan installed at the tip of the shaft. There, at one of the corners of the cubic region scanned with LDV, the time scales of $w'(\mathbf{x},t)$ were consistently short, while those of $u'(\mathbf{x},t)$ were longer and with more spread.

The LDV is an instrument that needs no calibration and is particularly suitable to the study of the temporal coherence of the flow. However, LDV is usually not the best tool to investigate the length scales unless under special conditions. Figure 20 offers autocorrelation plots for the leaf blower fan installed with close clearance to the wall. The self-correlations have been smoothed with the Savitzky-Golay method using 32 points per window to fit a 2^{nd} order polynomial. The integral time scale is numerically equal to the area below the autocorrelation curve, from null delay to the first zero crossing. The rest of the self-correlation plots are left in the appendices. The parallel Fortran code written to compute integral time scales is also part of the appendices.

Table 5 Integral time scale of selected locations expressed in milliseconds. Coordinates in millimeters.

	$u'(\mathbf{x},t)$ **[0, 0, 0]**	$w'(\mathbf{x},t)$ **[0, 0, 0]**	$u'(\mathbf{x},t)$ **[-44, 44, -44]**	$w'(\mathbf{x},t)$ **[-44, 44, -44]**
Plug, 2000 rpm	14.29	12.60	12.42	21.04
Plug, 6000 rpm	3.85	4.40	5.01	5.46
Blower, 2000 rpm	34.51	11.20	8.39	2.94
Blower, 4000 rpm	14.46	8.68	10.12	4.44
Blower, 6000 rpm	11.46	5.88	13.78	2.40
Blower, 8000 rpm	8.85	3.13	4.70	2.27
Blower, 8000 rpm, at wall	4.64	4.29	6.39	2.75

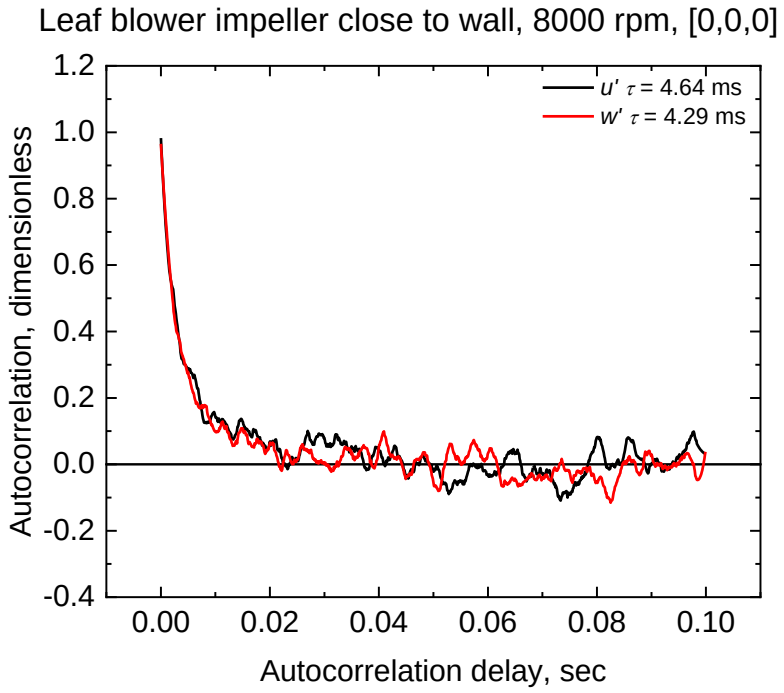

Figure 20 Autocorrelation of turbulence fluctuation at vessel center. The leaf blower fan was installed with a close clearance from the wall.

APPARATUS DESIGN

Optical setup and blast room

A schlieren set up was designed with plano-convex lenses to collimate the light coming from a mercury arc lamp. Flat mirrors on kinematic mounts were used to steer the light from the light source, though the vessel and into de camera. The blast room layout at Texas A&M Turbomachinery Laboratory was modified to accommodate the new rig and optimize the resource share with the existing devices. A view of the blast room is offered in Figure 21.

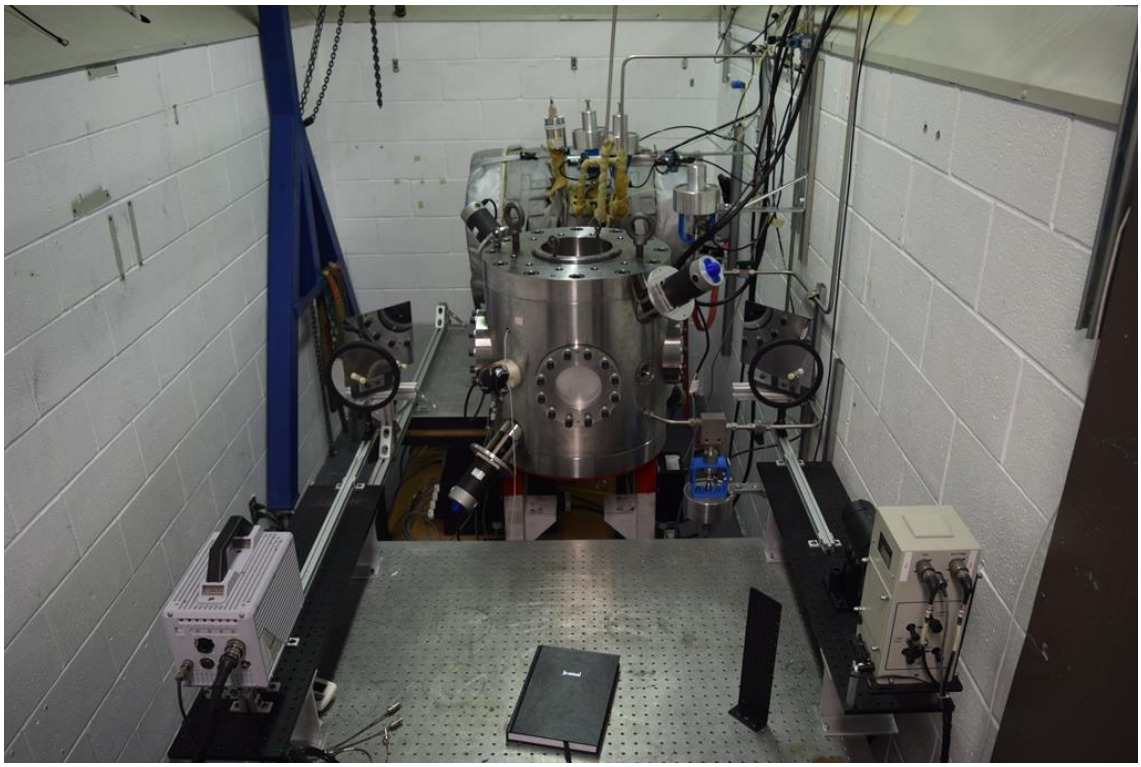

Figure 21 Blast room layout. The new fan-stirred flame bomb of the present work is at center. An existing, heated, stainless steel, laminar flame bomb is partially visible in the back.

Stirring assembly

Stirring the contents of a pressure vessel with fans is not trivial task. A penetration to the vessel must be made to drive the shafts with seals that allow the best possible control of the composition of the gaseous mixture inside the vessel without leaking and also that consistently survive the blast of confined deflagration. In addition, the stirring assembly is expected to run at a maximum speed of 10,000 rpm at temperatures above ambient.

The selection of the motor is constrained to a number of factors such power demand, ease of assembly, maintenance and operation. During design, it was chosen to mount the motor directly on the vessel. The motor had to be strong enough to drive the fan and overcome the seal friction while being light enough to be easily handled by one person and flange-mounted directly on the bomb. It was decided to motorize the shaft with two different motors to cover the range of desired speed. To run in low range, from 0 to 6000 rpm, a DC brushed motor was chosen. The DC motor main characteristics are listed in Table 6 and its physical dimensions detailed in Figure 22. The DC motor is nominally rated 323 W (0.429 hp), although it can handle overloads for short periods of time. The DC motor control, KB Electronics model KBMD-240D, was upgraded with a heatsink to increase the deliver up to 745.7 W (1 hp).

The higher end of the speed range, 8,000 - 10,000 rpm, is powered with a router motor pack. Some relevant figures about the router motor pack are collected in Table 7. The motor pack has a built-in speed controller that allows adjusting the rotational speed from 8,000 to 24,000 rpm, albeit no very precisely. A fixed router base, Dewalt DW6184, permits a convenient coupling with the receiving flange of the stirring assembly.

Table 6 Technical specifications of Ametek Pittman ID33005 DC brushed motor.

Specification		
Supply Voltage	90	Vdc
Continuous Stall Torque	7.50	lb-in
Speed @ Cont. Torque	6000	rpm
Current @ Cont. Torque	8.33	A
Continuous Output Power	323	W
	0.429	hp
Maximum speed	6000	rpm
Peak Current	33.20	A
Peak Torque	37.50	lb-in
Weight	7.20	lbs

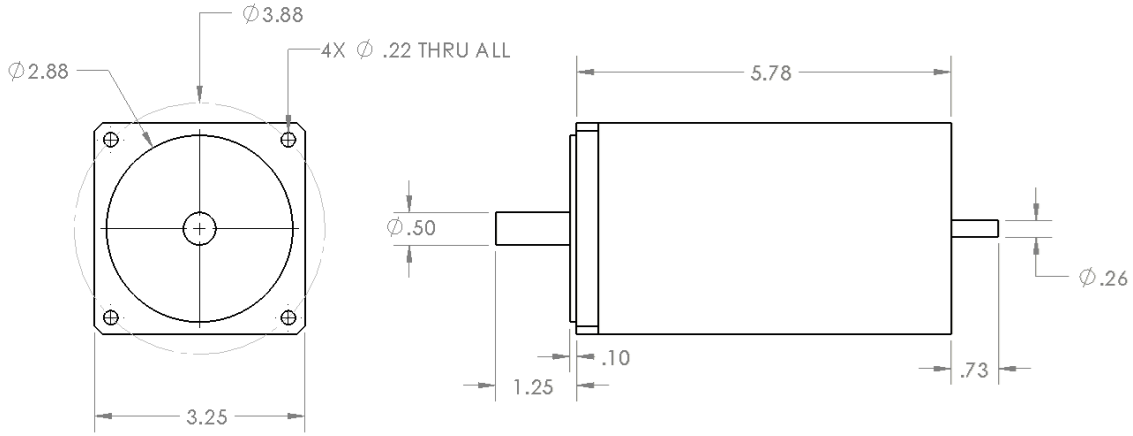

Figure 22 DC brushed motor. Pittman ID33005. Dimensions in inches.

Table 7 Technical specifications of Dewalt DW618 motor.

Specification		
Supply voltage	125	Vac
Power	2.25	hp
No-load speed	8 - 24	krpm
Current	12.00	A
Collet diameter	¼, ½	in
Weight	10.1	lbs

The fan shaft was designed to a maximum speed of 10,000 rpm. An excerpt of the shaft engineering drawing is presented in Figure 23. The critical speed was estimated with the Rayleigh–Ritz method, following expressions (11) through (14). The fan weight was modeled as a lump load applied at the tip of the shaft. The shaft was approximated to a cantilever beam 6.5 in long in this analysis, which corresponds to the distance from the guide bearing to the shaft tip.

$$N_{crit} = \frac{30}{\pi}\sqrt{\frac{1}{\delta_{st}}} \tag{11}$$

$$\delta_{st} = \delta_{shaft} + \delta_{fan} \tag{12}$$

$$\delta_{shaft} = \frac{m_{shaft} L^3}{8EI} \tag{13}$$

$$\delta_{fan} = \frac{m_{fan} L^3}{3EI} \tag{14}$$

Where:

N_{crit}	11,798	rpm	shaft critical speed
δ_{st}	6.48	μm	total shaft static displacement
δ_{shaft}	2.33	μm	shaft displacement under its own weight
δ_{fan}	4.15	μm	shaft displacement due to the weight of the impeller
m_{shaft}	0.258	kg	mass of shaft (cantilever end)
m_{fan}	0.173	kg	mass of impeller (early prototype)
L	16.51	cm	cantilever length of shaft (6.5 in)
E	196	GPa	modulus of elasticity
I	3.12E-9	m^4	area moment of inertia

The numbers have been scaled for reading convenience. Proper unit concordance must be enforced in computation.

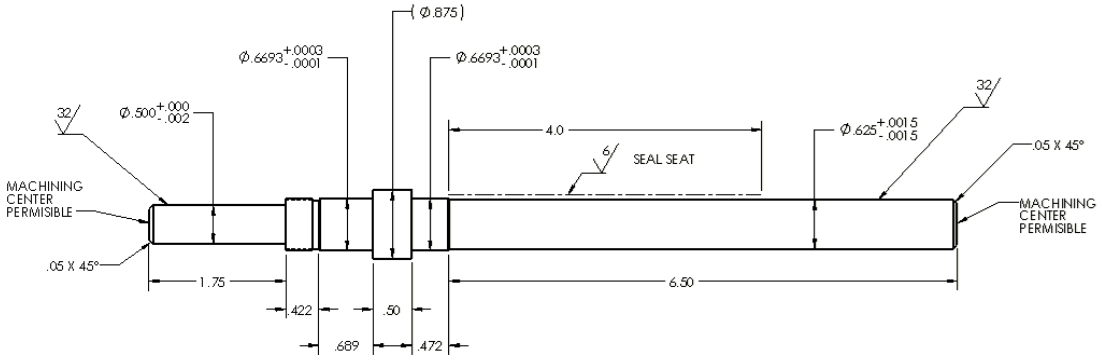

Figure 23 Fan shaft drawing detail.

A hammer impact test was performed to a stirring assembly, and the natural frequency acquired was 176 Hz with the Toro leaf blower impeller installed at the tip of the shaft. This corresponds to a critical speed of 10,560 rpm which confirms that the approximations taken for the Rayleigh–Ritz calculation were reasonable. A different configuration, with the leaf blower installed with a close clearance the bomb interior wall, produced a natural frequency of 448 Hz. The alternative fan location critical speed, 26,880 rpm, is much higher and well away from the operation range of the stirring assembly.

The rotary assembly was built with inherently balanced elements, however the assembly as a whole was not dynamically balanced. The shaft was machined without keyways. Keyless torque couplings, adapters, and locknuts were chosen. With these elements it was possible to adjust the location of the impeller along the shaft. This flexibility was needed to accommodate different impeller geometries in the stirring assembly. The motors were chosen to have the same shaft diameter, so that a single coupling could be used for both.

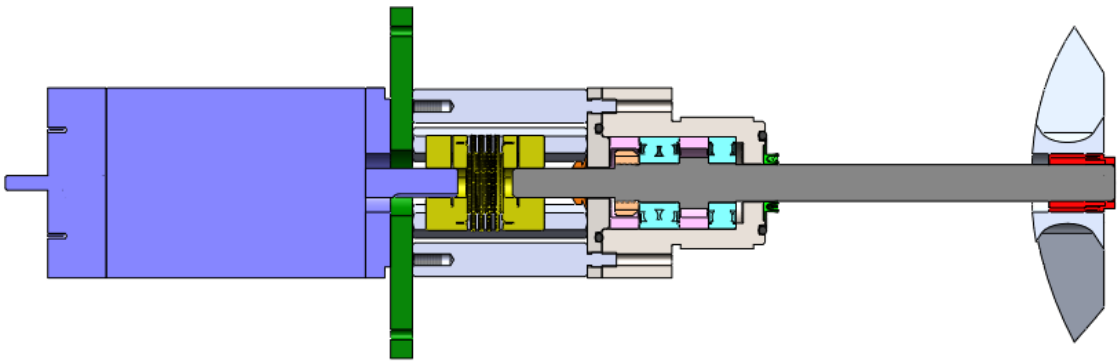

Figure 24 Stirring assembly cross section.

The bellows coupling can be slid to facilitate assembly, colored yellow in the assembly cross section Figure 24. With the proper machining tolerances, keyless shaft-hub connector provides a very secure interference fitting with the impeller at any position along the shaft. The keyless connector has been colored bright red in the assembly view, Figure 24.

The primary seal around the shaft and the bomb penetration is a spring-loaded PTFE lip seal, shown in bright green in Figure 25. The lip seal has a flanged profile that is clamped between the bomb body and the bearing housing to ensure that the seal does not spin with the shaft. The lip seal material is chemically inert at elevated temperatures and pressures and is capable of running without lubrication at high surface speeds. It is rated for 3000 psi at maximum rotary surface speed of 1500 ft/min. The shaft was ground to surface finish of R_a 6 μin as recommended by the seal manufacturer. Secondary containment seals have been placed in tandem. A pair of o-rings closes the static path, while a v-ring, orange in Figure 25, keeps contaminants out of the bearing cavity and weakly assists vacuum seal.

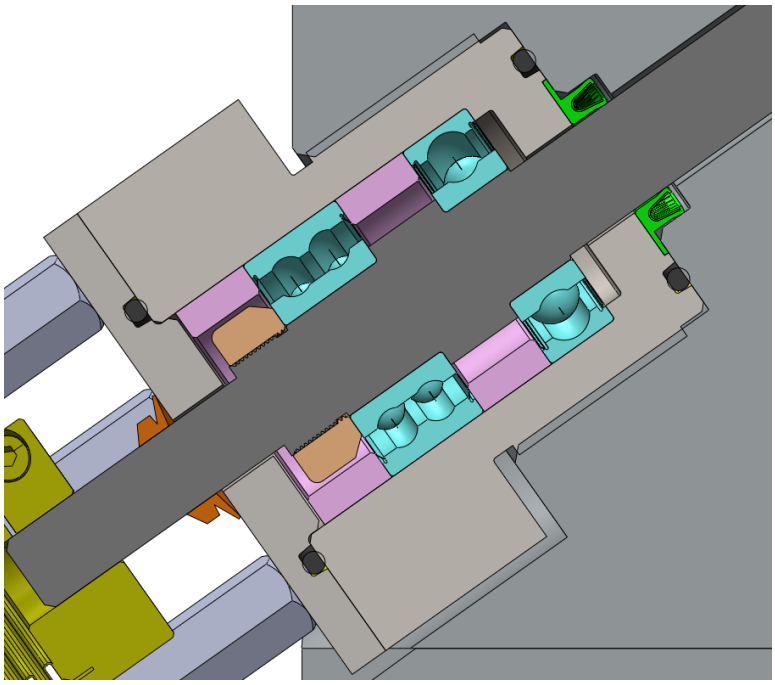

Figure 25 Bomb and stirring assembly detail cross section.

A cage is created with 6 standoff bolts that serve multiple purposes as they secure the bearing housing lid, enclose the shaft coupling and provide a mounting structure for the motor receiving flange. The concentric design makes robust assembly because the maximum possible misalignment of the shafts is limited by the clearance and machining tolerances. Nevertheless, the metal bellows coupling absorbs and accommodates any leftover misalignment.

Windows

Two sets of orthogonal windows is a key feature of this apparatus. Orthogonal lines-of-sight enable optical techniques that potentially resolve the 3D structure of the flame in tomography or even stereoscopy, as opposed to the 2D projection of schlieren imaging. For example, the instantaneous flow field at a given cross section can be rendered

using PIV or the concentration of a specific species can be mapped across the flame at any time applying planar laser induced fluorescence. Two windows are visible in Figure 26.

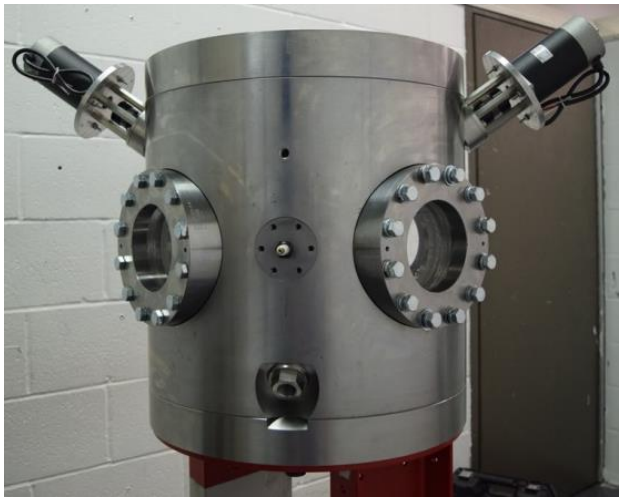

Figure 26 Turbulent flame bomb during assembly. Plumbing and wiring work is missing in this picture.

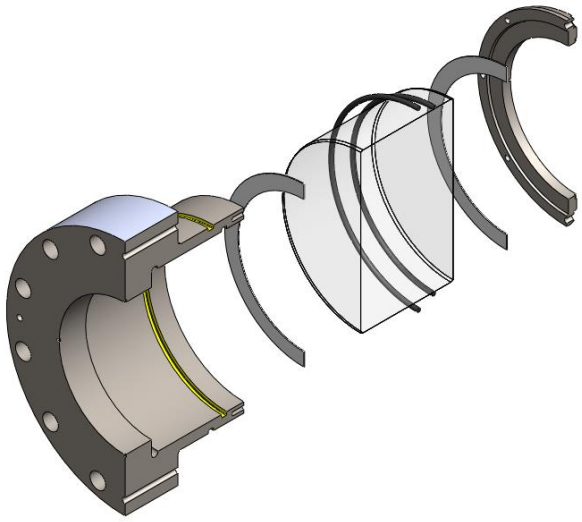

Figure 27 Exploded cutaway view of the window subassembly.

The window substrate is padded with 1/32-inch thick PTFE gaskets and is gently clamped inside the cell. The clamp does not need very strong because it function is to retain the substrate in place in vacuum. A couple of circumferential o-rings shut the gas path. The o-rings glands are highlighted in yellow in Figure 27. This arrangement makes the viewport airtight and keeps the window in a low-stress state.

The quartz window substrate was designed for a pressure of 3000 psi using the following expression [32]:

$$t_w = 0.5 \overline{\varnothing}_a \sqrt{k_w f_s \frac{\Delta P}{\sigma_y}} \tag{15}$$

Where,

t_w	3.50	in	window thickness
$\varnothing_a$	5.00	in	aperture diameter
k_w	0.75	dim	support condition (clamped = 0.75, unclamped = 1.25)
f_s	7.58	dim	safety factor
ΔP	3000	psi	pressure differential
σ_y	8700	psi	fracture strength

A 7.6 safety factor was chosen exacting a minimum thickness of 3.5 in. according to equation (15) Simulations show an overall low level stress with a maximum tension stress of 2.3 ksi on the center of the exterior face when an internal pressure of 3000 psi is applied; see Figure 28 and Figure 29.

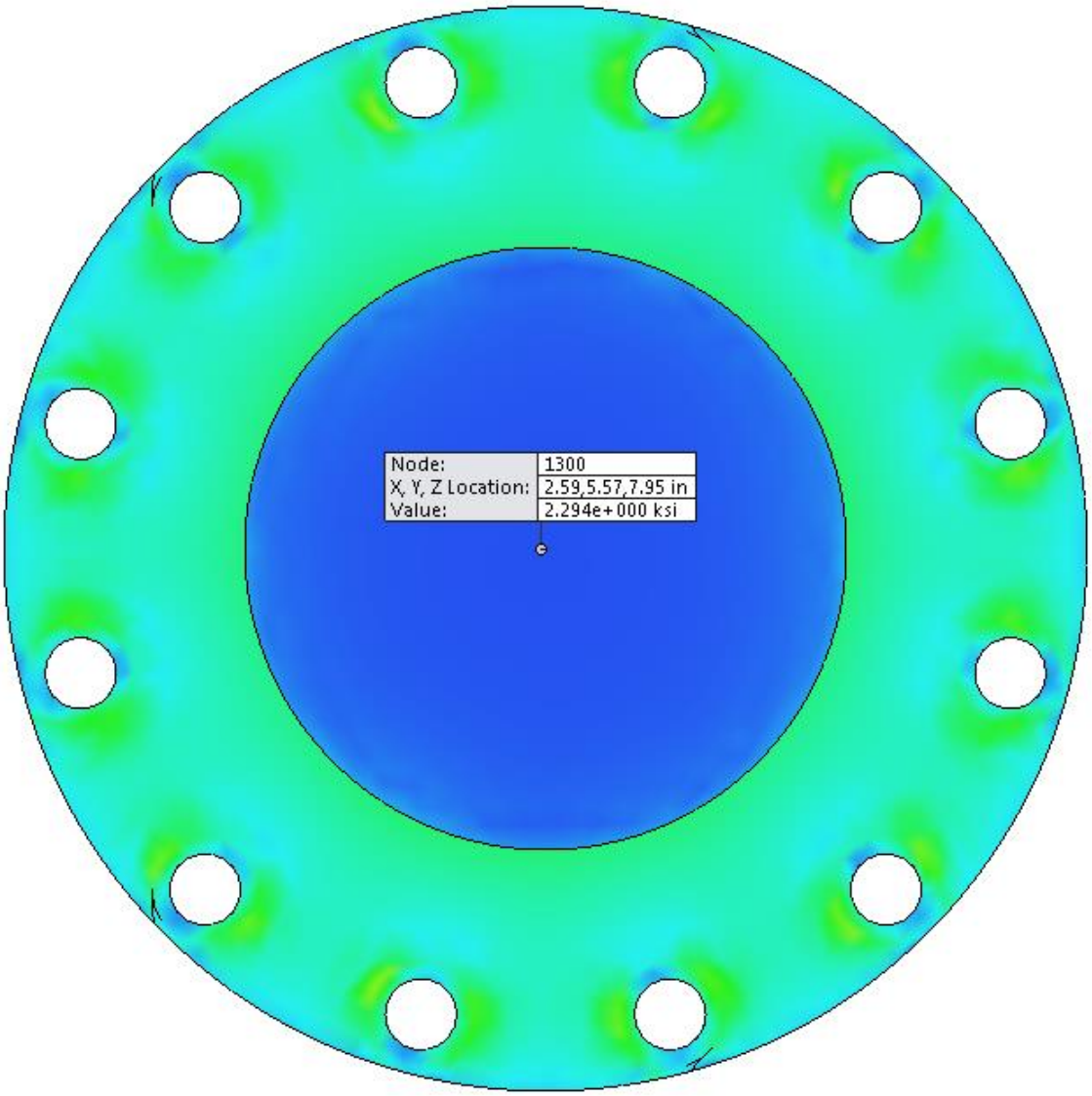

Figure 28 Contour plot of von Mises stress of window assembly, front view.

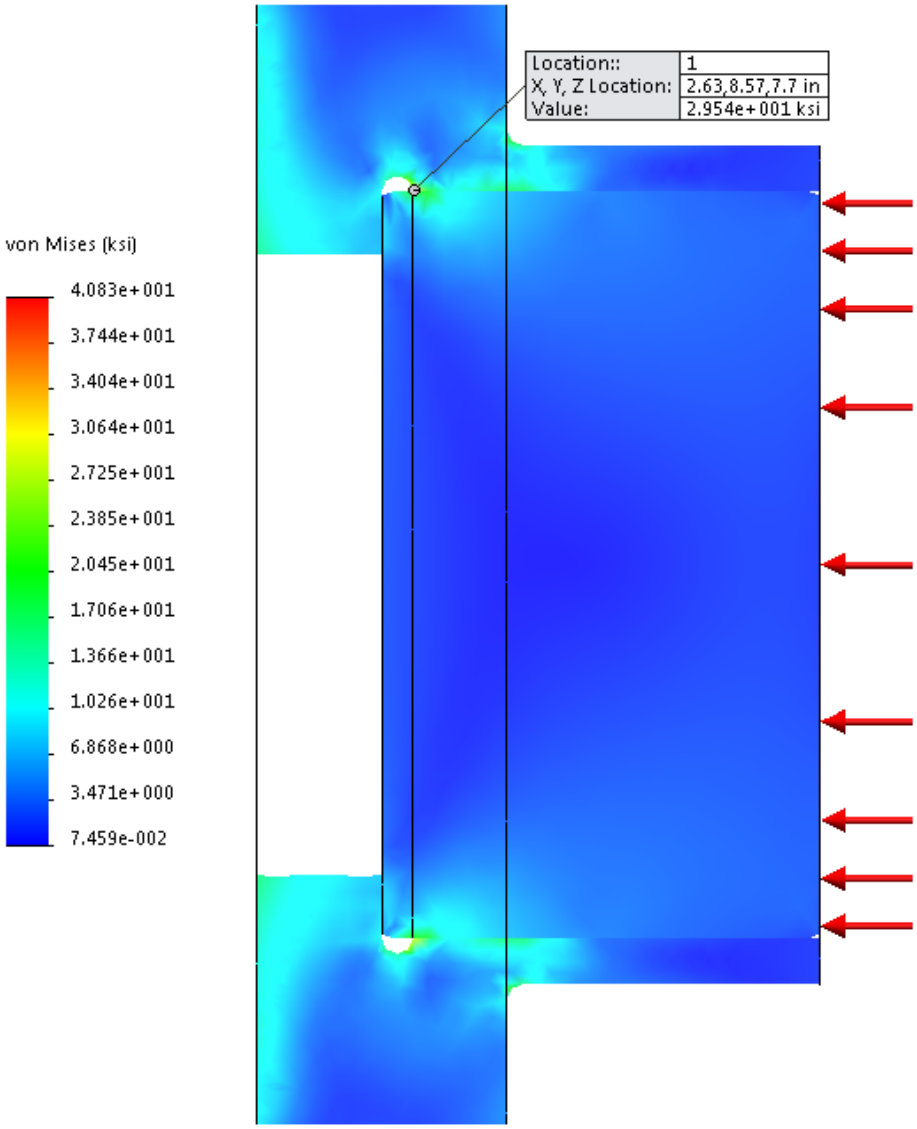

Figure 29 Von Mises stress of window assembly, cutaway view.

Pressure vessel

The vessel is intended to perform spherical flame experiments at 10 atm prior to ignition. An instantaneous peak pressure of roughly 10 times the initial pressure is

expected typically in closed volume combustion. Therefore, the design maximum pressure was chosen to be 100 atm (1,469.6 psi).

The material chosen for this apparatus has the ASTM specification A182 F 6A. It is a forged martensitic stainless steel. The steel was hardened to reach a Class 4 designation with the heat treatment specified in Table 8. The mechanical properties of A182 F 6A in its Class 4 hardened condition are summarized in Table 9. The material was shaped into seamless rings. The construction of the pressure vessel out of forged cylinders eliminates welding procedures.

Table 8 Heat treatment requirements for ASTM grade F 6A class 4 [33].

Heat Treatment Type	Minimum Austenitizing Solutioning Temperature, °F [°C]	Cooling Media	Quenching Cool Below °F [°C]	Minimum Tempering Temperature °F [°C]
Anneal	Not specified	Furnace cool	N/A	N/A
Normalize and temper	Not specified	Air cool	400 [205]	1000 [540]

Table 9 Tensile and hardness requirements for ASTM A182 F 6A class 4 [33].

Tensile Strength, min, ksi [MPa]	Yield Strength†, min, ksi [MPa]	Elongation in 2 in. [50 mm] or 4⌀, min, %	Reduction of Area, min, %	Brinell Hardness Number, HBW
130 [895]	110 [760]	12	35	263–321

† Determined by the 0.2 % offset method.

According to the ASME pressure vessel code UG-27 [34], the formulas for the circumferential and longitudinal stress in cylindrical shells subject to internal pressure are given in equations (16) and (17) respectively.

$$t = \frac{PR}{SE - 0.6P} \tag{16}$$

$$t = \frac{PR}{2SE + 0.4P} \tag{17}$$

Where

E	1.00	dim	joint efficiency. Seamless-forgings have no joints, therefore efficiency is 1.0.
P	1500	psi	internal design pressure.
R	7.0	in	inside radius of the shell course under consideration
S	55	ksi	maximum allowable stress value. Chosen as ½ of yield strength.
t		in	minimum required thickness of shell

The minimum cylinder thickness found for circumferential stress and longitudinal stress is 0.3947 in and 0.19 in. The vessel was built with a wall thickness of 3.5 in, which yields a safety factor of 8.9.

The minimum thickness of un-stayed flat heads, cover plates and blind flanges shall conform to the requirements given the ASME Pressure Vessel Code Section VIII UG-34 [34]. The minimum required thickness of flat unstayed circular heads, covers and blind flanges shall be calculated by the following formula:

$$t = d\sqrt{CP/SE} \tag{18}$$

Where

C	0.25	dim	a factor depending upon the method of attachment of head, shell dimensions, and other items as listed in (d) below, dimensionless. End cap factor 0.25.
d	14	in	diameter, or short span, measured as indicated in Figure UG-34
E	1.0	dim	joint efficiency. Seamless forging efficiency of the joint is 1.0
P	1500	psi	internal design pressure.

The endcap does not have constant cross section; it is thinnest at the bolt flange, 2.5 inches, and much thicker in around the retaining ring thread and vent opening. Plugging the bolt flange thickness into equation (18), produces a safety factor of 1.63. The highest stress areas are very localized and limited to the fillet between the bolt flange and the cylindrical projection that is inserted into the bomb body, see Figure 30. For this reason, the fillet radius was generously sized to 0.4 in, which make it the largest fillet feature among all the bomb components.

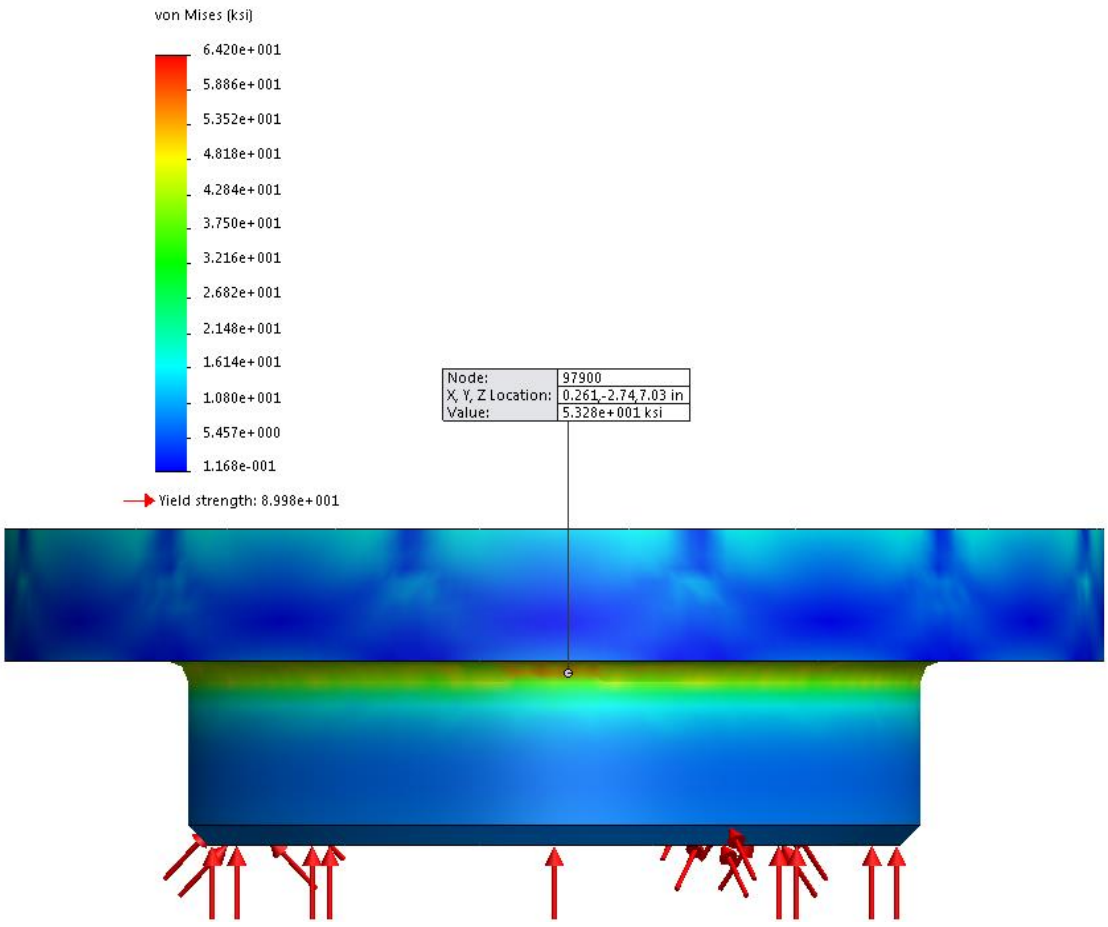

Figure 30 Von Mises stress plot of end cap, side view.

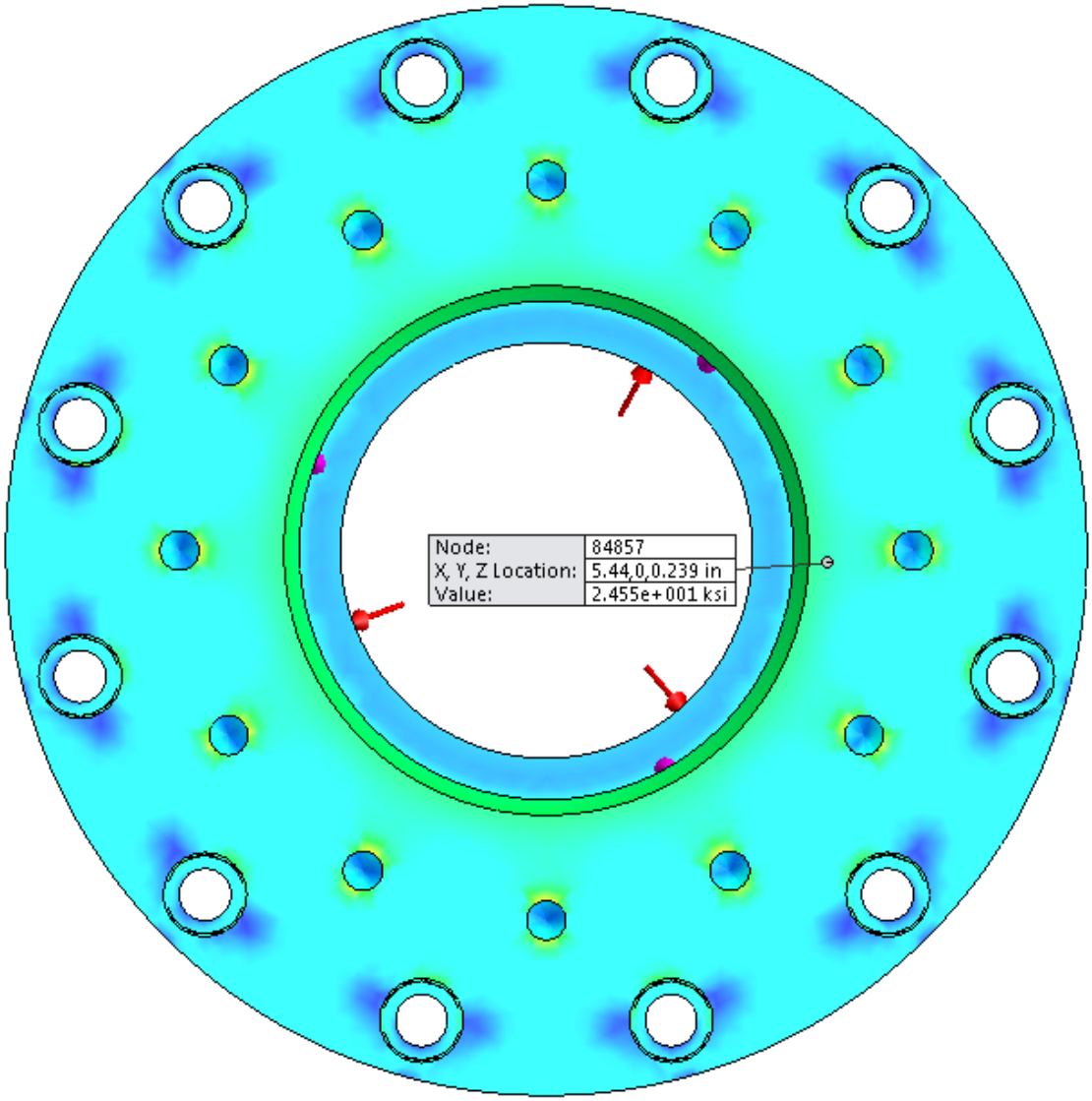

Figure 31 Von Mises stress plot of end cap, top view.

Fasteners

The selection and design of fasteners was done following the guidelines of the Machinery's Handbook [35]. The typical bolt strength is 170 ksi. For the minimum engagement length, the fact that the internal threads are machined into the forged stainless steel with a lower strength has to be considered. The forged rings strength is 110 ksi and the engagement length has been corrected so that the bolt would fail before the internal threads strip. The minimum engagement requirement was relaxed in the case of the bearing housing thread since it has a very generous safety factor. Table 10 summarizes the fasteners engineering.

The endcaps have an 8-in-diameter breech and retaining ring, Figure 32. The retaining ring holds in place accessories fitted at the breech, of which the simplest option is a plug blank, as presented in Figure 33. The thread chosen for these elements is a standard 10-3 BUTT 3A buttress screw, known for being particularly strong in one direction. Table 11 details the features of the lead screw design.

Figure 32 End cap and retaining ring.

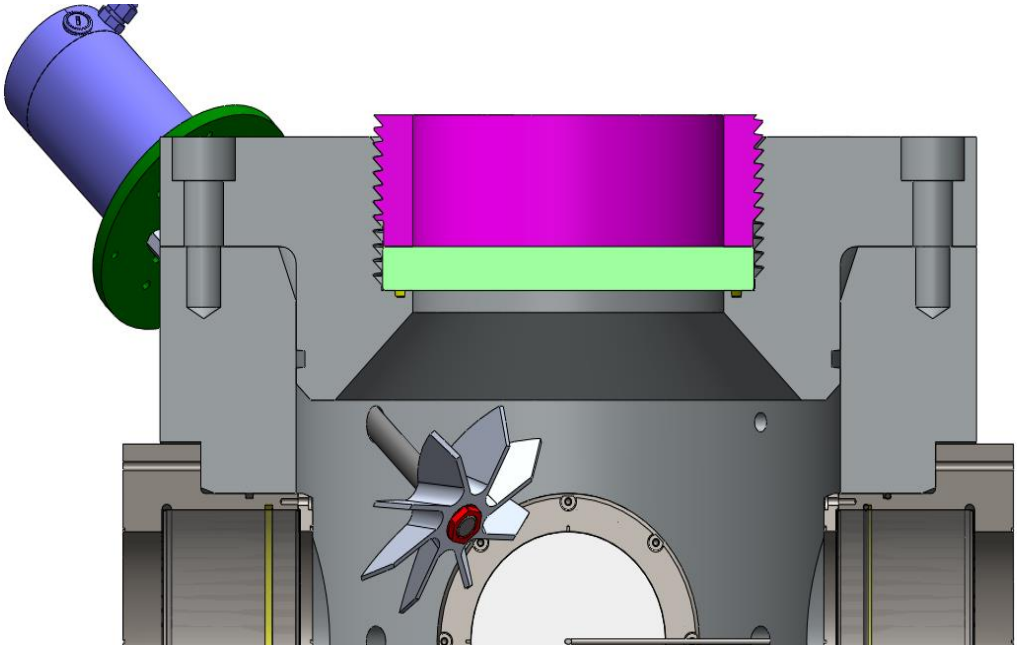

Figure 33 Detail cutaway showing the retaining ring in magenta and a blank plug disk in light green.

Table 10 Fasteners calculations.

Application	Thread	Number of fasteners	Q, corrected engagement length, in	Fastener strength, ksi	Pressure, psi	Total load, lb	Load per fastener, lb	Fastener, load capacity, lb	Safety factor
Window clamp	8-32 UNC 2A	8	0.137	180	15	416	52	2,522	48.5
Housing cover	1/4-20 UNC 2A	12	0.182	170	3,000	9,425	785	5,410	6.9
Side port	5/16-18 UNC 2A	6	0.238	170	3,000	4,455	742	8,913	12.0
Window cell	9/16-12 UNC 2A	12	0.442	170	3,000	107,355	8,946	30,931	3.5
Spark plug	1/2-14 NPT	1		110	3,000	1,663	1,663	51,277	30.8
Expansion joint	7/8-9 UNC 2A	12	0.705	170	3,000	235,619	19,635	78,495	4.0
End cap	1-8 UNC 2A	12	0.802	170	3,000	461,814	38,485	102,977	2.7
Bearing housing	2 1/4 -10 UNS 2A	1	1.853	110	3,000	2,356	2,356	400,311	169.9
Retaining ring	10-3 BUTT 3A	1	0.1439	63.5†	3,000	235,619	235,619	3,928,462	16.7

† Shear strength of buttress thread elements.

Table 11 Dimensions for 10-3 BUTT Class 3 buttress thread.

Symbol	Value	Unit	Formula	Description
D	10	in	D = 10	Major diameter (nominal)
tpi	3	threads/in	tpi = 3	Threads per inch
p	0.3333	in/thread	p = 1 / tpi	Pitch
H	0.2969	in	H = 0.89064 * p	Height of sharp V-thread
h	0.2	in	h = 0.6 * p	Basic height of thread engagement
r	0.0238	in	r = 0.07141 * p	Root radius
s	0.0275	in	s = 0.0826 * p	Root truncation for either round or flat root
S	0.0309	in	S = 0.0928 * p	Flat width of flat root form
G	0.0093	in	G = 0.0093	Allowance
h_e	0.1954	in	$h_e = h - 0.5 * G$	Height of thread engagement
f	0.0484	in	f = 0.14532 * p	Crest truncation
F	0.0544	in	F = 0.16316 * p	Crest width
D_n	10.0418	in	$D_n = D + 0.12542 * p$	Major diameter of internal thread
D_s	9.9907	in	$D_s = D - G$	Major diameter of external thread
E_n	9.8	in	$E_n = D - h$	Pitch diameter of internal thread
E_s	9.7907	in	$E_s = D - h - G$	Pitch diameter of external thread
h_n	0.2209	in	$h_n = 0.66271 * p$	Height of thread of internal thread
h_s	0.2209	in	$h_s = 0.66271 * p$	Height of thread of external thread
K_n	9.6	in	$K_n = D - 2 * h$	Minor diameter of internal thread
K_s	9.5489	in	$K_s = D - 1.32542 * p - G$	Minor diameter of external thread
L_{s45}	0.2438	in/thread	$L_{s45} = H - f - 0.5 * G$	Shear length per thread under 45 degree flank
L_s	0.2737	in/thread	$L_s = L_{s45} * (1 + \tan(7°))$	Shear length both flanks, 7° and 45°
A_s	8.5913	in^2/thread	$A_s = \pi * D_s * L_s$	Shear area per thread

RIG VALIDATION

Hydrostatic test

A hydrostatic test was performed on April 18th 2017 by FESCO, Ltd. The vessel was filled with water and then pressurized 2000 psi with a pneumatic pump, Figure 34, Figure 35, and Figure 36. No leaks or pressure loss were observed, however, one quartz window fractured. Even in its broken state, the window did not disintegrate; it continued to hold pressure without releasing water. The hydrostatic test was considered successful as the worthiness of the vessel was verified. As a corrective measure, PTFE gaskets were added to the window assembly to avoid direct contact between metal and quartz on the flat faces and minimize stress concentration, as shown in Figure 27.

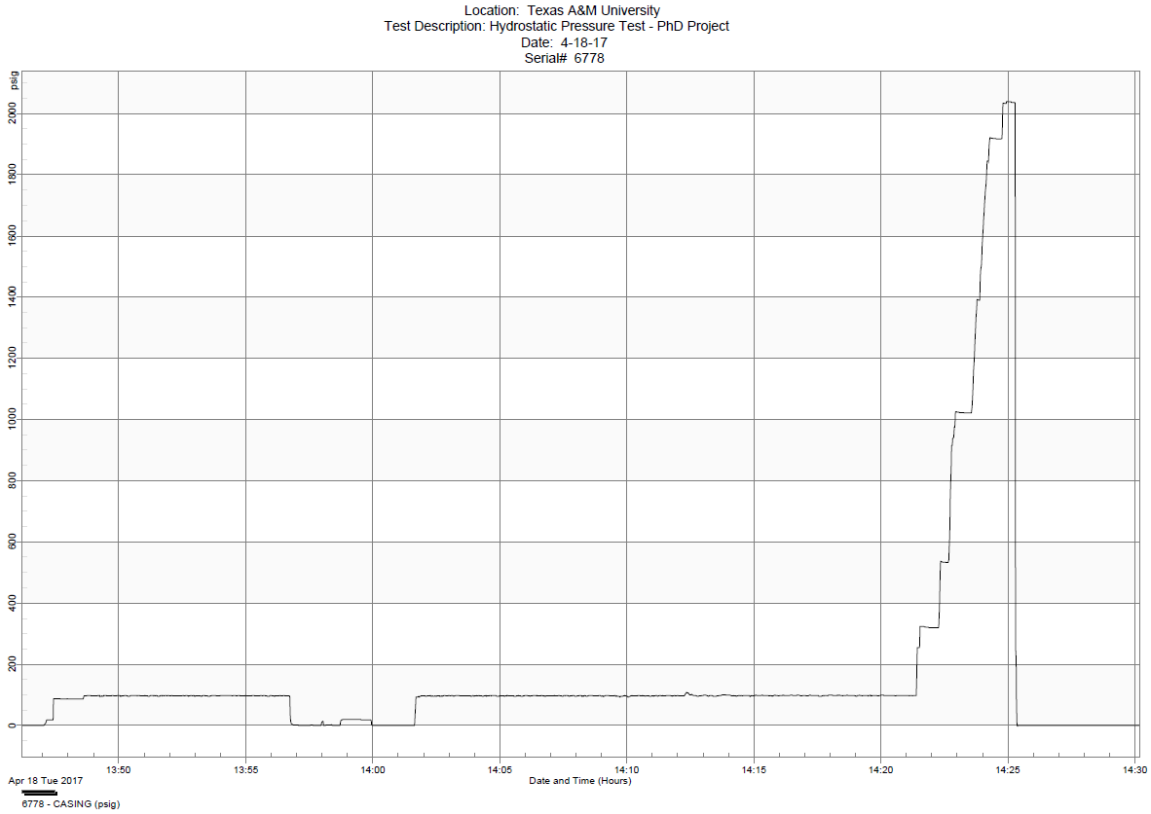

Figure 34 Hydrostatic test pressure trace.

Figure 35 Pneumatic pump and pressure transducer with data log

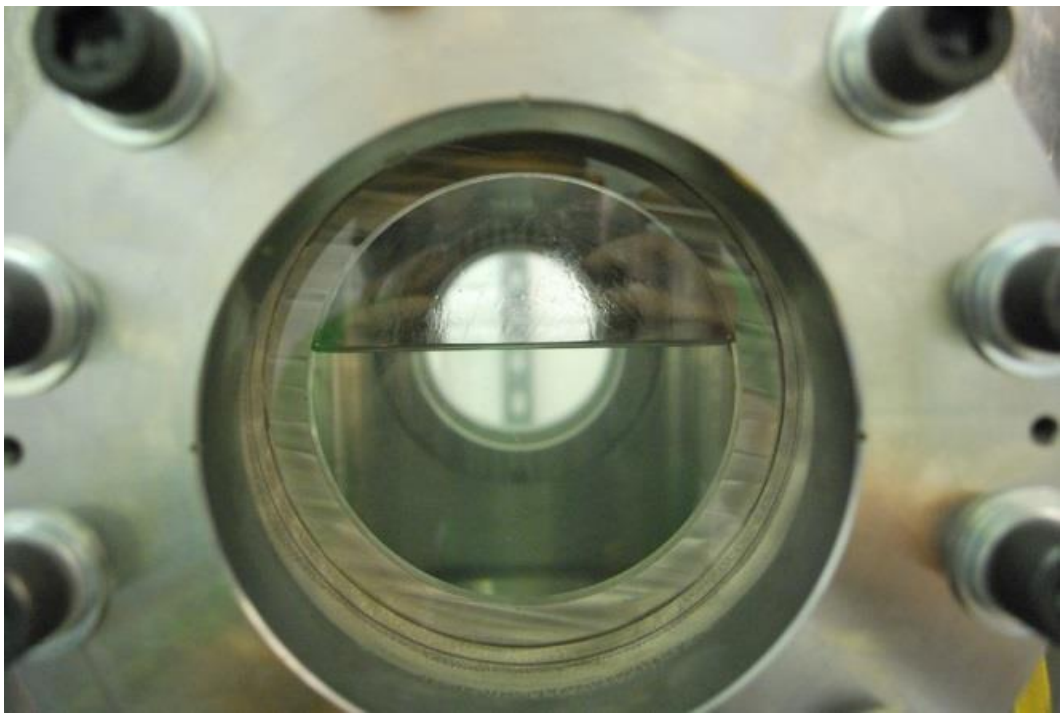

Figure 36 Water level while preparing the vessel for hydrostatic test.

The subsequent investigation showed that the quartz substrate failed due to contact stress. A fractrographic inspection by Dr. Miladin Radovic (TAMU) identified the origin of fracture and propagation direction, Figure 37. The fail started at the exterior window seat, the annular region at the bottom of the window cell socket where window substrate is supported. The fracture then branched from this point. All the quartz pieces present inclusions and defects observable with naked eye. These defects weaken the material; however it was shown that the failure started elsewhere.

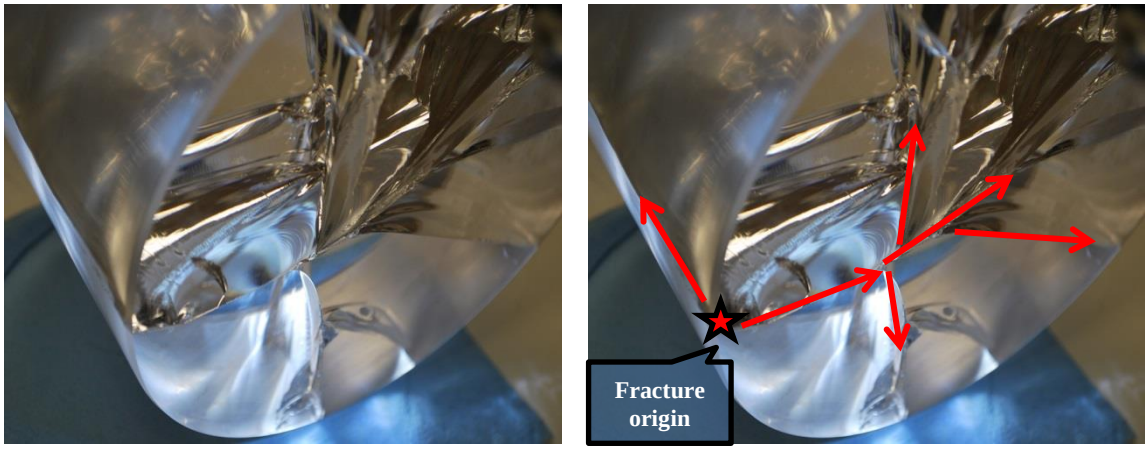

Figure 37 Fracture propagation.

Laminar flame speed validation

Since this is a new device, a validation diligence is necessary. A series of experiments with hydrogen were chosen as a figure of merit. The bomb was able to reproduce results obtained in the past by this group [36] with excellent repeatability, Figure 38.

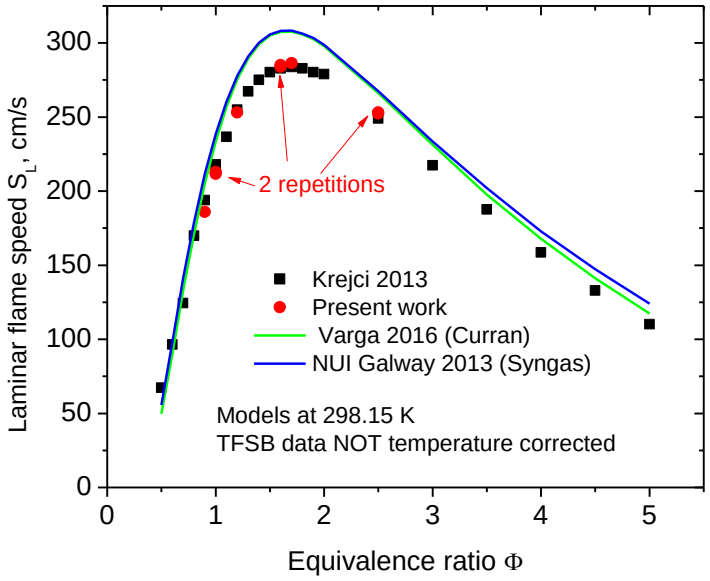

Figure 38 Laminar flame speed of hydrogen at 1 atm and room temperature. Continuous lines are recent kinetics models for hydrogen and syngas [37, 38].

The maximum operating pressure is 10 atmospheres. This figure refers to the pressure of reactants prior to ignition. The competence of the bomb under static load was judged with the hydrostatic test disclosed elsewhere in this text. A conservative rule of thumb estimates that the pegging pressure, i.e. the momentarily peak pressure, will be tenfold the initial pressure for closed volume combustion. Before commissioning the

bomb for operation at 10 atmospheres, trial experiments with aluminum window plugs where performed, Figure 39. The trials with aluminum window plugs were successful, Figure 40, and the window cells were again fitted with quartz substrates.

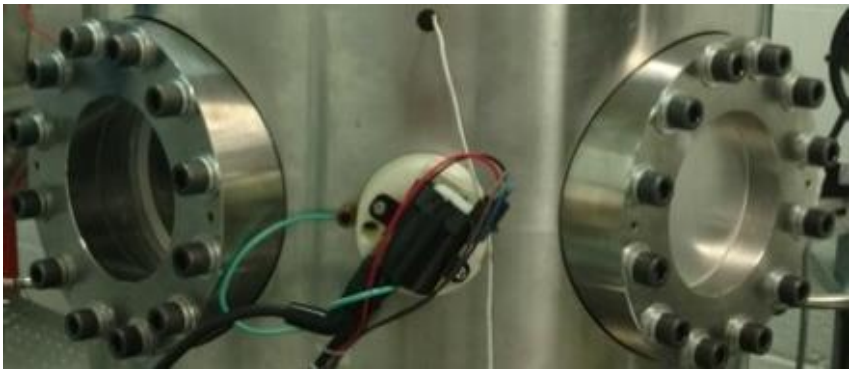

Figure 39 The quartz substrate (left) been substituted by aluminum blank (right).

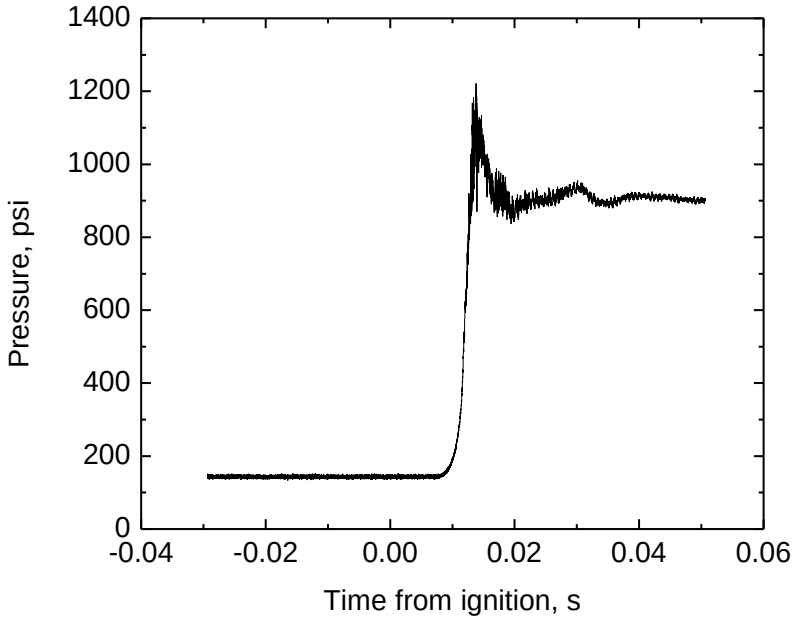

Figure 40 Pressure trace of ST Run 43. Reactants pressure was 10 atm. Stoichiometric hydrogen in air.

NOx formation

It was noticed that, after the high-pressure experiments, the combustion products when seen through the window immediately after a run had a distinctively yellow/greenish coloration, see Figure 41. The yellow shade was more intense the higher the initial pressure; in other words, combustion products of 10-bar experiments were decidedly mustard while the coloration after 2-bar runs was barely perceptible. Moreover, if the combustion gases were allow to sit in the bomb and cool down, the mustard hue faded away gradually. The water that eventually condensed inside the bomb had a bright yellow color while some surfaces were stained with a dark brown/rust patina. To minimize condensation and the residue left behind, the combustion products were vented through the ventilation system as quickly as possible. Even with the extraction system working, a pungent, biting smell was perceived for a few seconds following the exhaust release.

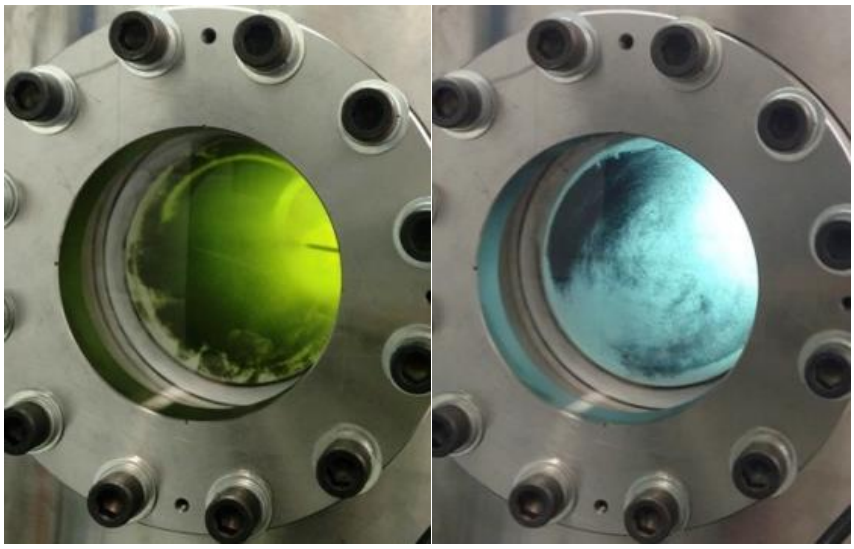

Figure 41 Combustion products after a 10 bar experiment. The oxidizer for the left side was O_2:N_2::1.0:3.76. The oxidizer for the right side was O_2:He::1:6.

Figure 42 Water condensed inside the bomb after 10-bar experiment. The oxidizer was air (O_2:N_2::1.0:3.76). Hydrogen was burned at ϕ=0.5. Top view.

It was postulated that the mustard coloration was owed to the formation of nitrogen oxides (NOx). The physical and chemical characteristics of nitrogen dioxide (NO_2) in particular fit the observations quite well, including the color (Figure 43). To test this hypothesis, a simple test was devised; to substitute nitrogen in the oxidizer for an inert gas: helium. A 10-atm run of hydrogen at an equivalence ratio of 0.5 was prepared with a mixture of oxygen and helium in the following volume ratio: O_2:He::1:6. The combustion products were odorless and colorless, see the right side of Figure 41. The condensate was also transparent. It was concluded that the coloration in the air-burning experiments was due to nitrogen oxidation. It can be said that, after the experiments, the bomb and the steam generated therein, were acting as an unintended wet scrubber. Nitrogen dioxide is highly soluble in water and decomposes in nitric acid promptly [39], which could explain why the gas phase loses the yellow color while if enough time is allowed, leaving a tarnished condensate behind.

Figure 43 Overlayed pictures taken to the same sealed ampule containing 99.9% pure NO2/N2O4 at different temperatures. From left to right -196 C, 0 C, 23 C, 35 C, 50 C. © Efram Goldberg / CC-BY-SA-3.0

Confinement effect

Flame bombs are finite volume devices, and therefore pressure is expected to increase after combustion takes place. However, in the early stages of the flame development, there is very little change in pressure. The current device demonstrated that the pressure increase during the time the flame is being recorded is negligible, see Figure 44 and Figure 45. This claim was later confirmed during the analysis. A confinement effect was not observable in the burned velocity-versus-stretch plots, see an example in Figure 46. This lack of observed confinement effect might be due to the fact that this new bomb

diameter and volume are greater than former generations [26, 27] at Texas A&M University.

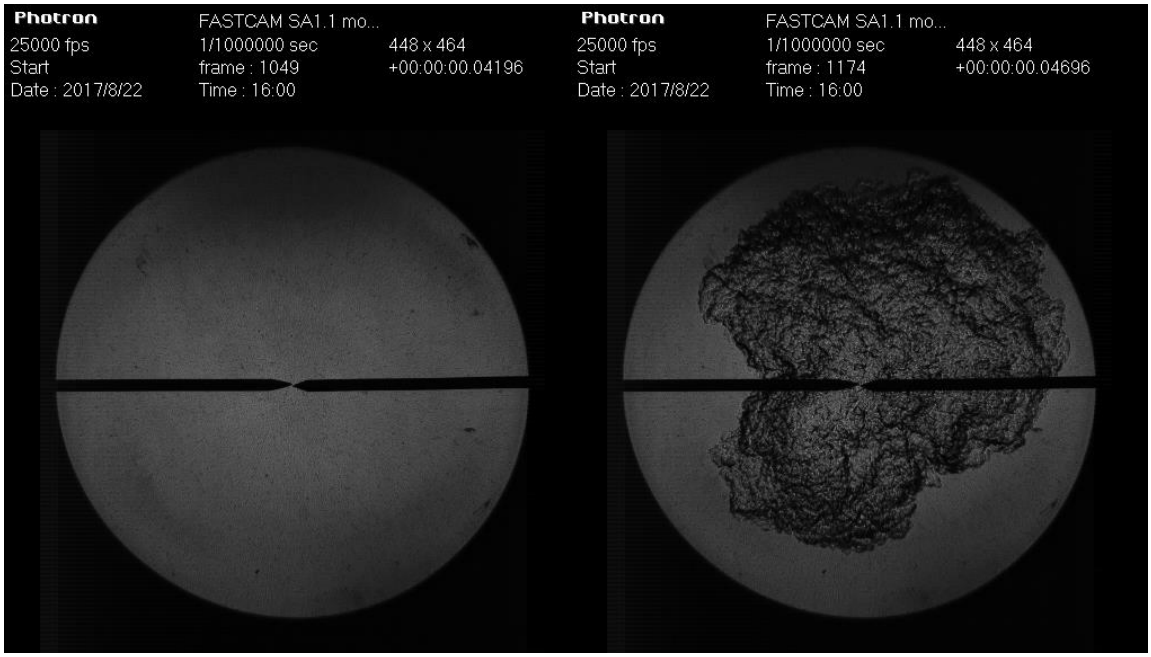

Figure 44 First and last frame of run 58. The total elapsed time is 5 ms. This is a 2-atm syngas experiment at equivalence ratio of 0.5.

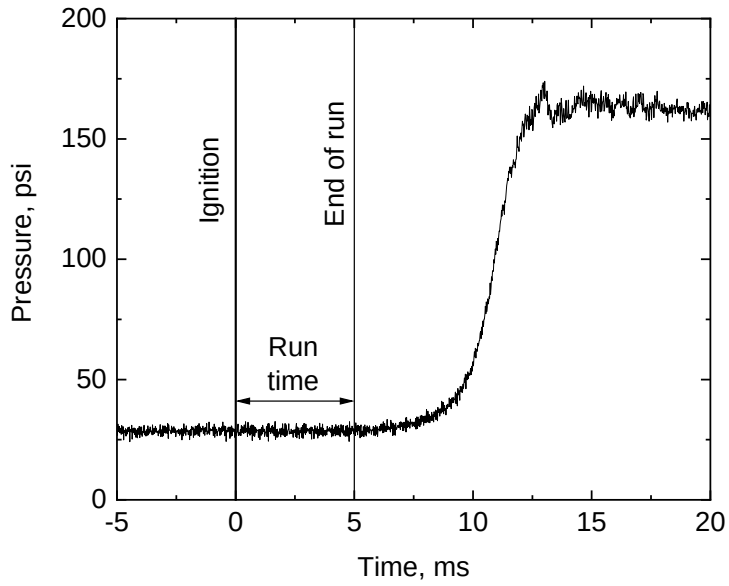

Figure 45 Pressure trace of Run 58. The flame silhouette reaches the edge of the field of view well before 5 ms mark, when the increase in pressure is not perceptible.

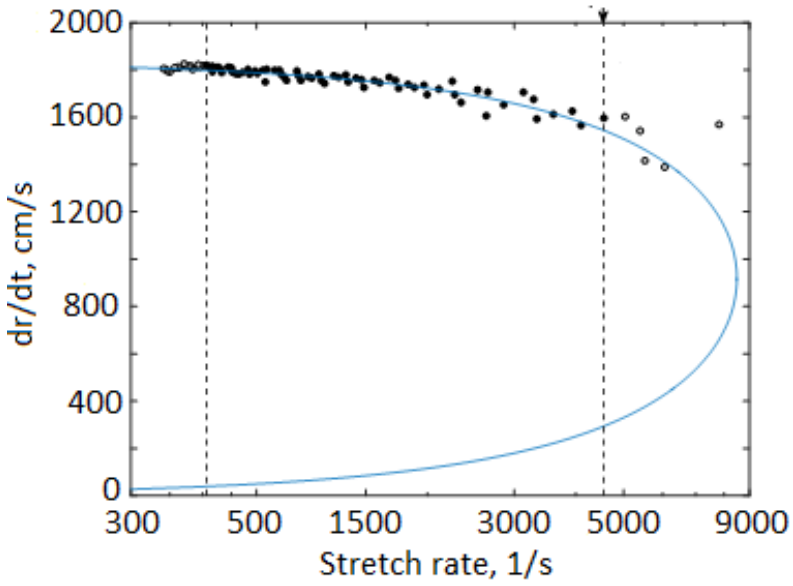

Figure 46 Burned velocity versus stretch rate for Run 10.

SYNGAS DEMOSTRATION

Experiment matrix

The fuel chosen to demonstrate the capabilities of the new rig was a mixture of hydrogen and carbon monoxide in equal volumetric proportion. The effect of pressure on the laminar flame speed of this particular mixture has been previously studied by this group [36]. Only one equivalence ratio was studied in the present work, ϕ=0.5. This mixture is the approximate air fuel composition at which syngas is burned in gas turbines [40]. The fans operated at 2000, 4000, and 8000 rpm to induce a planar turbulence fluctuation c' of 1.4, 2.8, and 5.5 m/s, respectively. Three levels of pressure, 1, 5 and 10 bar were explored, but not all combinations of shaft speed and pressure were attainable. It was not possible to run experiments at 8000 rpm for 5- and 10-bar experiments. Both the motors and the electrical installation proved to be insufficient to overcome the power demand imposed by the lip seal at high pressure. All experiments were held at room temperature. Leaf blower impellers placed near the wall stirred the gases.

The laminar flame speed, flame thickness and turbulent Reynolds number Re_T for the test matrix are in Table 12. The integral length scale of the turbulence, L_T, is typically derived from spatial correlations computed from instantaneous snapshots of the flow field. Particle Image Velocimetry (PIV) is the preferred tool for such analysis. Unfortunately, PIV was not available for this study and L_T was assumed to be equal to the length of the leading edge of the impeller, i.e. 20 mm. The lack of information about the spatial coherence also prevented the spectral analysis of wavelengths. The spectral distribution

could have been used to estimate the energy dissipation rate. A crude approximation to the energy dissipation rate can be obtained from the ratio of power taken from the electrical grid and the mass trapped in the bomb. The average energy dissipation rate must be less than such quotient since the motor and drive train power losses are unaccounted.

Table 12 Laminar flame properties and turbulent Re of test mixture at Φ = 0.5, L_T = 20 mm, T = 300 K.

	$S_{L,u}^{\circ}$	δ_{∇}	δ_{α}	$\mathrm{Re}_T = c'L_T/\nu$		
	m/s	**µm**	**µm**	**1.4 m/s**	**2.8 m/s**	**5.5 m/s**
1 bar	0.269	649	107	1621	3242	6369
5 bar	0.130	195	45	8116	16,231	
10 bar	0.081	142	36	16,185	32,370	

The laminar flame thickness has multiple definitions. The thermal diffusivity thickness δ_{α}, shown in Eq. (19), is derived from dimensional arguments as the ratio of the thermal diffusivity of the fresh reactants and laminar flame speed. This definition is not the only diffusive thickness, and some authors prefer to assess the flame thickness in terms of other transport properties. In fact, it is not uncommon find all transport properties to be assumed numerically equal in some derivations (i.e. $\alpha = D = \upsilon$). This treatment is implicit in the construction of Borghi diagrams, since curves of constant Reynolds number are shown up as straight lines in the logarithmic space. The permute of momentum and thermal diffusivity is defensible for air in a wide range of temperatures as the Prandtl number stays somewhat close to unity ($\mathrm{Pr} \equiv \nu/\alpha \approx 0.7$) and allows expression (20) for the Reynolds number.

$$\delta_\alpha = \frac{\lambda_u}{\rho_u c_P S_L} = \frac{\alpha}{S_L} \tag{19}$$

$$\mathrm{Re}_T\big|_{\mathrm{Pr}=1} = \frac{u' L_i}{\delta_\alpha S_L} \tag{20}$$

Where

δ_α	m	thermal diffusivity flame thickness.
λ_u	W/m^2-K	thermal conductivity of reactants
ρ_u	kg/m^3	density of reactants
c_P	J/kg-K	heat capacity at constant pressure
α	m^2/s	thermal diffusivity

Other definitions of the flame thickness are formulated from the temperature profile across the flame front. Figure 47 can be used to illustrate the temperature gradient thickness δ_∇ which is obtained by extending a tangent line from the point of maximum slope to intersect the steady state temperature line of reactants and products. This temperature gradient definition, expressed in Eq. (21), is usually 5 times larger than the thermal diffusivity thickness (i.e. $\delta_\nabla \approx 5\,\delta_\alpha$) and is useful as a first approach to set the grid size in numerical simulations [41]. The total flame thickness δ_{total}, which measures the distance needed by the combustion products to reach the final equilibrium temperature starting from the fresh gases temperature, is also depicted in Figure 47.

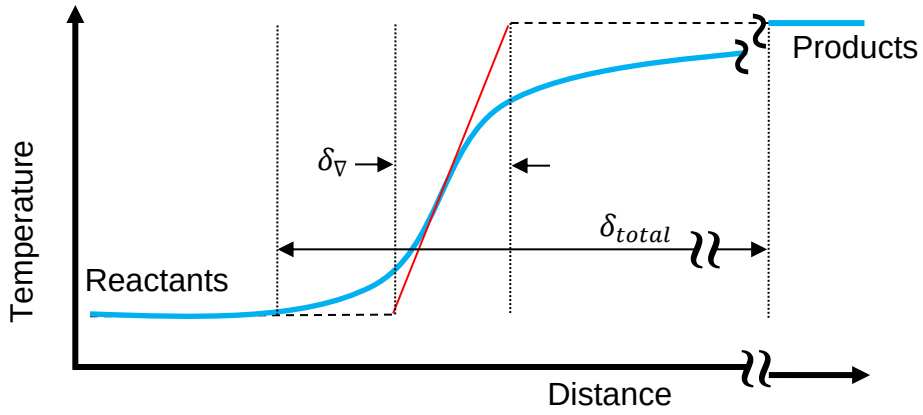

Figure 47 Mock temperature profile of a flame. The steepest rise and steady state temperature of the products and reactants define the thermal gradient flame thickness, δ_∇. The total flame thickness, δ_{total}, is much larger.

$$\delta_\nabla = \frac{T_b - T_u}{\max\left(\left|\frac{dT}{dx}\right|\right)} \tag{21}$$

Where

δ_∇	m	thermal gradiente flame thickness.
δ_{Total}	m	total flame thickness
T_u	K	temperature of reactants.
T_b	K	equilibrium temperature of combustion products.
x	m	coordinate along flame propagation

All conditions tested in this work fall in the thin reaction zone as when represented in a Borghi diagram like Figure 48.

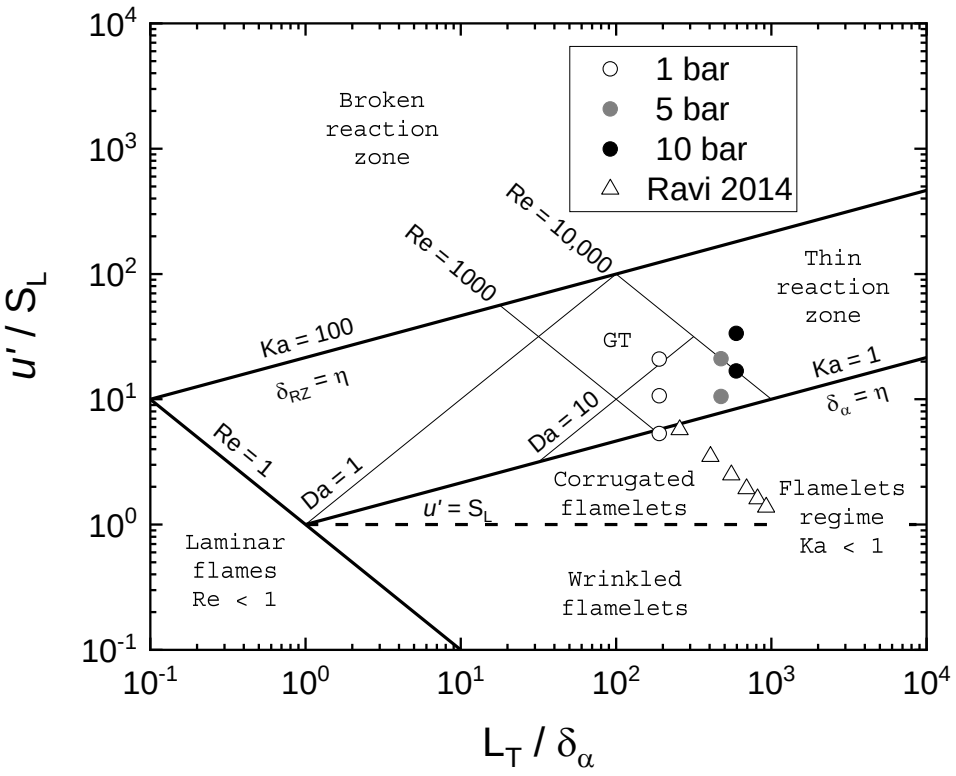

Figure 48 Borghi diagram with test conditions attained in this work

Results and discussion

A Photron high-speed camera, Fastcam SA1.1 was used to acquire schlieren images at 25,000 frames per second. Figure 49 provides one example of turbulent flame picture. The still images were post-processed with a Matlab script that finds the edge of the window and flame. The area occupied flame silhouette is tallied, and the radius of a circle with the same area is calculated for every frame. With this information, it is possible to plot the equivalent flame radius over time. The radius development of four repetitions

of one test condition is displayed in Figure 50. In all repetitions shown in Figure 50, acceleration is clearly noticeable as the flame grows. The stochastic nature of this phenomenon is manifested the spread of repetitions. This behavior is in line with the observations of other research groups.

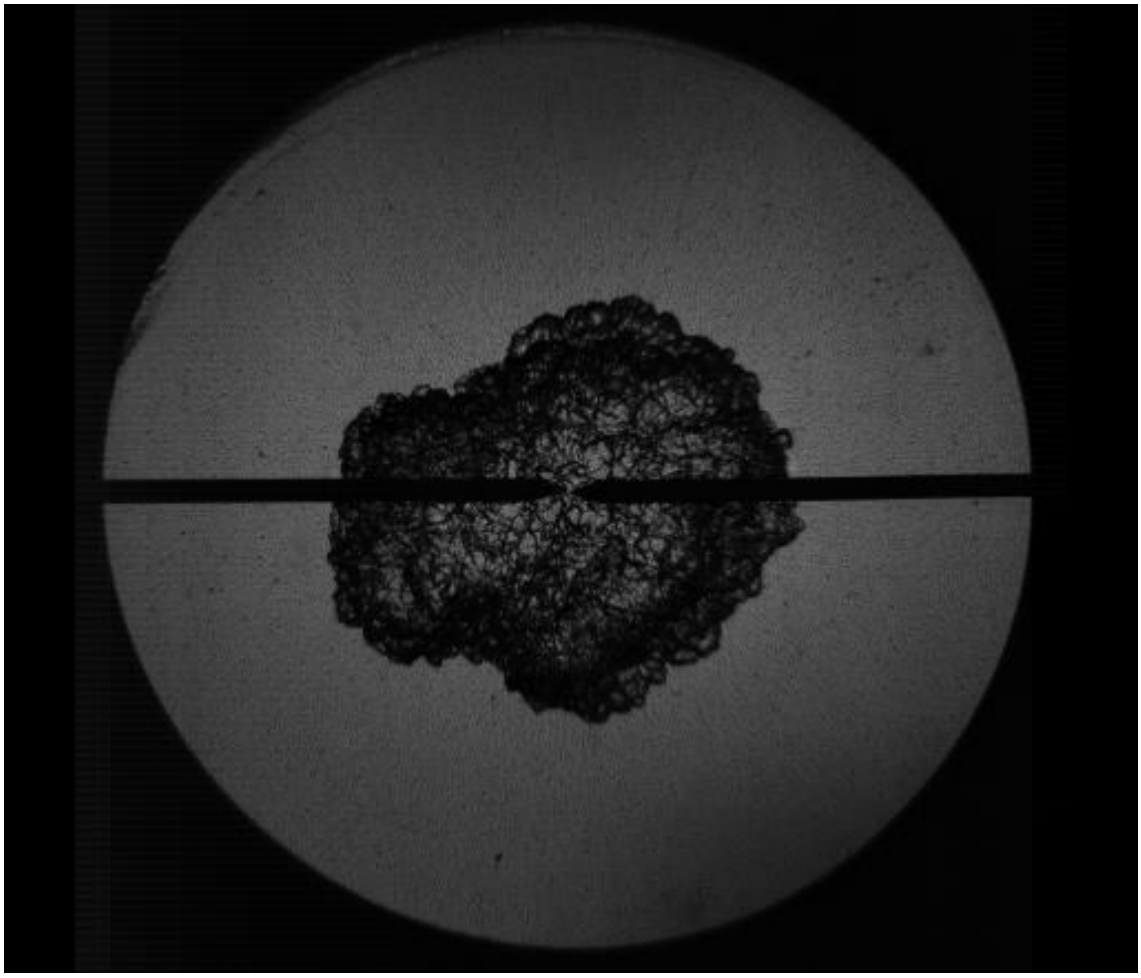

Figure 49 Schlieren image of a syngas flame stirred at 2000 rpm. The initial pressure was 5 bar. Approximately 0.6 ms have elapsed since ignition.

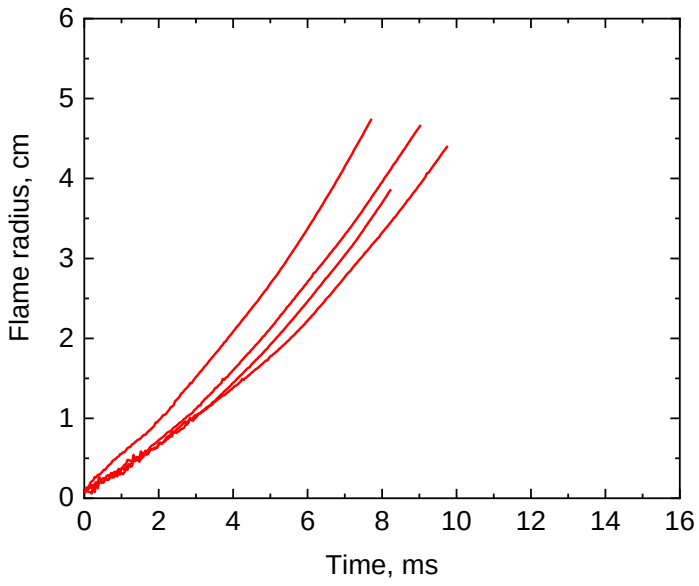

Figure 50 Radius history of four test repetitions at 2000 rpm and 1 bar.

The effect of the fan speed on flame acceleration is larger than the scatter exhibited by the runs. Three distinct groups of curves can be observed in Figure 51. The faster the shaft speed the quicker the radius grows. Experiments at 2000 rpm presented more scatter than those conducted at 4000 and 8000 rpm.

Figure 52 presents the results for all 4000-rpm runs. The effect of pressure is not evident in the flame radius growth rate, at least when the fans spin at 4000 rpm. All tests at this shaft speed collapse over the same region, regardless of the initial pressure. A master plot of flame radius for all runs is provided in Figure 53.

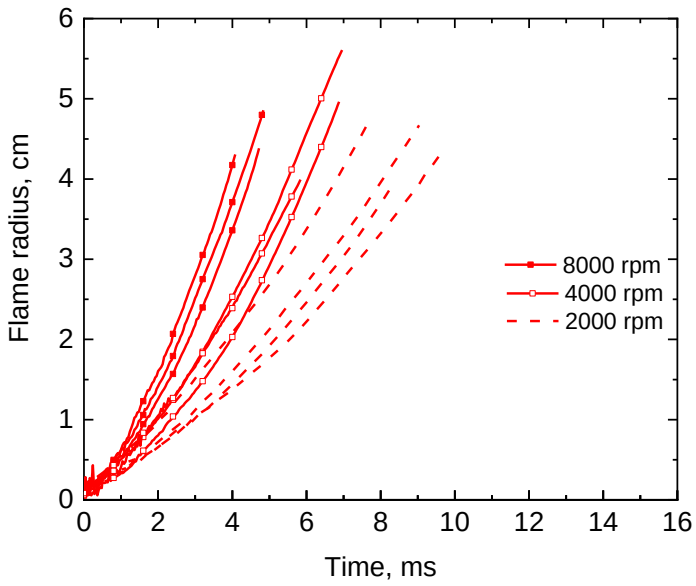

Figure 51 Effect of shaft speed on flame radius development. The initial pressure of all runs shown here is 1 bar.

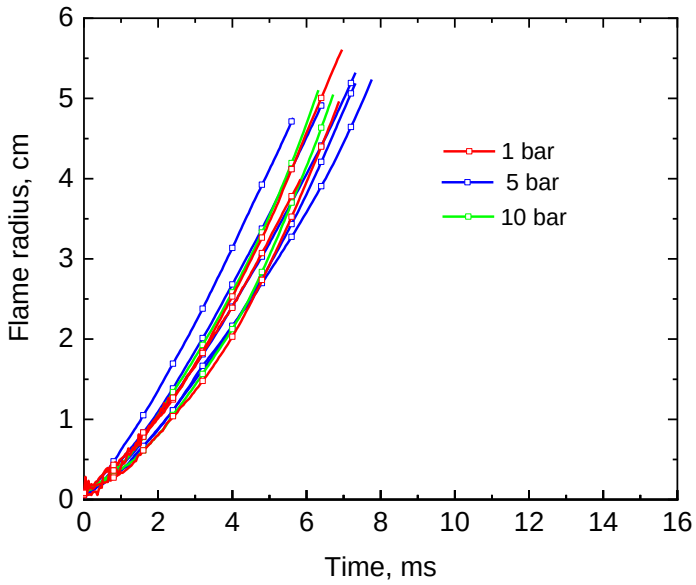

Figure 52 Pressure effect on flame radius development. All runs at 4000 rpm.

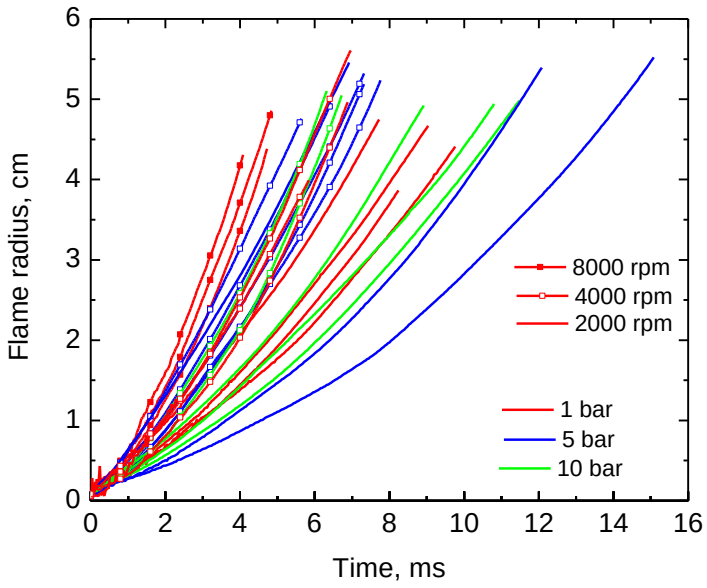

Figure 53 Flame radius as a function of time. All runs are included here.

Turbulent displacement velocity of the burned gases is obtained by numerical differentiation of the radius-versus-time curves. This procedure yields noisy derivatives, so the radii history was smoothed with a Savitsky-Golay method (2nd order polynomial, 10 points per window). To further reduce the data, the repetitions were averaged.

The results at 1 bar for all shaft speeds are condensed in Figure 54. The promoting effect of shaft speed on the turbulent displacement speed of the burned is confirmed. The effect of pressure is not as straightforward. Figure 55 collects results for 1, 5, and 10 bar. No conclusion can be drawn from the experiments done at 4000 rpm for the different pressure levels, as previously observed in radius growth plots. At 2000 rpm, a difference between the pressure treatments can be identified, but it does not line up with the

expectation of laminar flame speed scaling. In Figure 55, the turbulent displacement speed average for 1-bar tests is the highest, followed by the results at 10 bar, which are in turn trailed by the 5-bar runs. This order does not correspond to their respective laminar flame speed.

It has to be recognized that the amount of repetitions per treatment in this test program is low compared to other authors. Goulier and coworkers tested 10 times per condition [42], to cite an example. The inherent variability of the spherically expanding flames in turbulent environment demands abundance of measurements to produce statistically meaningful conclusions.

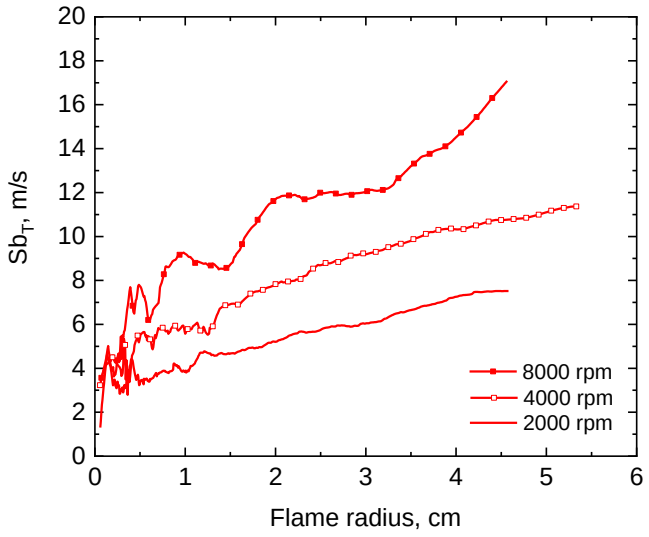

Figure 54 Flame speed to the burned gases at 1 bar.

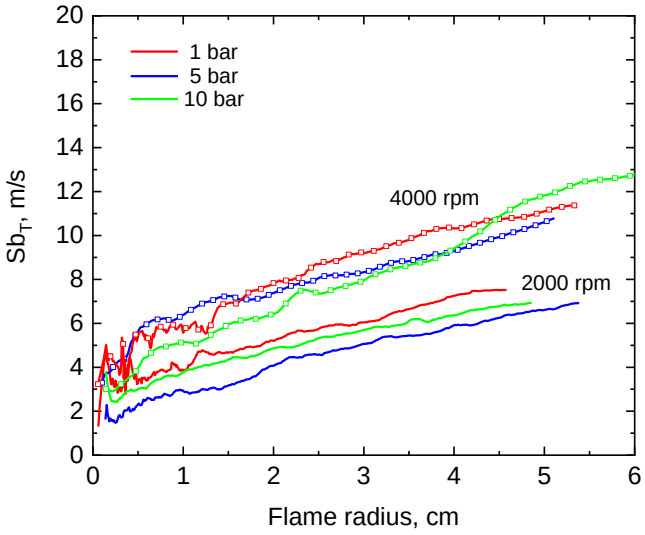

Figure 55 Displacement velocity of burned gases stirred at 2000 and 4000 rpm for all pressure levels.

CONCLUSIONS

The need of devices capable of measuring of fundamentals properties of turbulent combustion at high temperature and high pressure was identified. To the author's best knowledge, prior to this contribution, there was only one fan-stirred flame bomb in the world capable of creating a turbulence fluctuation intensity higher than 5 m/s that also has access to elevated temperature and pressure.

Rough guidelines for the selection of impellers were formulated. In general, large-diameter impellers are better stirrers in terms of the turbulence fluctuation produced. It was found that the impeller design has a big impact on the power demanded to drive it. It was also learned that it was possible to affect some properties of the flow by changing the location of the impeller along the shaft. This last finding permitted to achieve near-isotropic turbulence (i.e. $u'/w' \approx 1.0$) when the impeller was installed in close clearance with the vessel wall. However, the ratio of turbulence fluctuation to average speed was deteriorated and increased from 0.2 to 0.33.

The details of key features of the new fan-stirred flame bomb were exposed. In terms of optical access, the bomb developed in this work is superior to the previous generations built at the Turbomachinery Laboratory of Texas A&M University. The new apparatus has 4 windows with a clear aperture of 5 inches arranged in two perpendicular lines of sight. The windows will enable combustion diagnostics and flow measurement techniques that were not possible past iterations.

The temperature operation ceiling is set by the elastomeric materials chosen for the seals. In the as-built condition, 200°C should be within reach. Safety factors are in

place to test combustible mixtures at 10-bar initial pressure. The highest turbulence fluctuation rms used during the demonstration experiments was 5.5 m/s. These are not the most demanding specifications achieved worldwide, but they are not trivial either. Furthermore, preparations were made to modify the vessel and extended the experiment domain.

The experiment setup as a whole was able to reproduce laminar flame speed benchmarks and demonstrated excellent repeatability. The vessel also showed that the entire field of view is usable without concerns of confinement. For the first time, the presence of NOx was noticed and diagnosed in the flame bombs built at the Turbomachinery Laboratory.

The new experimental apparatus demonstrated competence in a series of syngas turbulent flame speed experiments. The full range of pressure domain was exacted without issues, even at 8000 rpm. General trends of the effect of turbulence were in line with expectation, but not enough information was obtained to gain insight on the role of pressure.

RECOMMENDATIONS FOR FUTURE WORK

The shortcomings of the present dissertation and the recommendations for future work are listed below.

1. The turbulence characterization is not complete without measuring the length scale and the spectrum distribution of energy. This information will enable more sophisticated analysis and understanding. Systematic PIV measurements are recommended.
2. The shaft and rotary seals were designed for 10000 rpm, however it was not possible to attain the maximum speed at all pressure conditions. The load on the motor increases with pressure due to the friction that the seal exerts on the shafts. A revised electrical installation and more powerful motors are needed to spin the stirring assembly at elevated pressures.
3. The limitations in the electrical installation and motor choice was also evident during the characterization of the impeller prototypes. Gaps were left in the characterization of impellers when the power required to drive them exceeded the power available in motor and/or the laboratory electrical system. Future researchers may want to revisit the characterization of the impellers as some of them have potential to produce turbulent flows even more intense than those used in the present work.
4. The vessel was built with a large breech on each end cap. One possible adaptation of this feature is to convert the closed-volume bomb into a vented deflagration device. The venting of deflagrations is a worthy research topic on its own, but it could also be exploited to access higher pressures in spherically expanding flame experiments.

5. The heating capability of the device was not fully developed and will need to be revisited by future researchers to unlock experimental conditions at elevated temperature.
6. Applying advanced combustion diagnostics are perhaps the greatest task left to my successors. I intentionally designed the bomb with two optical axes to enable laser diagnostics and PIV flow measurements. I also left ports in excess for a purpose that I cannot foresee, but I hope that they will be useful in the future.

REFERENCES

[1] Damköhler, G., 1940, "Der Einfluss der Turbulenz auf die Flammengeschwindigkeit in Gasgemischen," Zeitschrift für Elektrochemie und angewandte physikalische Chemie, 46(11), pp. 601-626.

[2] Chen, J. H., 2011, "Petascale direct numerical simulation of turbulent combustion—fundamental insights towards predictive models," Proceedings of the Combustion Institute, 33(1), pp. 99-123.

[3] McIlroy, A., McRae, G., Sick, V., Siebers, D. L., Westbrook, C. K., Smith, P. J., Taatjes, C., Trouve, A., Wagner, A. F., Rohlfing, E., Manley, D., Tully, F., Hilderbrandt, R., Green, W., Marceau, D., O'Neal, J., Lyday, M., Cebulski, F., Garcia, T. R., and Strong, D., 2006, "Basic Research Needs for Clean and Efficient Combustion of 21st Century Transportation Fuels," USDOE Office of Science.

[4] Pope, S. B., 2013, "Small scales, many species and the manifold challenges of turbulent combustion," Proceedings of the Combustion Institute, 34(1), pp. 1-31.

[5] Environmental Protection Agency, and National Highway Traffic Safety Administration, 2012, "2017 and later model year light-duty vehicle greenhouse gas emissions and corporate average fuel economy standards," D. o. Transportation, ed., Federal Register, pp. 62623-63200.

[6] Abdel-Gayed, R. G., Al-Khishali, K. J., and Bradley, D., 1984, "Turbulent burning velocities and flame straining in explosions," Proceedings of the Royal Society of London. Series A, Mathematical and physical sciences, 391(1801), pp. 393-414.

[7] Fansler, T. D., and Groff, E. G., 1990, "Turbulence characteristics of a fan-stirred combustion vessel," Combustion and Flame, 80(3-4), pp. 350-354.

[8] Groff, E. G., 1987, "An experimental evaluation of an entrainment flame-propagation model," Combustion and Flame, 67(2), pp. 153-162.

[9] Groff, E. G., 1982, "The cellular nature of confined spherical propane-air flames," Combustion and Flame, 48(0), pp. 51-62.

[10] Haq, M. Z., 1998, "Fundamental Studies of Premixed Combustion," Ph.D., The University of Leeds, Leeds, UK.

[11] Sick, V., Hartman, M. R., Arpaci, V. S., and Anderson, R. W., 2001, "Turbulent scales in a fan-stirred combustion bomb," Combustion and Flame, 127(3), pp. 2119-2123.

[12] Smallbone, A., Tsuneyoshi, K., and Kitagawa, T., 2006, "Turbulent and stable/unstable laminar burning velocity measurements from outwardly propagating spherical hydrogen-air flames at elevated pressures," Journal of Thermal Science and Technology, 1(1), pp. 31-41.

[13] Kitagawa, T., Nakahara, T., Maruyama, K., Kado, K., Hayakawa, A., and Kobayashi, S., 2008, "Turbulent burning velocity of hydrogen–air premixed propagating flames at elevated pressures," International Journal of Hydrogen Energy, 33(20), pp. 5842-5849.

[14] Weiß, M., 2008, "Untersuchung von Flammenfrontstreckungseffekten auf die sphärische Flammenausbreitung laminarer und turbulenter Brennstoff/Luft-Gemische," Ph.D., Karslruhe University, Germany.

[15] Weiß, M., Zarzalis, N., and Suntz, R., 2008, "Experimental study of Markstein number effects on laminar flamelet velocity in turbulent premixed flames," Combustion and Flame, 154(4), pp. 671–691.

[16] Liu, C. C., Shy, S. S., Chen, H. C., and Peng, M. W., 2011, "On interaction of centrally-ignited outwardly-propagating premixed flames fully-developed isotropic turbulence at elevated pressure," Proceedings of the Combustion Institute, 33(1), pp. 1293-1299.

[17] Liu, C. C., Shy, S. S., Chiu, C. W., Peng, M. W., and Chung, H. J., 2011, "Hydrogen/carbon monoxide syngas burning rates measurements in high-pressure quiescent and turbulent environment," International Journal of Hydrogen Energy, 36(14), pp. 8595-8603.

[18] Peng, M. W., 2010, "Measurements of Laminar and Turbulent Burning Velocities for Centrally-Ignited, Outwardly Propagation Premixed Flames at Elevated Pressure," M.S., National Central University, Taiwan, Taiwan.

[19] Shy, S. S., I, W. K., and Lin, M. L., 2000, "A new cruciform burner and its turbulence measurements for premixed turbulent combustion study," Experimental Thermal and Fluid Science, 20(3-4), pp. 105-114.

[20] Chaudhuri, S., Wu, F., and Law, C. K., 2012, "Turbulent Flame Speed Scaling for Expanding Flames with Markstein Diffusion Considerations," arXiv preprint arXiv:1203.1029.

[21] Chaudhuri, S., Wu, F., Zhu, D., and Law, C. K., 2012, "Flame Speed and Self-Similar Propagation of Expanding Turbulent Premixed Flames," Physical Review Letters, 108(4), p. 044503.

[22] Ravi, S., Peltier, S. J., and Petersen, E. L., 2013, "Analysis of the impact of impeller geometry on the turbulent statistics inside a fan-stirred, cylindrical flame speed vessel using PIV," Experiments in Fluids, 54(1).

[23] Morones Ruelas, A., 2015, "Turbulence Measurements in a Fan-Stirred Flame Bomb Using Laser Doppler Velocimetry," M.S., Texas A&M University, College Station, TX.

[24] Galmiche, B., Mazellier, N., Halter, F., and Foucher, F., 2014, "Turbulence characterization of a high-pressure high-temperature fan-stirred combustion vessel using LDV, PIV and TR-PIV measurements," Experiments in Fluids, 55(1), pp. 1-20.

[25] Goulier, J., Chaumeix, N., Halter, F., Meynet, N., and Bentaïb, A., 2017, "Experimental study of laminar and turbulent flame speed of a spherical flame in a fan-stirred closed vessel for hydrogen safety application," Nuclear Engineering and Design, 312, pp. 214-227.

[26] De Vries, J., 2009, "A study on spherical expanding flame speeds of methane, ethane, and methane/ethane mixtures at elevated pressures.," Ph.D., Texas A&M University, College Station, Texas.

[27] Krejci, M. C., 2012, "Development of a New Flame Speed Vessel to Measure the Effect of Steam Dilution on Laminar Flame Speeds of Syngas Fuel Blends at Elevated Pressures and Temperatures," MS, Texas A&M University, College Station, Tx.

[28] Ravi, S., 2014, "Measurement of turbulent flame speeds of hydrogen and natural gas blends (C1-C5 alkanes) using a newly developed fan-stirred vessel," Ph.D., Texas A&M University, College Station, Texas.

[29] Morones, A., Leon, V. J., and Petersen, E. L., 2017, "Reconfigurable Fan-Stirred Flame Bomb with Optical Access," 55th AIAA Aerospace Sciences Meeting, American Institute of Aeronautics and Astronautics.

[30] Abdel-Gayed, R. G., 1978, "Mechanisms of turbulent flame propagation," Ph.D., University of Leeds.

[31] Andrews, G. E., Bradley, D., and Lwakabamba, S. B., 1975, "Measurement of turbulent burning velocity for large turbulent Reynolds numbers," Symposium (International) on Combustion, 15(1), pp. 655-664.

[32] Harris, D. C., 1999, Materials for infrared windows and domes: properties and performance, SPIE Optical Engineering Press, Bellingham, Wash.

[33] ASTM. A182/A182M - 16a, "Standard Specification for Forged or Rolled Alloy and Stainless Steel Pipe Flanges, Forged Fittings, and Valves and Parts for High-Temperature Service," ASTM International, 2016

[34] ASME. Section VIII Rules for Construction of Pressure Vessels, "ASME boiler and pressure vessel code," ASME, 2015

[35] Oberg, E., Jones, F. D., Horton, H. L., and Ryffel, H. H., 2012, Machinery's Handbook (29th Edition) & Guide to Machinery's Handbook, Industrial Press.

[36] Krejci, M. C., Mathieu, O., Vissotski, A. J., Ravi, S., Sikes, T. G., Petersen, E. L., Kérmonès, A., Metcalfe, W., and Curran, H. J., 2013, "Laminar Flame Speed and Ignition Delay Time Data for the Kinetic Modeling of Hydrogen and Syngas Fuel Blends," Journal of Engineering for Gas Turbines and Power, 135(2), pp. 021503-021501-021503-021509.

[37] Kéromnès, A., Metcalfe, W. K., Heufer, K. A., Donohoe, N., Das, A. K., Sung, C.-J., Herzler, J., Naumann, C., Griebel, P., Mathieu, O., Krejci, M. C., Petersen, E. L., Pitz, W. J., and Curran, H. J., 2013, "An experimental and detailed chemical kinetic modeling study of hydrogen and syngas mixture oxidation at elevated pressures," Combustion and Flame, 160(6), pp. 995-1011.

[38] Varga, T., Olm, C., Nagy, T., Zsély, I. G., Valkó, É., Pálvölgyi, R., Curran, H. J., and Turányi, T., 2016, "Development of a Joint Hydrogen and Syngas Combustion Mechanism Based on an Optimization Approach," International Journal of Chemical Kinetics, 48(8), pp. 407-422.

[39] Clean Air Technology Center (MD-12), 1999, "Nitrogen oxides (NOx): why and how they are controlled," No. EPA-456/F-99-006R, U.S. Environmental Protection Agency, Research Triangle Park, N.C.

[40] Lefebvre, A. H., and Ballal, D. R., 2010, Gas turbine combustion : alternative fuels and emissions. 3rd ed. authors, Arthur H. Lefebvre, Dilip R. Ballal, Taylor & Francis, Boca Raton, FL.

[41] Poinsot, T., and Veynante, D., 2012, Theoretical and numerical combustion, http://elearning.cerfacs.fr, Bordeaux, France.

[42] Goulier, J., Comandini, A., Halter, F., and Chaumeix, N., 2017, "Experimental study on turbulent expanding flames of lean hydrogen/air mixtures," Proceedings of the Combustion Institute, 36(2), pp. 2823-2832.

[43] Bell, W., "Spectral analysis of laser velocimeter data with the slotted correlation method," Proc. Proceedings of the AIAA/ASME Fourth Fluid Mechanics, Plasma Dynamics and Lasers Conference.

APPENDIX

DC motor Performance chart at 90 Vdc

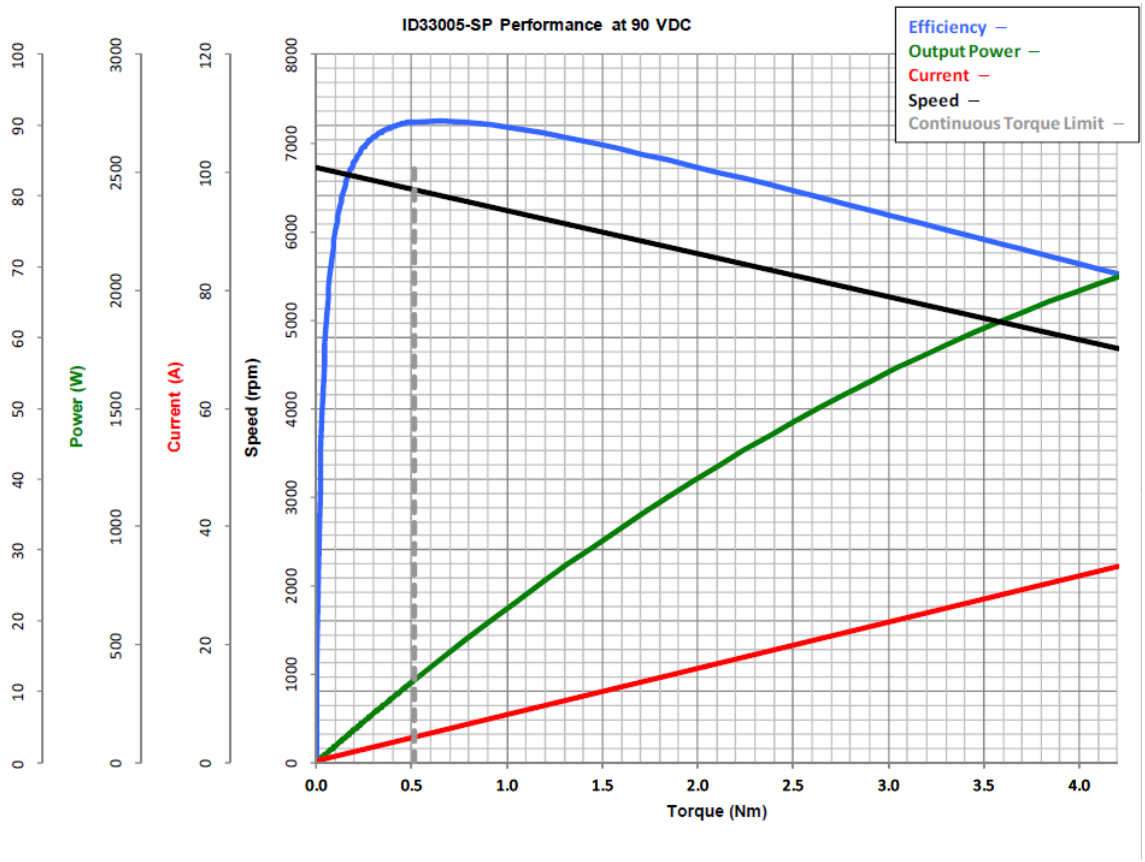

All values are nominal at 25°C. Peak torque and peak current are theoretical values. Curves are shown for reference only. Visit www.pittman-motors.com.

List of stirring assembly part numbers

Component	Model/part number	Manufacturer
Shaft	TFSB-05 REV4.1	Rave Gears and Machining
Bearing housing	TFSB-06 REV3.0	Rave Gears and Machining
Housing cover	TFSB-09 REV3.0	TAMU Physics Machine Shop
Motor flange	TFSB-10 REV3.2	TAMU Physics Machine Shop
Impeller adapter	TFSB-16 REV2.0	Mattias Turner
Impeller	Metal Impeller Asm 127-7092	Toro
Guide bearing	6203-2Z	SKF
Thrust bearing	3203 A-2ZTN9/C3	SKF
Lip seal	0102FFC18700625260SVM	Parker
V-ring	400130	SKF
Lock nut	NSH-03	Whittet-Higgins
O-rings	224, 222 (all viton)	Parker
Shaft-hub connector	Trantorque Mini 5/8 6410063	Fenner Drives
Shaft coupling	BC26-8-8-A	Ruland
Standoff bolts	Standoff bolt 91075A033	McMaster-Carr
Bearing spacers	CLBU30-40-12.7	Misumi

Seamless rings heat treatment

All Metals & Forge Group

75 Lane Road
Fairfield, New Jersey 07004

Ferrous & Non-Ferrous Metals
Aluminum • Stainless Steel • Nickel Alloys
Carbon Steel • Alloy Steel • Tool Steel
Titanium • Magnesium • Moly • Tungsten
Trademarked Metals

Phone: 973-276-5000
Fax: 973-276-5050
Toll-Free: 800-600-9290
E-Mail: sales@steelforge.com
www.steelforge.com

All Metals & Forge Group, LLC, maintains our files for a minimum of five years.

These test reports apply to our sales order: 63480-8	
Customer: Texas A&M University	Customer Purchase Order: AM28-16-P009018
Date: May 12, 2017	Heat or Lot Number: 1411B056
Material: Stainless Steel / A182 F6A	Heat Treat Report: Quench & Temper
Size: Item #1; 21" od x 14" id x 18" long – (1 PC) / Item #2; 21" od x 8" id x 6" long – (2 PCS)/ Item #3; 10.50" od x 8" id x 3" long – (2 PCS)/ Item #4; 9" od x 5" id x 4.5" long – (4 PCS)	Signature: AM&FG 2 QC

AM&FG-LT162 REV 9

ALL METALS & FORGE GROUP
75 LANE RD, Fairfield NJ 07004
Phone 973-276-5000 Fax 973-276-5050
Email info@steelforge.com

HEAT TREATMENT TEST REPORT

PRODUCT NAME	DRAWING NO.	MATERIAL	Heat NO.	METHOD OF HT	HT STATUS OF TEST PIECE	HT PROCESS RECORDREMENT					
						HEATING TEMP	TIME OF HEATING TEMP	COOL METHOD AND TIME	TEMP OF OUT FURNACE	TEMP OF COOL
Forging -Open Die PO 63480-8	60755 Rev 2-APD	A182 Fm Class 4 QUANTITY 102+2+4 =8PC	1411B056	☐ Quench & Temper	☐ HEAT TREATED WITH SAME FURNACE ☐ NO TEST PIECE Quench Temper	°C 1010°C 950°C	HOURS 6.5 h 9.5 h	Oil Air	°C 1000°C 590°C	°C 2°C 5°C

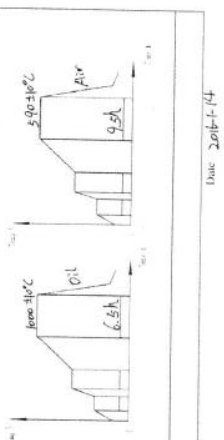

Note: HT Temperature Automatic record of time Chart

Conclusion: Acceptable ☑ Unacceptable ☐

Inspector: Reviewed By:

Date: 2016-1-14

All Metals & Forge Group

75 Lane Road
Fairfield, New Jersey 07004

Ferrous & Non-Ferrous Metals
Aluminum • Stainless Steel • Nickel Alloys
Carbon Steel • Alloy Steel • Tool Steel
Titanium • Magnesium • Moly • Tungsten
Trademarked Metals

Phone: 973-276-5000
Fax: 973-276-5050
Toll-Free: 800-600-9290
E-Mail: sales@steelforge.com
www.steelforge.com

All Metals & Forge Group, LLC, maintains our files for a minimum of five years.

These test reports apply to our sales order: 63480-8	
Customer: Texas A&M University	Customer Purchase Order: AM28-16-P009018
Date: May 12, 2017	Heat or Lot Number: 1411B056
Material: Stainless Steel / A182 F6A	Heat Treat Chart: Quench & Temper
Size: Item #1; 21" od x 14" id x 18" long – (1 PC) / Item #2; 21" od x 8" id x 6" long – (2 PCS)/ Item #3; 10.50" od x 8" id x 3" long – (2 PCS)/ Item #4; 9" od x 5" id x 4.5" long – (4 PCS)	Signature: AM&FG 2

AM&FG-LT162 REV 9

The Specifications and additional information set forth in this certificate are accurate with respect to the materials described herein as of the date set forth above, Any subsequent thermo-mechanical or similar processing (including any such processing to change the gauge, condition or specification of materials described herein) shall nullify the information set forth in this certificate and All Metals & Forge Group

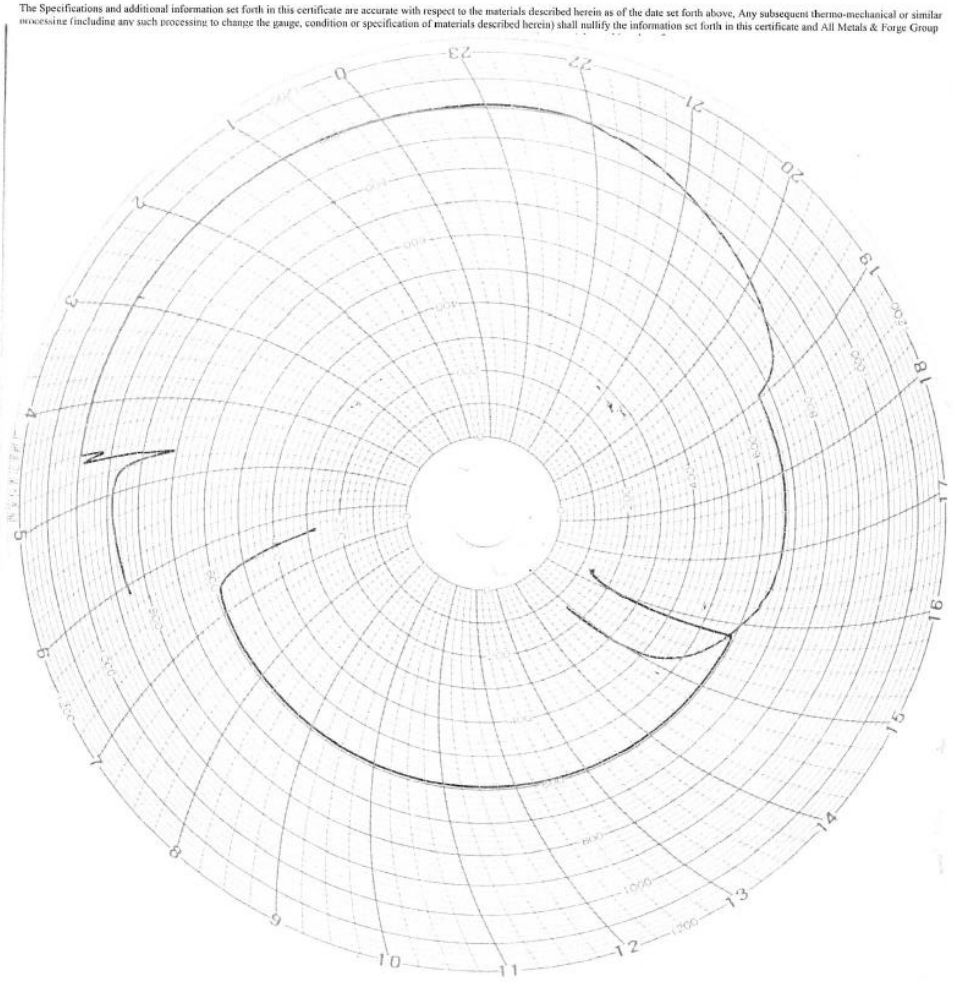

Quench & Temper

Certificate of chemical analysis and mechanical properties

All Metals & Forge Group

OPEN DIE FORGINGS & SEAMLESS ROLLED RINGS

Ferrous & Non-Ferrous Metals
Aluminum • Stainless Steel • Nickel Alloys
Carbon Steel • Alloy Steel • Tool Steel
Titanium • Magnesium • Moly • Tungsten
Trademarked Metals

Phone: 973-276-5000
Fax: 973-276-5050
Toll-Free: 800-600-9290
E-Mail: sales@steelforge.com
www.steelforge.com

75 Lane Road
Fairfield, New Jersey 07004

Date	: January 18, 2016
Customer	: Texas A&M University
Attn	: Anibal Morones
Address	: Department of Mechanical Engineering
Address	: College Station, TX 77843
AM&FG SO#	: 63480-8
Your Order No.	: AM28-16-P009018

CERTIFICATE OF CHEMICAL ANALYSIS AND PHYSICAL PROPERTIES

ITEM #	DESCRIPTION & SPECIFICATION	QUANTITY	HEAT/LOT NO.
1	Forging - Smls Rolled Rings, Stainless Steel / A182 F6A CLASS 4, ASTM A182, FORGED, Q&T TO 110 KSI MIN. YIELD, SEAMLESS, ROUGH MACHINED WITH A 250 RMS FINISH, UT TEST PER ASTM A388, ROUGH MACHINED SIZE = 21.250" OD X 13.750" ID X 18.250" LONG, 21" od x 14" id x 18" long, Part Number: 545-12	1 PC	14118056
2	Forging - Smls Rolled Rings, Stainless Steel / A182 F6A CLASS 4, ASTM A182, FORGED, Q&T TO 110 KSI MIN. YIELD, SEAMLESS, ROUGH MACHINED WITH A 250 RMS FINISH, UT TEST PER ASTM A388, ROUGH MACHINED SIZE = 21.250" OD X 7.750" ID X 6.250" LONG, 21" od x 8" id x 6" long, Part Number: 545-12	2 PCS	
3	Forging - Smls Rolled Rings, Stainless Steel / A182 F6A CLASS 4, ASTM A182, FORGED, Q&T TO 110 KSI MIN. YIELD, SEAMLESS, ROUGH MACHINED WITH A 250 RMS FINISH, UT TEST PER ASTM A388, ROUGH MACHINED SIZE = 10.75" OD X 7.750" ID X 3.250" LONG, 10.50" od x 8" id x 3" long,Part Number: 545-12	2 PCS	
4	Forging - Smls Rolled Rings, Stainless Steel / A182 F6A CLASS 4, ASTM A182, FORGED, Q&T TO 110 KSI MIN. YIELD, SEAMLESS, ROUGH MACHINED WITH A 250 RMS FINISH, UT TEST PER ASTM A388, ROUGH MACHINED SIZE = 9.25" OD X 4.750" ID X 4.75" LONG,9" od x 5" id x 4.5" long, Part Number: 545-12	4 PCS	

CHEMICAL ANALYSIS WT%

ITEM #	C %	Si %	Mn %	P %	S %	Cr %	Ni %	Mo%	Cu%
1-4	0.11	0.41	0.50	0.015	0.001	12.26	0.31	---	---

PHYSICAL PROPERTIES

ITEM #	YIELD STRENGTH (0.2%) KSI	TENSILE STRENGTH KSI	ELONGATION %	REDUCTION OF AREA %	HARDNESS BHN
1-4	128.5	146	19.5	70	296/300/296

REMARKS:

ALL TEST COUPONS USED ON THIS PO WILL BE RETAINED FOR A MAXIMUM PERIOD OF 1 YEAR FROM DATE OF DELIVERY.
VISUAL AND DIMENSIONAL INSPECTION: OK
MELTING PROCESS: EF+VODC
SPECIFICATIONS: Q&T, TENSILE ≥ 130 SKI, YIELD ≥ 110 KSI, ELONGATION; ≥ 12% REDUCTION OF AREA; ≥ 35%, HARDNESS 263-321 BHN
DELIVERY CONDITION: FORGED AND FINISH MACHINED AS PER RFQ 607537 -APD
ALL PARTS ARE 100% ULTRASONIC TESTED ACCORDING TO ASTM A388.
ULTRA SONIC TEST: TEST RESULTS ACCEPTABLE

AM&FG
2
Q.C.

Authorized Signature
(Quality Assurance Personnel)
AM&FG-ST161-JJ REV 8
Frank DiMaio, QA Manager

Window failure during hydrostatic test

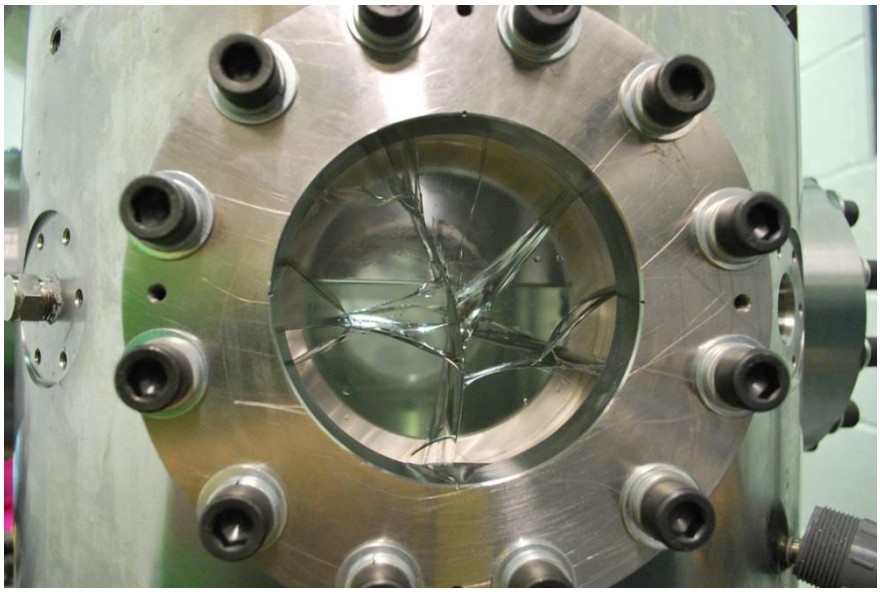

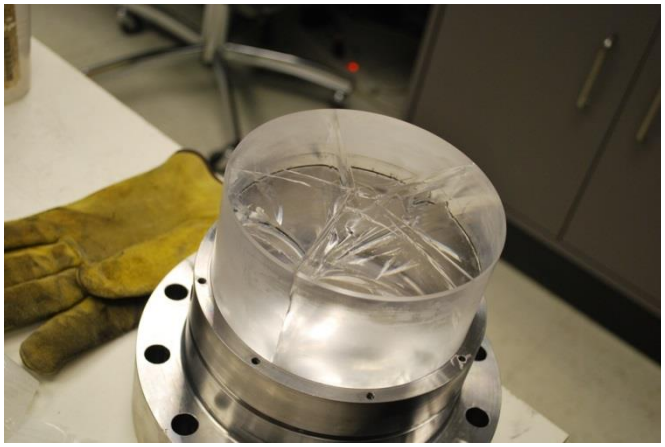

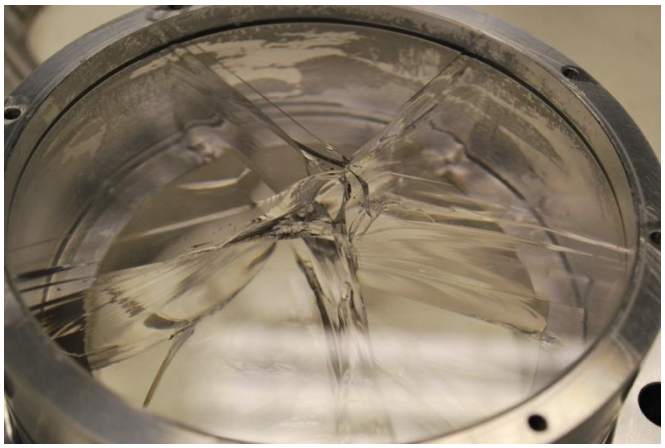

Impeller of the cylindrical bomb at University of Leeds

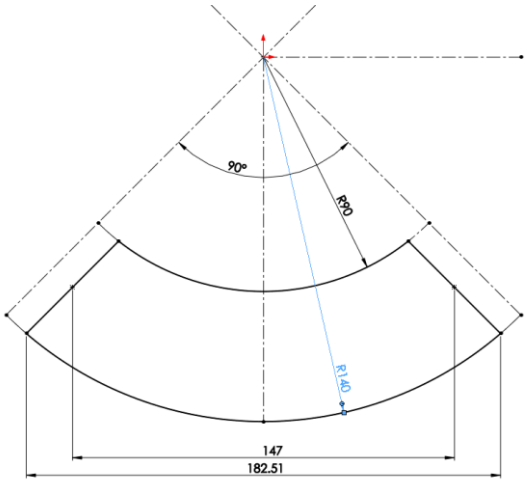

Sketch of 2D projection of impeller constructed following written description and available images [30, 31].

Quiver plots: plug impeller at 2000 rpm

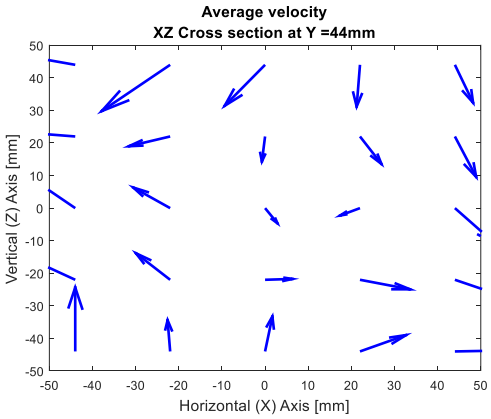

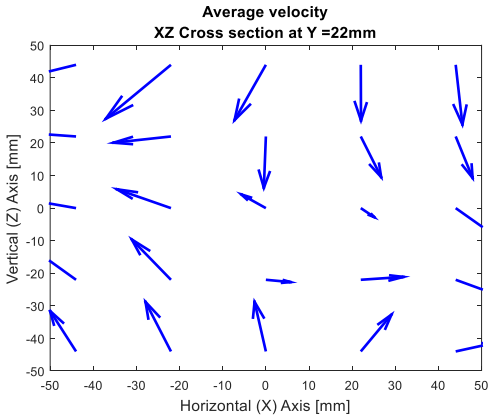

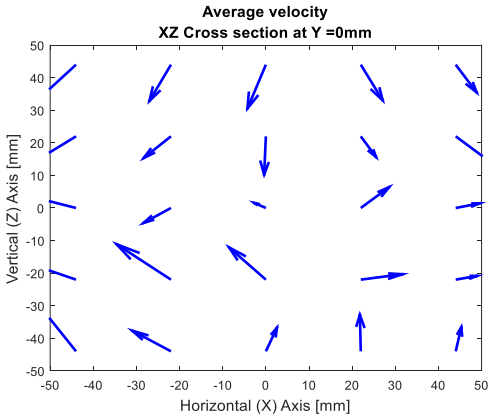

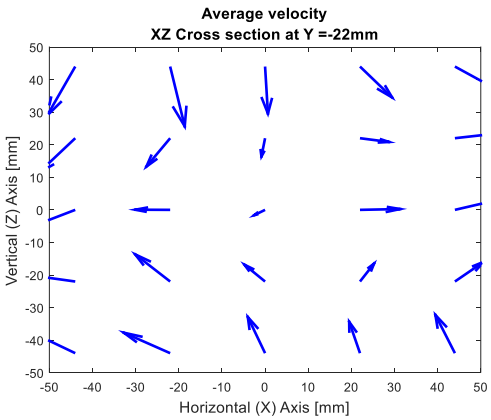

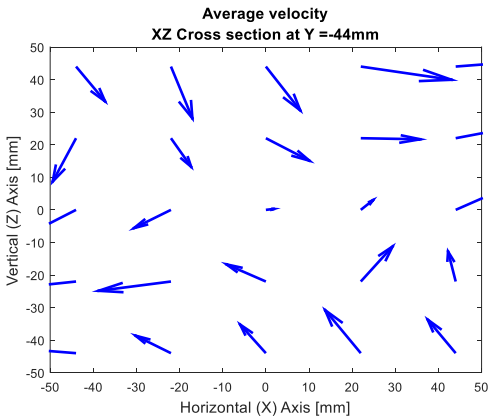

Quiver plots: plug impeller at 4000 rpm

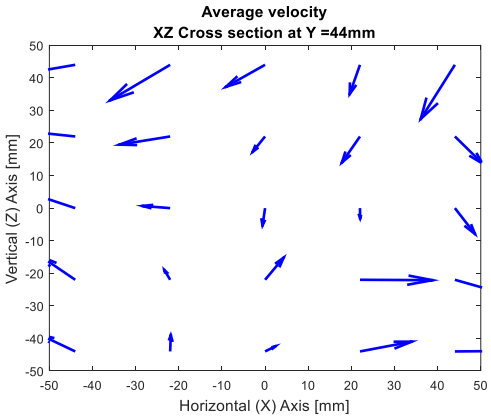

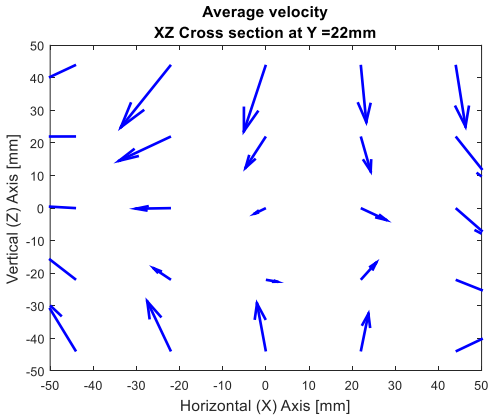

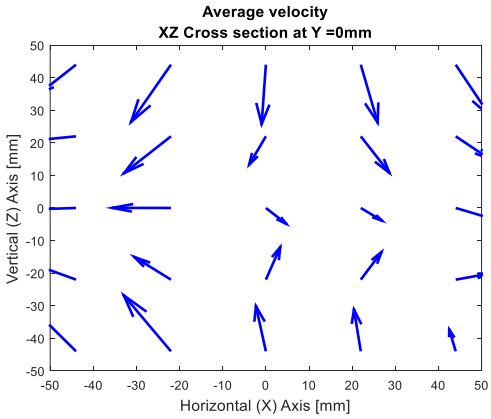

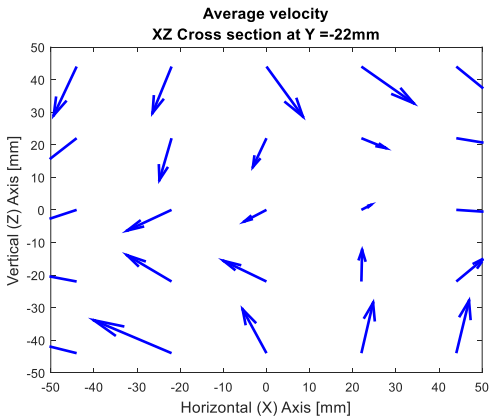

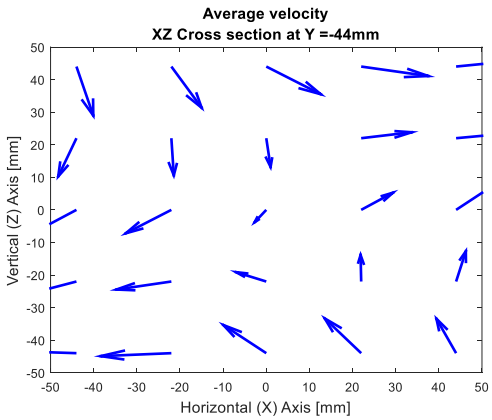

Quiver plots: plug impeller at 6000 rpm

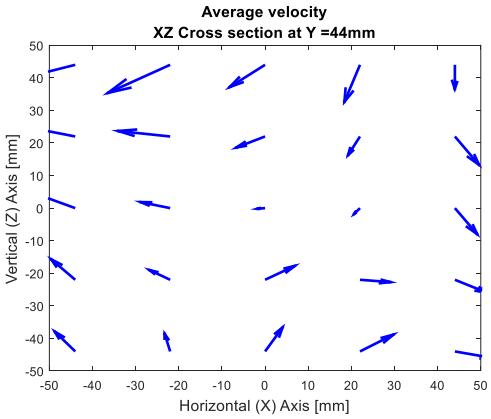

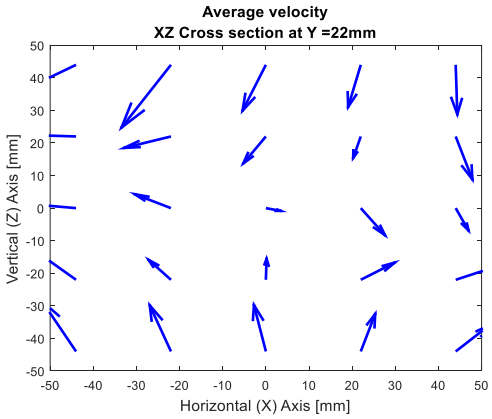

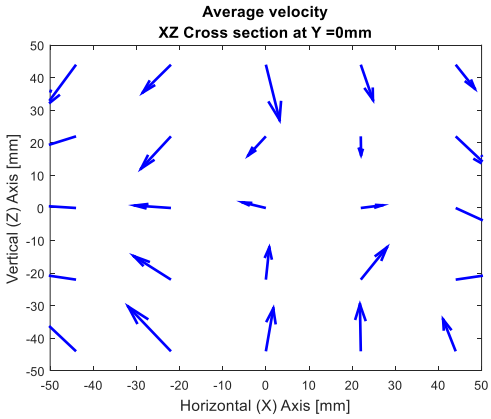

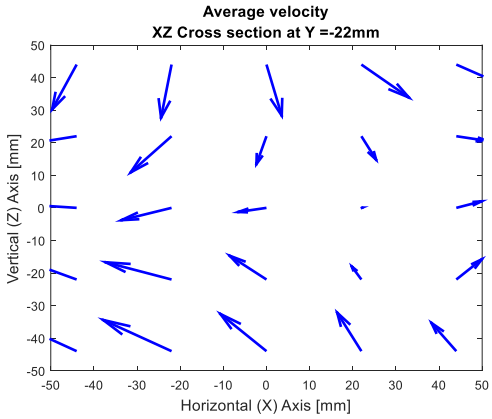

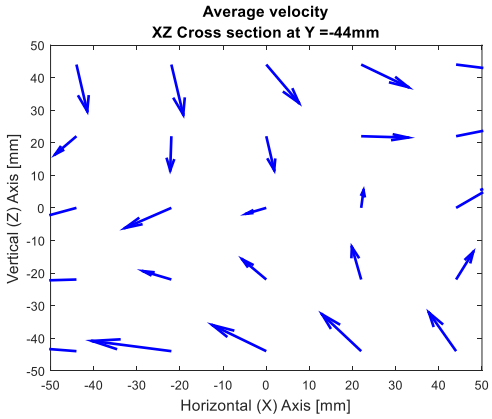

Quiver plots: leaf blower impeller at shaft tip, 2000 rpm

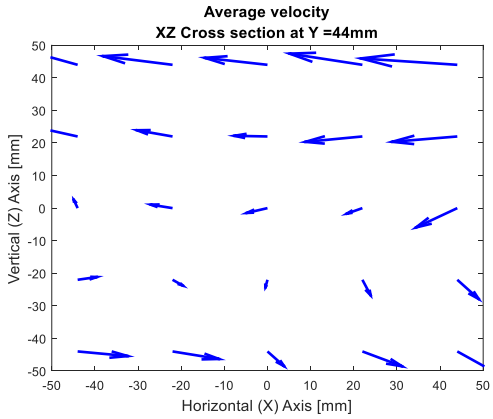

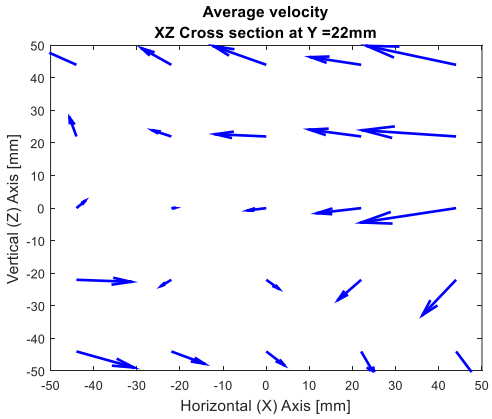

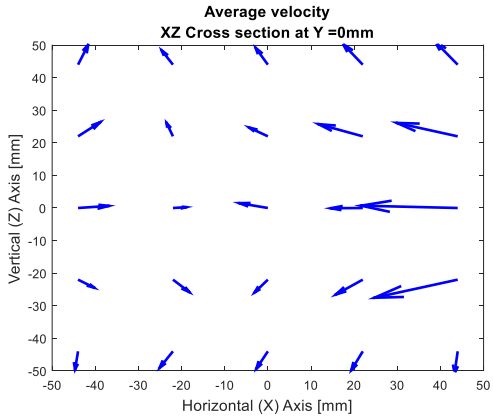

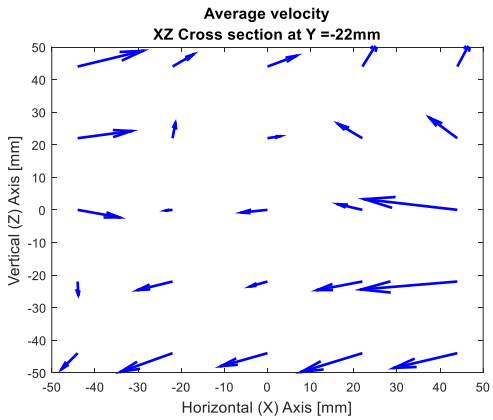

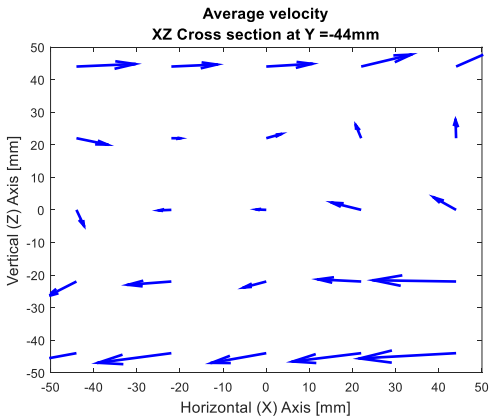

Quiver plots: leaf blower impeller at shaft tip, 4000 rpm

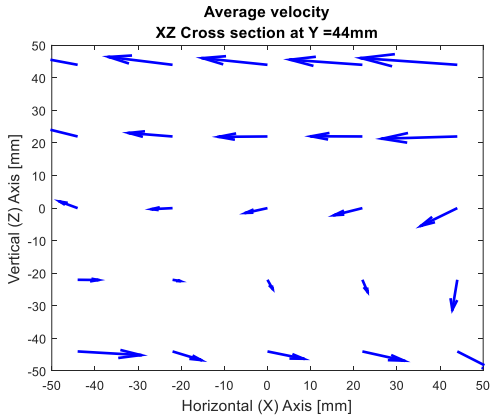

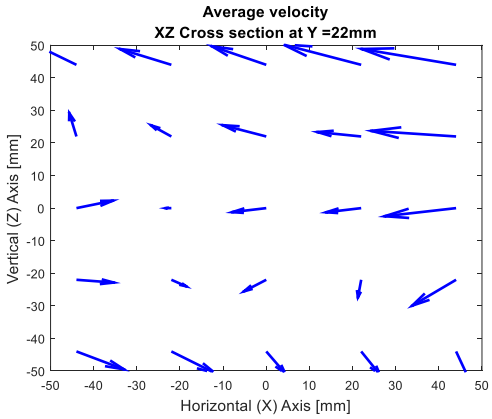

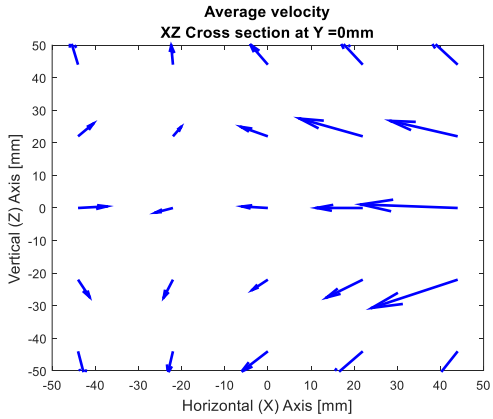

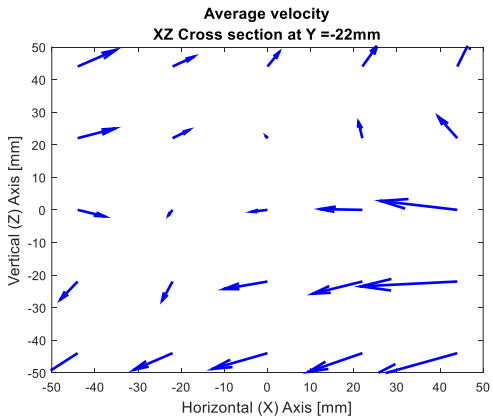

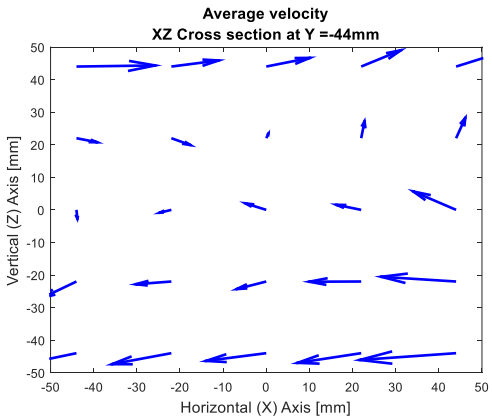

Quiver plots: leaf blower impeller at shaft tip, 6000 rpm

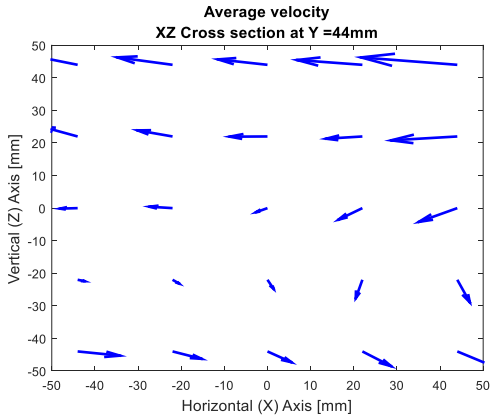

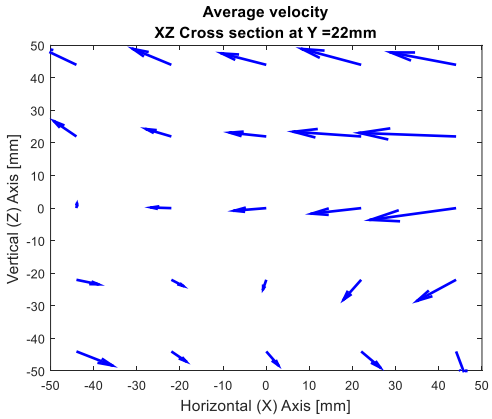

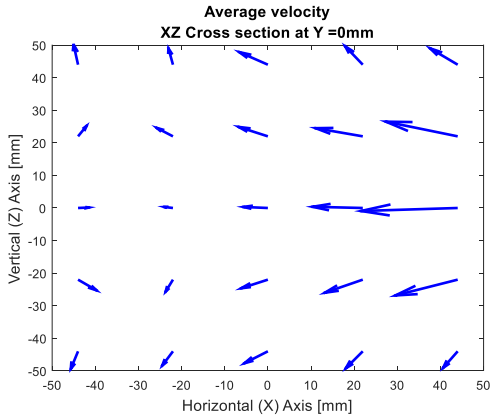

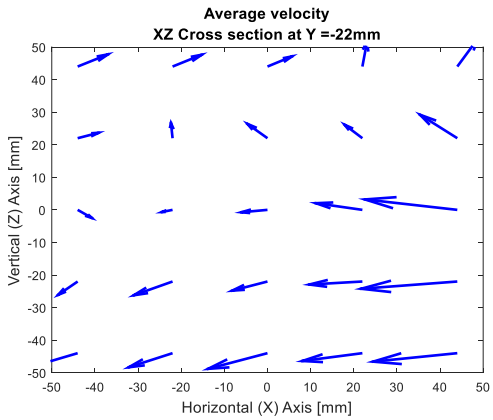

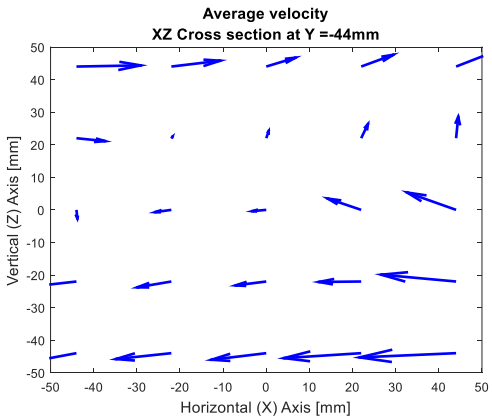

Quiver plots: leaf blower impeller at shaft tip, 8000 rpm

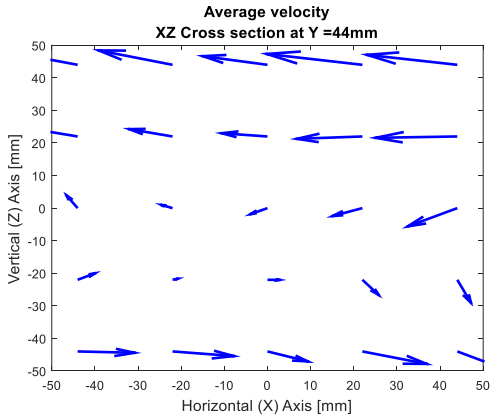

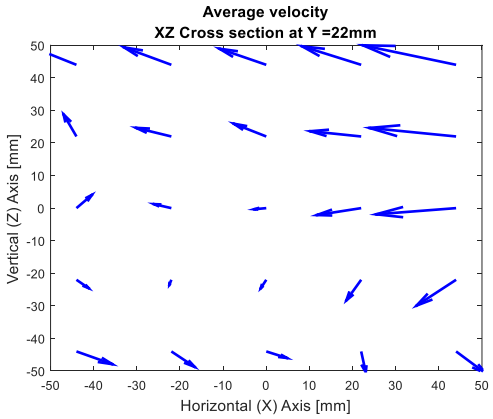

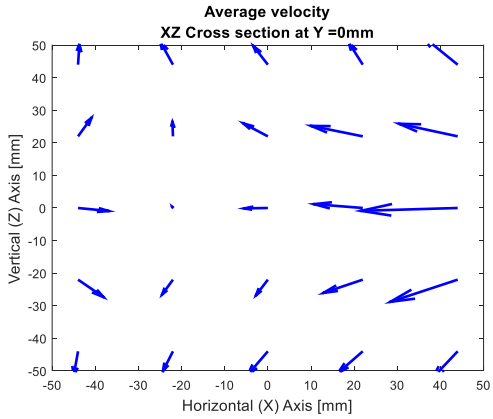

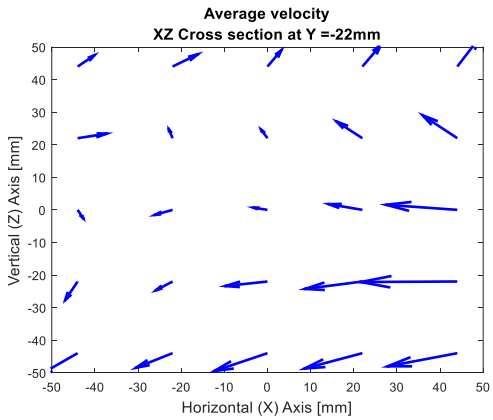

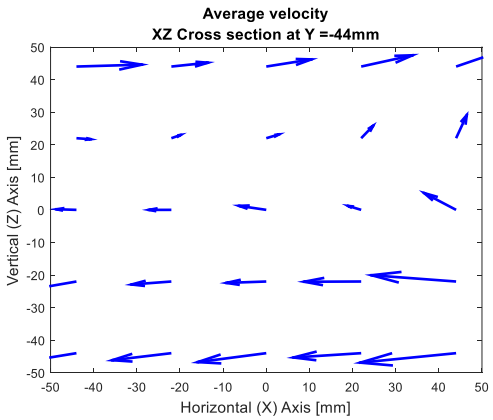

Quiver plots: leaf blower impeller close to wall, 8000 rpm

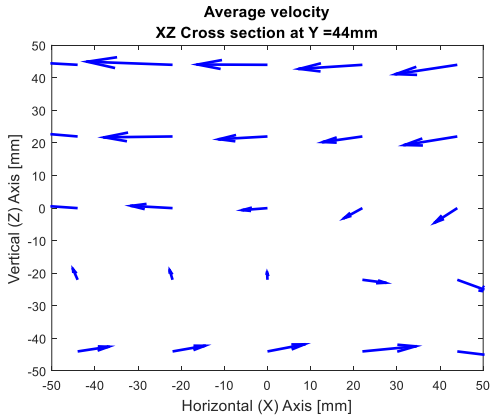

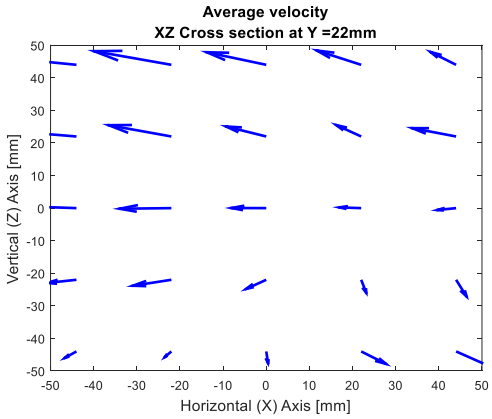

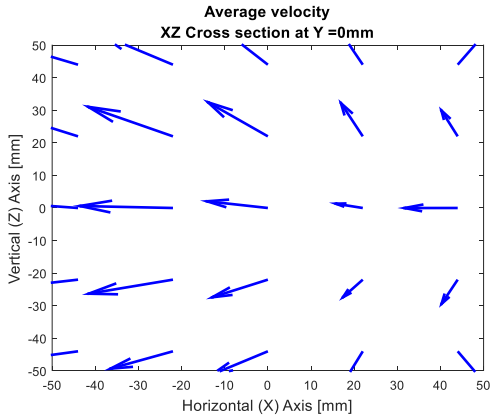

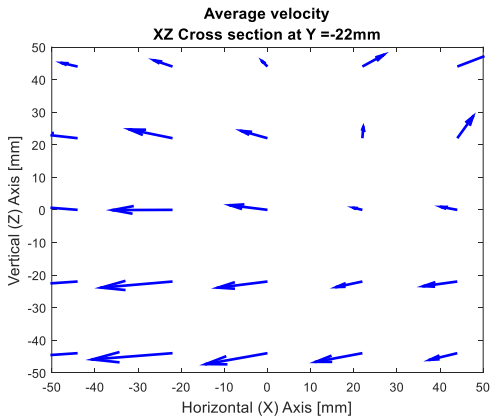

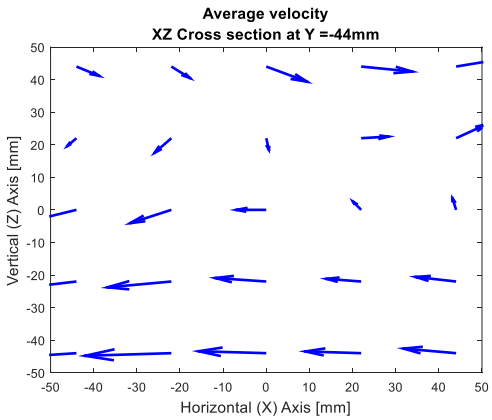

Autocorrelation code

The Fortran code below is written for parallel computation. It reads a comma-separated file that contains the instantaneous velocity time series, $\tilde{u}(\mathbf{x},t)$ and $\tilde{w}(\mathbf{x},t)$. Each row in the input data is expected to be in the following order: $\tilde{u}(\mathbf{x},t_i)$, $\tilde{w}(\mathbf{x},t_i)$, t_i. The program computes the local average velocity ($U(\mathbf{x})$ and $W(\mathbf{x})$), the turbulence fluctuation ($u'(\mathbf{x},t)$ and $w'(\mathbf{x},t)$), and then proceeds with the algorithm of autocorrelation. The program control parameters, namely the total time shift or delay to carry the autocorrelation, the number bins in which such delay will be segmented and the name of the file containing the input data is kept in separate text file called "*settings.txt"*. This allows a minimal interface to operate the program without the need of compiling every time. The program outputs the correlation function in a file that will be named identical to the raw data input file but with extension "*.out*"

LDV measurements are acquired at random time stamps. This makes very unlikely to have measurements evenly spaced in time. One way to circumvent this peculiarity is to use time intervals to compute the autocorrelations, as opposed to exact time differences. This is also known as the slotted correlation method and has been described in [43].

```
program timescalesource
    implicit none
    include 'mpif.h'
    integer :: myrank, peers, mpierr, errcode = 0, stat(MPI_STATUS_SIZE)! MPI stuff
    integer :: i = 0, k = 0, blanks = 0, starter, closer ! counters
    integer :: bins, recs=0, ioerr = 0, reset(1) = 0, last_jump, msg_int(3)
    integer :: turn = 0, no_jump(1) = 0, last_valid
    character(len=50) :: buffer
    character(len=:), allocatable :: filename
    real :: max_shift, msg_real(2), ave(2), dt, tic = 0
    real, allocatable :: raw(:,:), t(:),  u(:,:), scratch(:,:), R(:,:), auto(:,:)
    real, allocatable :: shift(:)
    integer, allocatable :: counter(:)

! MPI initialization
    call MPI_INIT(mpierr) ! Start up
    call MPI_COMM_SIZE(MPI_COMM_WORLD, peers, mpierr) ! How many peers I have?
    call MPI_COMM_RANK(MPI_COMM_WORLD, myrank, mpierr) ! Who am I?
```

```
! Rank 0 - Preliminary stuff
    if (myrank==0) then
        tic = MPI_Wtime()

        ! Read correlation settings
        open(unit=777, file="settings.txt")
            read(777,*), max_shift ! [s] Maximum time shift
            read(777,*), bins ! Integer - Total number of time slots
            read(777,*), buffer
        close(unit=777)
        filename = trim(buffer)

    ! Open data file
        open(unit=888, file=filename)

        ! Data sanitization: finding blank lines and amount of records
            find_blanks_loop: do
                read(888,*,iostat = ioerr) buffer
                if (ioerr /= 0) exit find_blanks_loop ! end of file reached
                if ( len_trim(buffer) == 0) blanks = blanks + 1
                recs = recs + 1
            end do find_blanks_loop
            ! this has the gross total number of lines in file

            rewind(888); ioerr = 0 !rewinding file and clearing end-of-file flag
            recs = recs - blanks
            dt = max_shift / bins
            allocate( raw(recs,3), t(recs) )

        !Reading data loop (undetermined)
            reading_data_loop: do
                i = i + 1
                if (i > recs) exit reading_data_loop
                read(888,*,iostat = ioerr) raw(i,1), raw(i,2), raw(i,3)
                if (ioerr /= 0) exit reading_data_loop !end of file found
            end do reading_data_loop

        close(unit=888)

    ! Time stamp reset detection
        last_valid = recs ! this stays in case no time reset found
        t = raw(:,3) ! temporarly holds time stamp
        t = t - t(1) ! makes first entry the starting point (t = 0[s])
        reset = minloc (t, MASK = t < 0) ! looks for negative time stamps
        if(reset(1) /= 0 ) last_valid = reset(1)-1

    ! Sets let last record to be used in "unshifted" series
        no_jump = minloc (t, MASK = t > t(last_valid) - max_shift )
        last_jump = no_jump(1)-1

    ! Information package preparation
        allocate( scratch(last_valid,3) )
        ave = [ sum(raw(1:last_valid,1))/last_valid, sum(raw(1:last_valid,2))/last_valid ]
        scratch(:,1) = raw(1:last_valid,1) - ave(1)
        scratch(:,2) = raw(1:last_valid,2) - ave(2)
        scratch(:,3) = t(1:last_valid)
        deallocate(t) ! if time stamp reset found, this vector needs to be redefined

    ! Printing analysis setup
        print*,
        print*,
        print*, 'Analyzing file: ', filename
        print*, 'Total lines in file: ', recs, '    blank lines ', blanks
        print*,
        print*,
        print*, 'Autocorrelation settings:'
        print*, '   - Total number of time slots: ', bins
        print*, '   - Maximum shift in analysis  (longest lag): ', max_shift, '  [sec]'
        print*, '   - First time stamp: ', raw(1,3), '  [sec]'
        print*, '   - Last valid time stamp: ', raw(last_valid, 3), '  [sec]'
        print*, '   - Number of records in file: ', recs
        print*, '   - Number of valid records: ', last_valid
        print*, '   - Average of column 1: ', ave(1)
        print*, '   - Average of column 2: ', ave(2)
        if(reset(1) /= 0 ) print*, '    - Number of points after time stamp reset: ', recs - reset, '
[sec]'
```

```
    ! Checking setup
        if (raw(last_valid,3) < max_shift) then ! You cannot shift beyond the last record time
            print*, 'It is not possible to construct the autocorrelation'
            print*, 'The maximum time shift has to be shorter'
            print*, 'Last valid time stamp ', raw(last_valid,3), '  [sec]'
            print*, 'Requested maximum time shift of autocorrelation ', max_shift, ' [sec]'
            errcode = 1
            call MPI_Abort(MPI_COMM_WORLD, errcode, mpierr) ! Game over!

        else if (bins<peers) then
            print*, 'The number of bins has to be greater than the number of processes'
            print*, 'The maximum time shift has to be shorter'
            print*, '   - Number of process: ', peers
            print*, '   - Number of bins: ', bins
            errcode = 2
            call MPI_Abort(MPI_COMM_WORLD, errcode, mpierr) ! Game over!
        end if

    ! Broadcast basic problem setup variable to other processes
        msg_int(1) = bins; msg_int(2) = last_jump; msg_int(3) = last_valid
        msg_real(1) = max_shift; msg_real(2) = dt
        call MPI_Bcast(msg_int,3,MPI_INT,0,MPI_COMM_WORLD,mpierr)
        call MPI_Bcast(msg_real,2,MPI_REAL,0,MPI_COMM_WORLD,mpierr)
        call MPI_Bcast(scratch(1,1),size(scratch), MPI_REAL,0,MPI_COMM_WORLD,mpierr)

! Everyone else receives data
    else
        call MPI_Bcast(msg_int,3,MPI_INT,0,MPI_COMM_WORLD,mpierr)
        call MPI_Bcast(msg_real,2,MPI_REAL,0,MPI_COMM_WORLD,mpierr)
        bins = msg_int(1); last_jump = msg_int(2); last_valid = msg_int(3)
        max_shift = msg_real(1); dt = msg_real(2)
        allocate(scratch(last_valid,3))
        call MPI_Bcast(scratch(1,1),size(scratch),MPI_REAL,0,MPI_COMM_WORLD,mpierr)
    end if
! End of preliminary stuff
! By this point, everyone has a copy of the time series.


    allocate( t(last_valid), u(last_valid,2), R(bins,2), counter(last_valid), shift(bins) )
    u = scratch(:,1:2) ! Velocity
    t = scratch(:,3) ! Time stamp

    R = 0 ! Autocorrelation vector initializaded

    shift = dt * [(i, i = 0, bins - 1 )] ! Time shift vector

! Autocorrelation calculation
! Sweep time shift bins
    do k = 1, bins

    ! Time shift bins distributed in round robin among processes
        if (turn == myrank) then
        starter = 1
        closer = 1
        counter = 0
        ! Points sweep loop:
            points_loop: do i = 1, last_jump

            ! Scrolls point by point until finds the first in bracket (inclusive)
                starter_loop: do
                    if ( t(starter) < t(i) + shift(k) ) then
                        starter = starter + 1
                        cycle starter_loop
                    else if (t(starter) <= t(i) + shift(k) + dt) then ! starter in interval found
                        exit starter_loop
                    else
                        ! no points in time shift interval for this point
                        ! skip to next point
                        cycle points_loop
                    end if
                end do starter_loop
                !if(myrank == 1)print*, 'starter found: ', starter, 'bin: ', k, 'shift: ', shift(k)
            ! Scrolls point by point until finds the last in bracket
            ! At this point it is known that there is at least one point in bracket
                closer_loop: do
                    if (t(closer) < t(i) + shift(k) + dt ) then
```

```
                        closer = closer + 1
                        cycle closer_loop
                    else
                        closer = closer - 1
                        exit closer_loop
                    end if
                end do closer_loop

                counter(i) = closer - starter + 1 !
                R(k,:) = R(k,:) + u(i,:) * sum( u(starter:closer,:), 1 )

            end do points_loop

            R(k,:) = R(k,:) / sum( counter ) ! Gets the average product

        end if
    ! Process round robin control
        turn = turn + 1 ! Scrolls turn
        if (turn/peers == 1) turn = 0 ! Reset turn control to start over

    end do


! Up to this point, the autocorrelation elements are available, but scattered
    turn = 0
    do i = 1, bins

    ! Everybody sends their respective info
        if (myrank == turn) then
            call MPI_SEND( R(i,1), 1, MPI_REAL, 0, i, MPI_COMM_WORLD, mpierr )
            call MPI_SEND( R(i,2), 1, MPI_REAL, 0, i+bins, MPI_COMM_WORLD, mpierr )
        end if

    ! Root process collects
        if (myrank == 0) then
            call MPI_RECV( R(i,1), 1, MPI_REAL, turn, i, MPI_COMM_WORLD, stat, mpierr )
            call MPI_RECV( R(i,2), 1, MPI_REAL, turn, i+bins, MPI_COMM_WORLD, stat, mpierr )
        end if

    ! Process round robin control
        turn = turn + 1 ! Scrolls turn
        if (turn/peers == 1) turn = 0 ! Reset turn control to start over
    end do

! Output
    if (myrank == 0) then

        print*,
        print*, 'Done. Saving to file...'

        k = len(filename)
        open(unit=333, file=filename(1:k-4)//'.out' )
        !open(unit=333, file="r.out" )
        allocate(auto(bins,2))
        auto(:,1) = R(:,1)/R(1,1)
        auto(:,2) = R(:,2)/R(1,2)
        do i = 1, bins
            write(333,*) i, shift(i), auto(i,:)
        end do

        close(unit=333)

        print*, 'Saved.'
        print*,
        print*,
        print*, 'Adios!'
        print*,
        print*,
        print*, 'Total elapsed time: ', MPI_Wtime() - tic, ' [sec]'
        print*,
    end if

    call MPI_FINALIZE(mpierr) ! Apaga y vamonos!
end program
```

Autocorrelations and integral time scale of selected points

The autocorrelation plots shown here have been smoothed with a Savitsky-Golay method using a 2nd order polynomial and 32 points per window. Coordinates in mm.

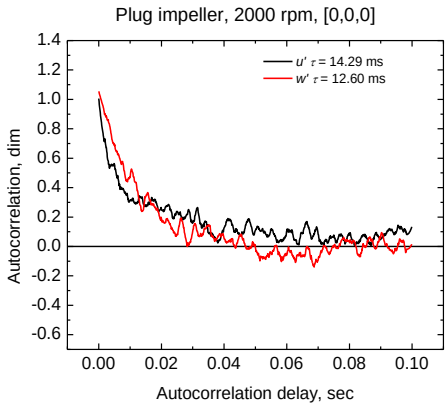

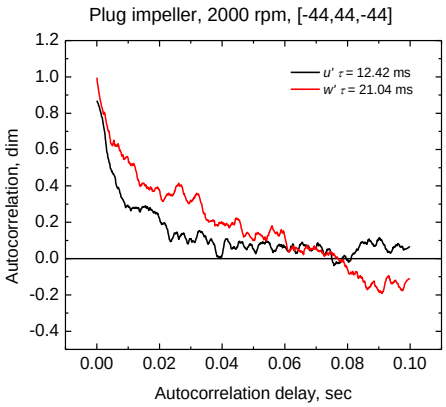

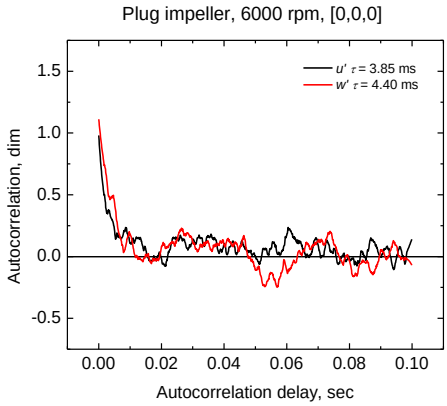

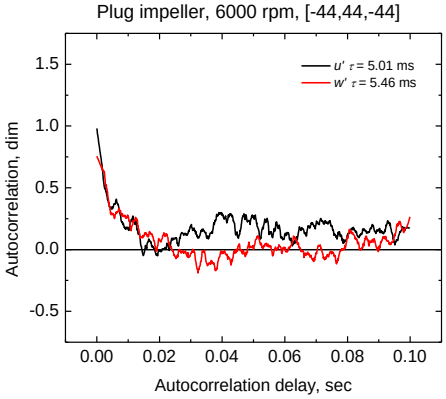

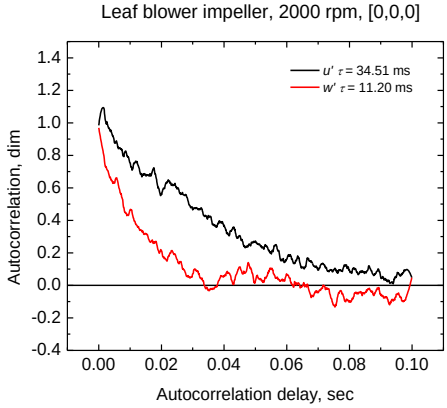

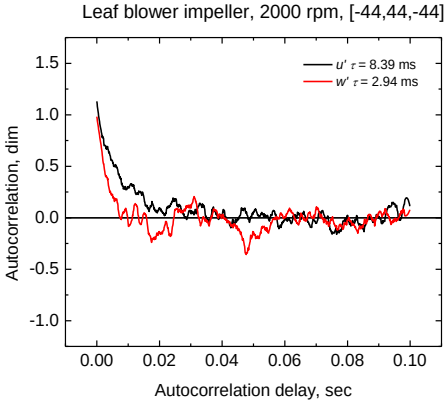

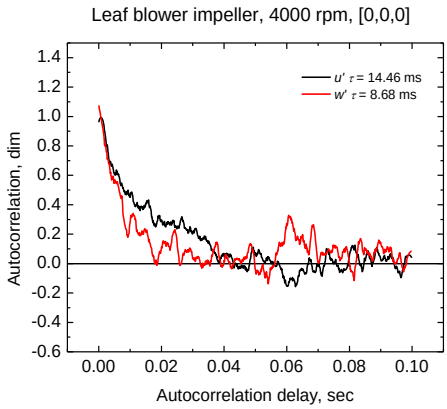
Leaf blower impeller, 4000 rpm, [0,0,0]
u' τ = 14.46 ms
w' τ = 8.68 ms
Autocorrelation, dim
Autocorrelation delay, sec

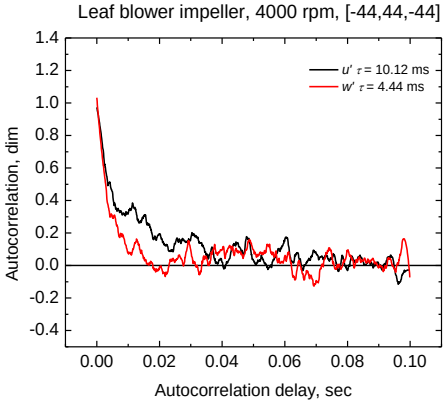
Leaf blower impeller, 4000 rpm, [-44,44,-44]
u' τ = 10.12 ms
w' τ = 4.44 ms
Autocorrelation, dim
Autocorrelation delay, sec

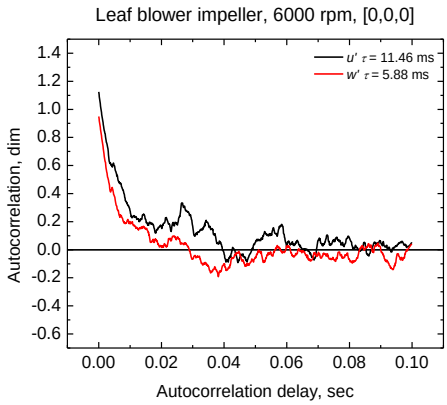
Leaf blower impeller, 6000 rpm, [0,0,0]
u' τ = 11.46 ms
w' τ = 5.88 ms
Autocorrelation, dim
Autocorrelation delay, sec

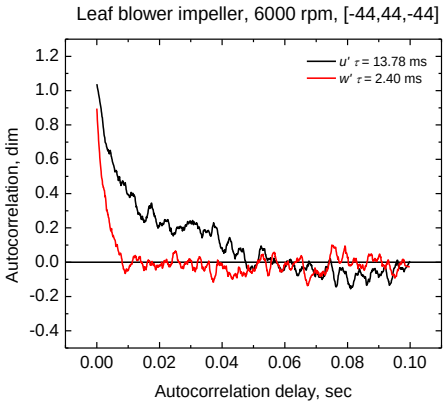
Leaf blower impeller, 6000 rpm, [-44,44,-44]
u' τ = 13.78 ms
w' τ = 2.40 ms
Autocorrelation, dim
Autocorrelation delay, sec

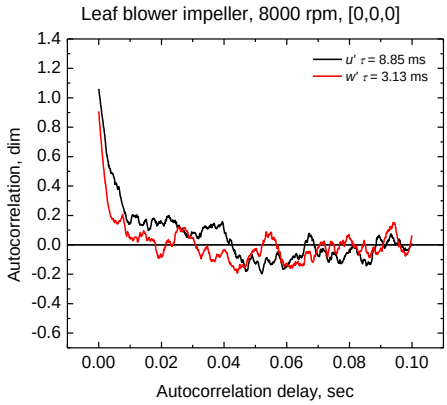
Leaf blower impeller, 8000 rpm, [0,0,0]
u' τ = 8.85 ms
w' τ = 3.13 ms
Autocorrelation, dim
Autocorrelation delay, sec

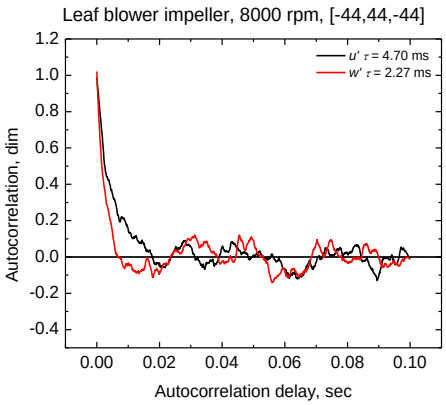
Leaf blower impeller, 8000 rpm, [-44,44,-44]
u' τ = 4.70 ms
w' τ = 2.27 ms
Autocorrelation, dim
Autocorrelation delay, sec

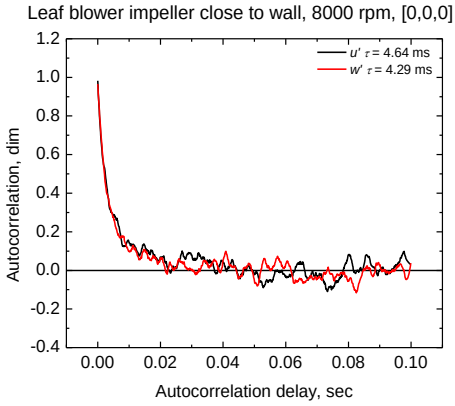
Leaf blower impeller close to wall, 8000 rpm, [0,0,0]
u′ τ = 4.64 ms
w′ τ = 4.29 ms
Autocorrelation, dim
Autocorrelation delay, sec
1.2
1.0
0.8
0.6
0.4
0.2
0.0
-0.2
-0.4
0.00
0.02
0.04
0.06
0.08
0.10

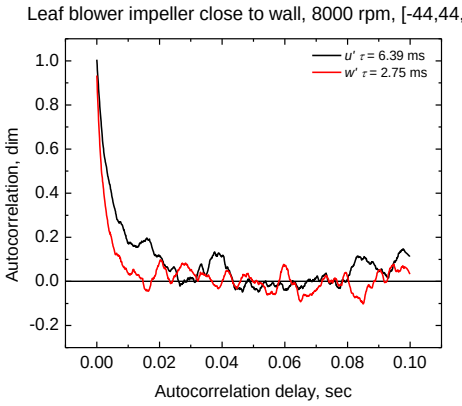
Leaf blower impeller close to wall, 8000 rpm, [-44,44,-44]
u′ τ = 6.39 ms
w′ τ = 2.75 ms
Autocorrelation, dim
Autocorrelation delay, sec
1.0
0.8
0.6
0.4
0.2
0.0
-0.2
0.00
0.02
0.04
0.06
0.08
0.10

Engineering drawings

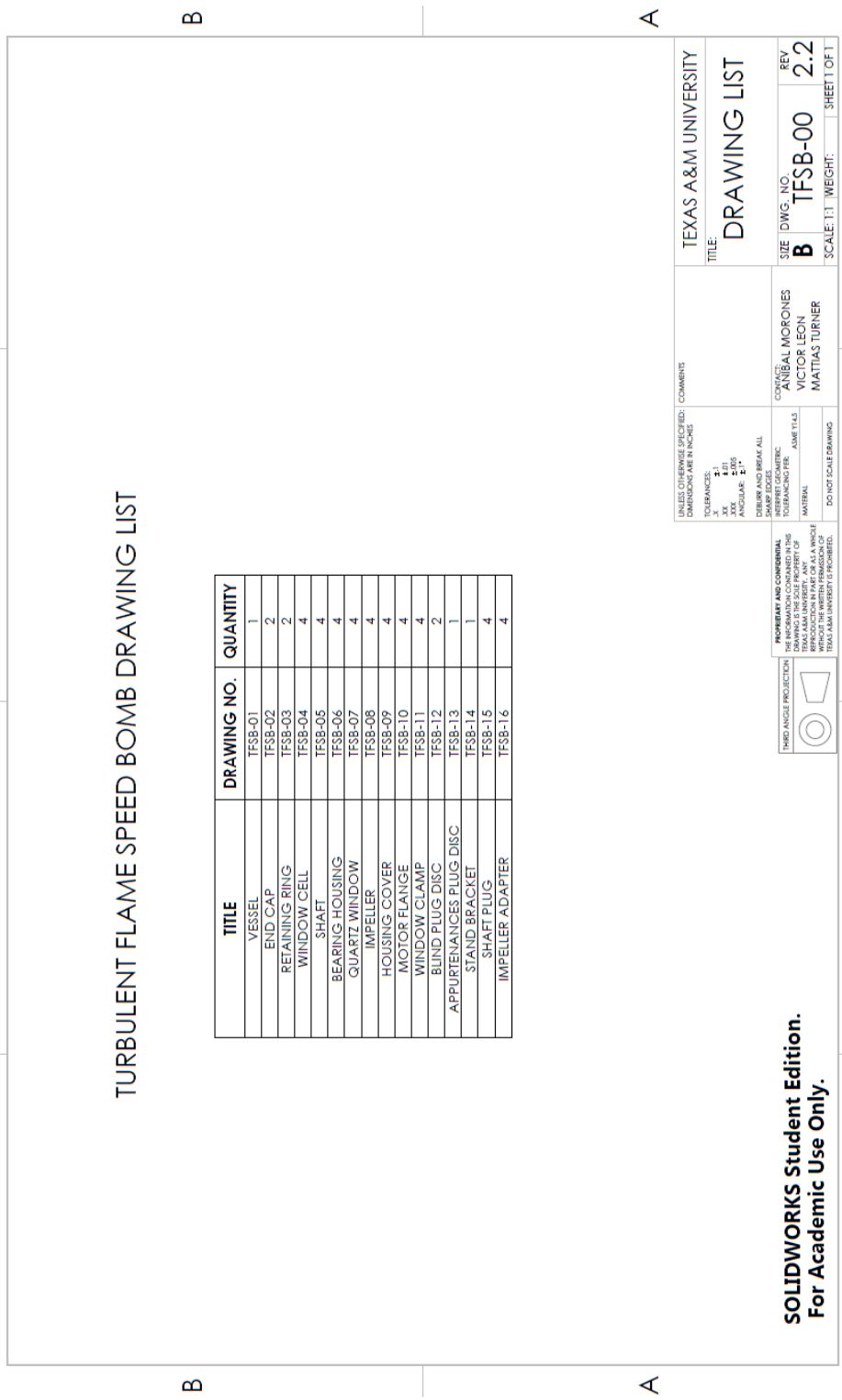

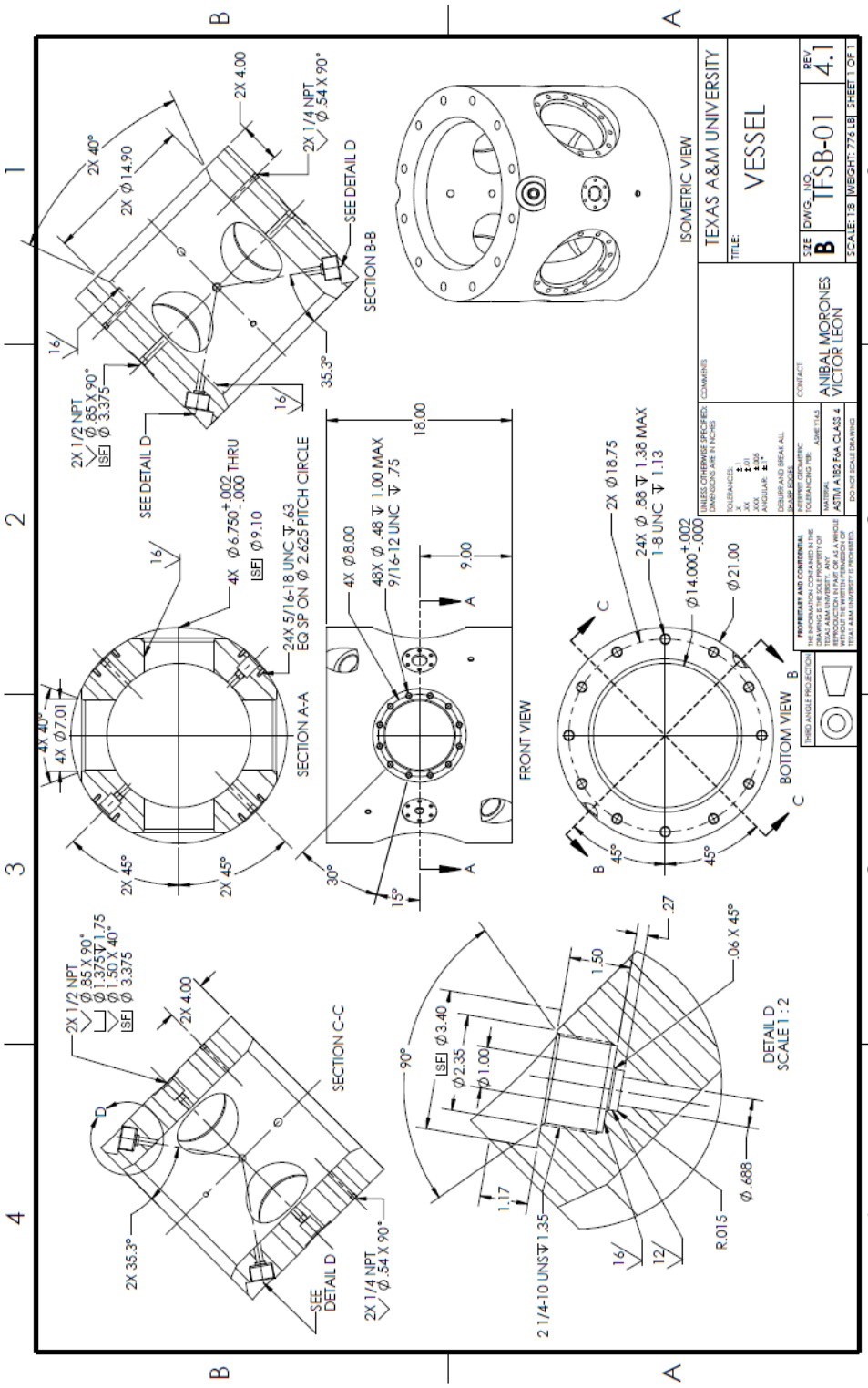
TEXAS A&M UNIVERSITY
VESSEL
DWG. NO. TFSB-01
REV 4.1
SIZE B
SCALE: 1:8 WEIGHT: 778 LB SHEET 1 OF 1
ANIBAL MORONES
VICTOR LEON
ASME Y14.5
ASTM A182 F6A CLASS 4
ISOMETRIC VIEW
FRONT VIEW
BOTTOM VIEW
SECTION A-A
SECTION B-B
SECTION C-C
DETAIL D
SCALE 1 : 2
SEE DETAIL D
2X 1/2 NPT
2X 1/4 NPT
24X 5/16-18 UNC ∓ .63
EQ SP ON Ø 2.625 PITCH CIRCLE
48X Ø .48 ∓ 1.00 MAX
9/16-12 UNC ∓ .75
24X Ø .88 ∓ 1.38 MAX
1-8 UNC ∓ 1.13
2 1/4-10 UNS∓ 1.35
R.015
.06 X 45°

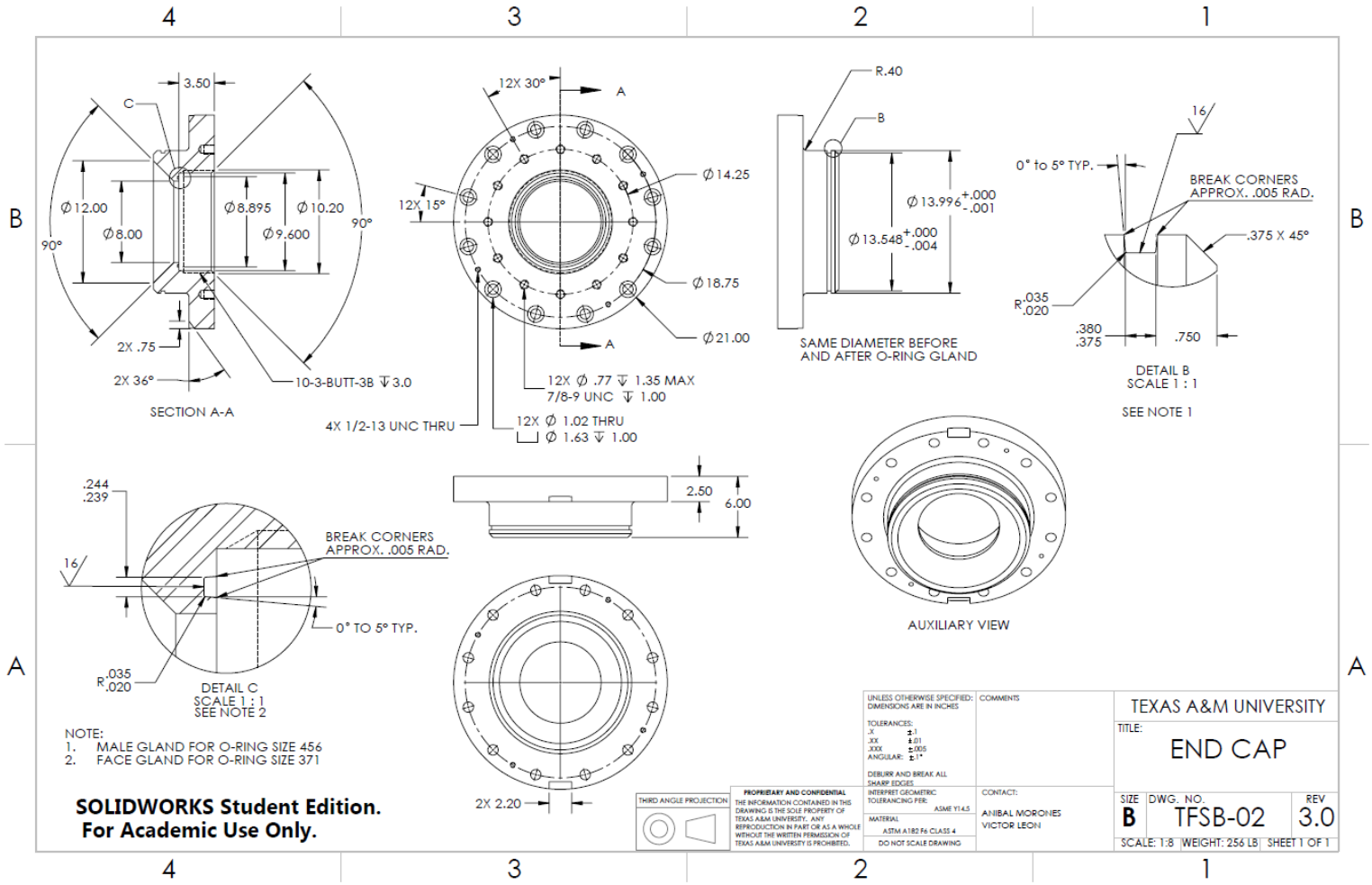
4
3
2
1
B
A
3.50
C
Ø12.00
Ø8.00
Ø8.895
Ø9.600
Ø10.20
90°
90°
2X .75
2X 36°
10-3-BUTT-3B ↧3.0
SECTION A-A
12X 30°
A
Ø14.25
12X 15°
Ø18.75
Ø21.00
A
4X 1/2-13 UNC THRU
12X Ø .77 ↧ 1.35 MAX
7/8-9 UNC ↧ 1.00
12X Ø 1.02 THRU
⌴ Ø 1.63 ↧ 1.00
R.40
B
Ø13.996 +.000 -.001
Ø13.548 +.000 -.004
SAME DIAMETER BEFORE
AND AFTER O-RING GLAND
16
0° to 5° TYP.
BREAK CORNERS
APPROX. .005 RAD.
.375 X 45°
R .035 .020
.380 .375
.750
DETAIL B
SCALE 1 : 1
SEE NOTE 1
2.50
6.00
.244 .239
16
BREAK CORNERS
APPROX. .005 RAD.
0° TO 5° TYP.
R .035 .020
DETAIL C
SCALE 1 : 1
SEE NOTE 2
2X 2.20
AUXILIARY VIEW
NOTE:
1. MALE GLAND FOR O-RING SIZE 456
2. FACE GLAND FOR O-RING SIZE 371
SOLIDWORKS Student Edition.
For Academic Use Only.
THIRD ANGLE PROJECTION
PROPRIETARY AND CONFIDENTIAL
THE INFORMATION CONTAINED IN THIS DRAWING IS THE SOLE PROPERTY OF TEXAS A&M UNIVERSITY. ANY REPRODUCTION IN PART OR AS A WHOLE WITHOUT THE WRITTEN PERMISSION OF TEXAS A&M UNIVERSITY IS PROHIBITED.
UNLESS OTHERWISE SPECIFIED: DIMENSIONS ARE IN INCHES
TOLERANCES:
.X ±.1
.XX ±.01
.XXX ±.005
ANGULAR: ±1°
DEBURR AND BREAK ALL SHARP EDGES
INTERPRET GEOMETRIC TOLERANCING PER: ASME Y14.5
MATERIAL: ASTM A182 F6 CLASS 4
DO NOT SCALE DRAWING
COMMENTS
CONTACT:
ANIBAL MORONES
VICTOR LEON
TEXAS A&M UNIVERSITY
TITLE:
END CAP
SIZE B
DWG. NO. TFSB-02
REV 3.0
SCALE: 1:8
WEIGHT: 256 LB
SHEET 1 OF 1

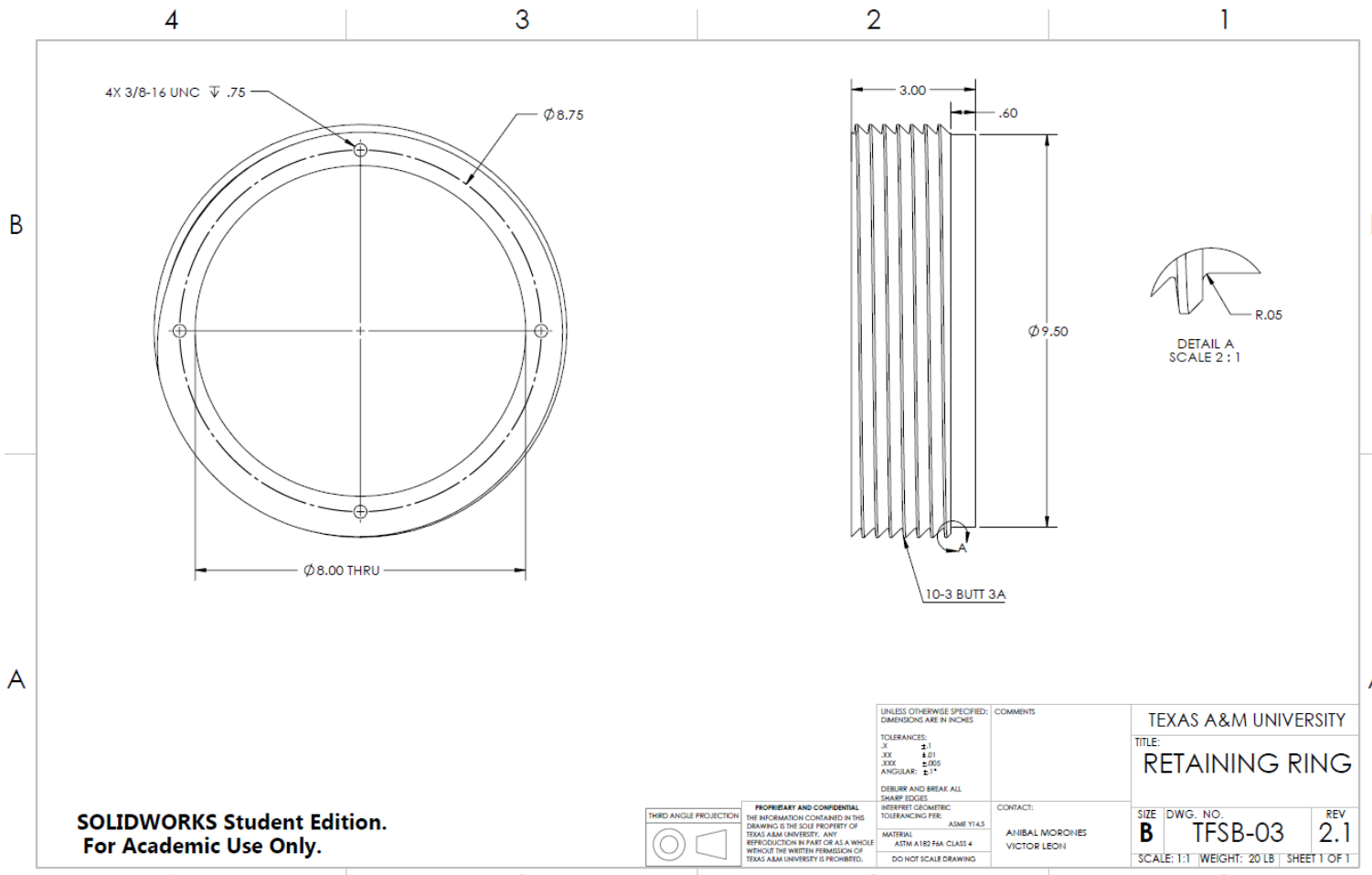

SOLIDWORKS Student Edition.
For Academic Use Only.

UNLESS OTHERWISE SPECIFIED: DIMENSIONS ARE IN INCHES
TOLERANCES:
.X ±.1
.XX ±.01
.XXX ±.005
ANGULAR: ±1°
DEBURR AND BREAK ALL SHARP EDGES
INTERPRET GEOMETRIC TOLERANCING PER: ASME Y14.5
MATERIAL: ASTM A182 F6A CLASS 4
DO NOT SCALE DRAWING

COMMENTS

CONTACT:
ANIBAL MORONES
VICTOR LEON

THIRD ANGLE PROJECTION

PROPRIETARY AND CONFIDENTIAL
THE INFORMATION CONTAINED IN THIS DRAWING IS THE SOLE PROPERTY OF TEXAS A&M UNIVERSITY. ANY REPRODUCTION IN PART OR AS A WHOLE WITHOUT THE WRITTEN PERMISSION OF TEXAS A&M UNIVERSITY IS PROHIBITED.

TEXAS A&M UNIVERSITY

TITLE:
RETAINING RING

SIZE	DWG. NO.	REV
B	TFSB-03	2.1

SCALE: 1:1 | WEIGHT: 20 LB | SHEET 1 OF 1

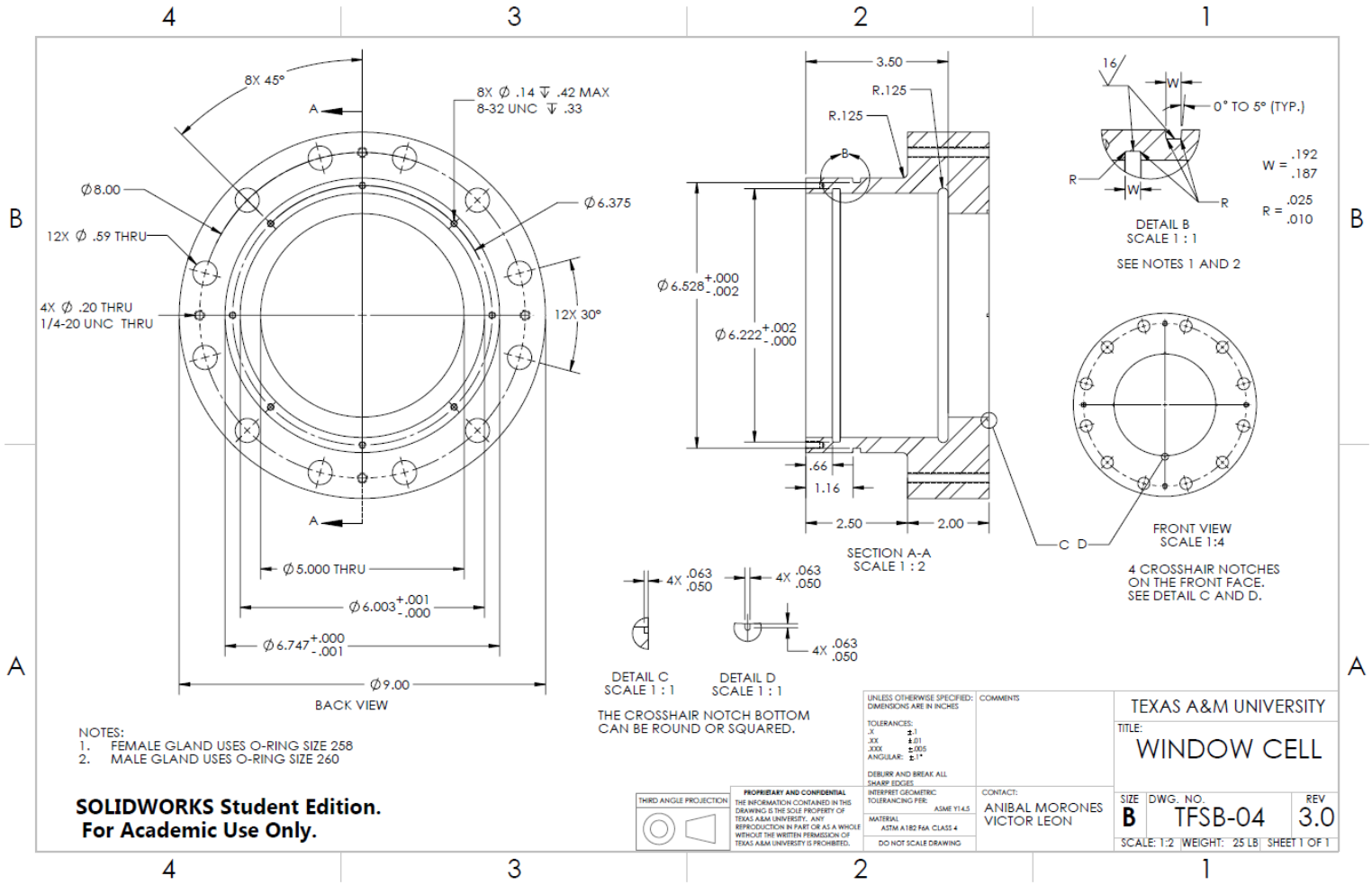
8X 45°
A
8X Ø .14 ↧ .42 MAX
8-32 UNC ↧ .33
Ø8.00
12X Ø .59 THRU
Ø6.375
4X Ø .20 THRU
1/4-20 UNC THRU
12X 30°
Ø5.000 THRU
Ø6.003 +.001 -.000
Ø6.747 +.000 -.001
Ø9.00
BACK VIEW
3.50
R.125
R.125
B
Ø6.528 +.000 -.002
Ø6.222 +.002 -.000
.66
1.16
2.50
2.00
SECTION A-A
SCALE 1 : 2
16
W
0° TO 5° (TYP.)
R
W
R
W = .192 .187
R = .025 .010
DETAIL B
SCALE 1 : 1
SEE NOTES 1 AND 2
C D
FRONT VIEW
SCALE 1:4
4 CROSSHAIR NOTCHES
ON THE FRONT FACE.
SEE DETAIL C AND D.
4X .063 .050
4X .063 .050
4X .063 .050
DETAIL C
SCALE 1 : 1
DETAIL D
SCALE 1 : 1
THE CROSSHAIR NOTCH BOTTOM
CAN BE ROUND OR SQUARED.
NOTES:
1. FEMALE GLAND USES O-RING SIZE 258
2. MALE GLAND USES O-RING SIZE 260
SOLIDWORKS Student Edition.
For Academic Use Only.
UNLESS OTHERWISE SPECIFIED: DIMENSIONS ARE IN INCHES
TOLERANCES:
.X ±.1
.XX ±.01
.XXX ±.005
ANGULAR: ±1°
DEBURR AND BREAK ALL SHARP EDGES
INTERPRET GEOMETRIC TOLERANCING PER: ASME Y14.5
MATERIAL: ASTM A182 F6A CLASS 4
DO NOT SCALE DRAWING
COMMENTS
CONTACT:
ANIBAL MORONES
VICTOR LEON
THIRD ANGLE PROJECTION
PROPRIETARY AND CONFIDENTIAL
THE INFORMATION CONTAINED IN THIS DRAWING IS THE SOLE PROPERTY OF TEXAS A&M UNIVERSITY. ANY REPRODUCTION IN PART OR AS A WHOLE WITHOUT THE WRITTEN PERMISSION OF TEXAS A&M UNIVERSITY IS PROHIBITED.
TEXAS A&M UNIVERSITY
TITLE:
WINDOW CELL
SIZE B
DWG. NO. TFSB-04
REV 3.0
SCALE: 1:2 WEIGHT: 25 LB SHEET 1 OF 1

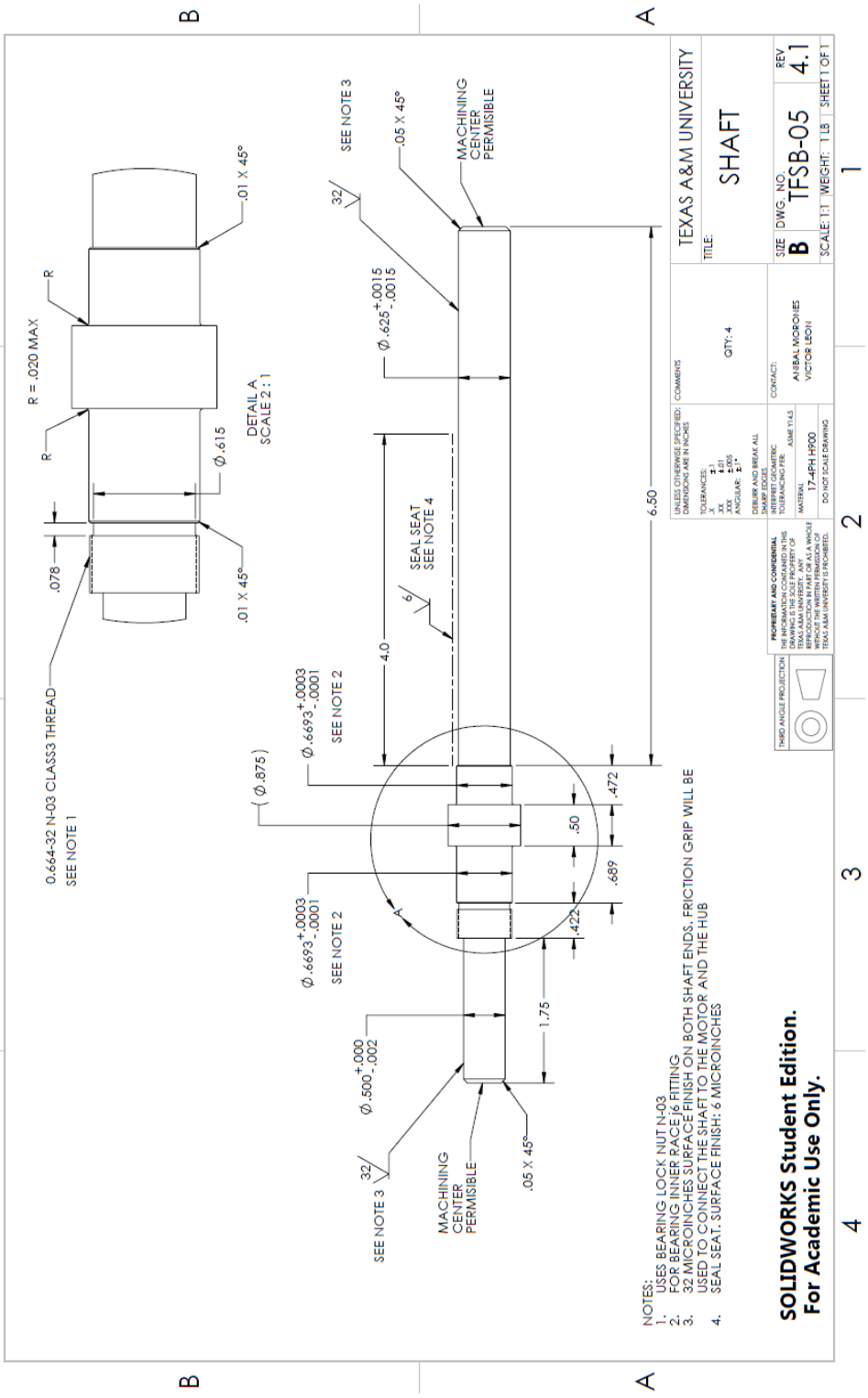
R = .020 MAX
R
R
.078
.01 X 45°
.01 X 45°
Ø.615
DETAIL A
SCALE 2 : 1
0.664-32 N-03 CLASS3 THREAD
SEE NOTE 1
SEE NOTE 3
32
.05 X 45°
MACHINING CENTER PERMISIBLE
Ø.625 +.0015 -.0015
SEE NOTE 3
32
.05 X 45°
MACHINING CENTER PERMISIBLE
SEAL SEAT
SEE NOTE 4
6
4.0
6.50
Ø.6693 +.0003 -.0001
SEE NOTE 2
(Ø.875)
Ø.6693 +.0003 -.0001
SEE NOTE 2
.472
.50
.689
.422
1.75
Ø.500 +.000 -.002
NOTES:
1. USES BEARING LOCK NUT N-03
2. FOR BEARING INNER RACE ¡6 FITTING
3. 32 MICROINCHES SURFACE FINISH ON BOTH SHAFT ENDS. FRICTION GRIP WILL BE USED TO CONNECT THE SHAFT TO THE MOTOR AND THE HUB
4. SEAL SEAT. SURFACE FINISH: 6 MICROINCHES
THIRD ANGLE PROJECTION
PROPRIETARY AND CONFIDENTIAL
THE INFORMATION CONTAINED IN THIS DRAWING IS THE SOLE PROPERTY OF TEXAS A&M UNIVERSITY. ANY REPRODUCTION IN PART OR AS A WHOLE WITHOUT THE WRITTEN PERMISSION OF TEXAS A&M UNIVERSITY IS PROHIBITED.
UNLESS OTHERWISE SPECIFIED:
DIMENSIONS ARE IN INCHES
TOLERANCES:
X ±.1
XX ±.01
XXX ±.005
ANGULAR: ±1°
DEBUR AND BREAK ALL SHARP EDGES
INTERPRET GEOMETRIC TOLERANCING PER: ASME Y14.5
MATERIAL
17-4PH H900
DO NOT SCALE DRAWING
COMMENTS
QTY: 4
CONTACT:
ANIBAL MORONES
VICTOR LEON
TEXAS A&M UNIVERSITY
TITLE:
SHAFT
SIZE B
DWG. NO. TFSB-05
REV 4.1
SCALE: 1:1 WEIGHT: 1 LB SHEET 1 OF 1
SOLIDWORKS Student Edition.
For Academic Use Only.

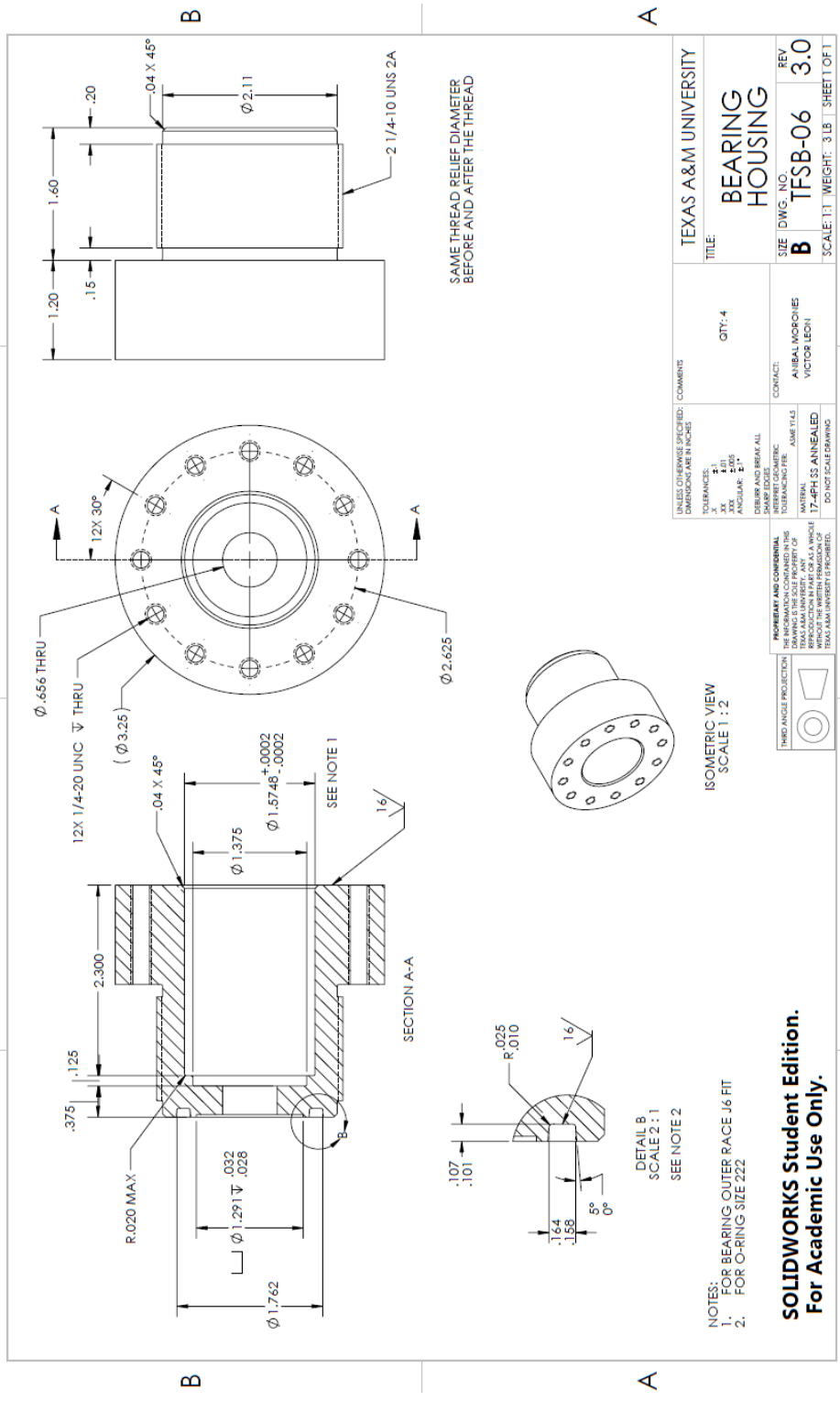
TEXAS A&M UNIVERSITY
BEARING HOUSING
TFSB-06
3.0
SOLIDWORKS Student Edition.
For Academic Use Only.

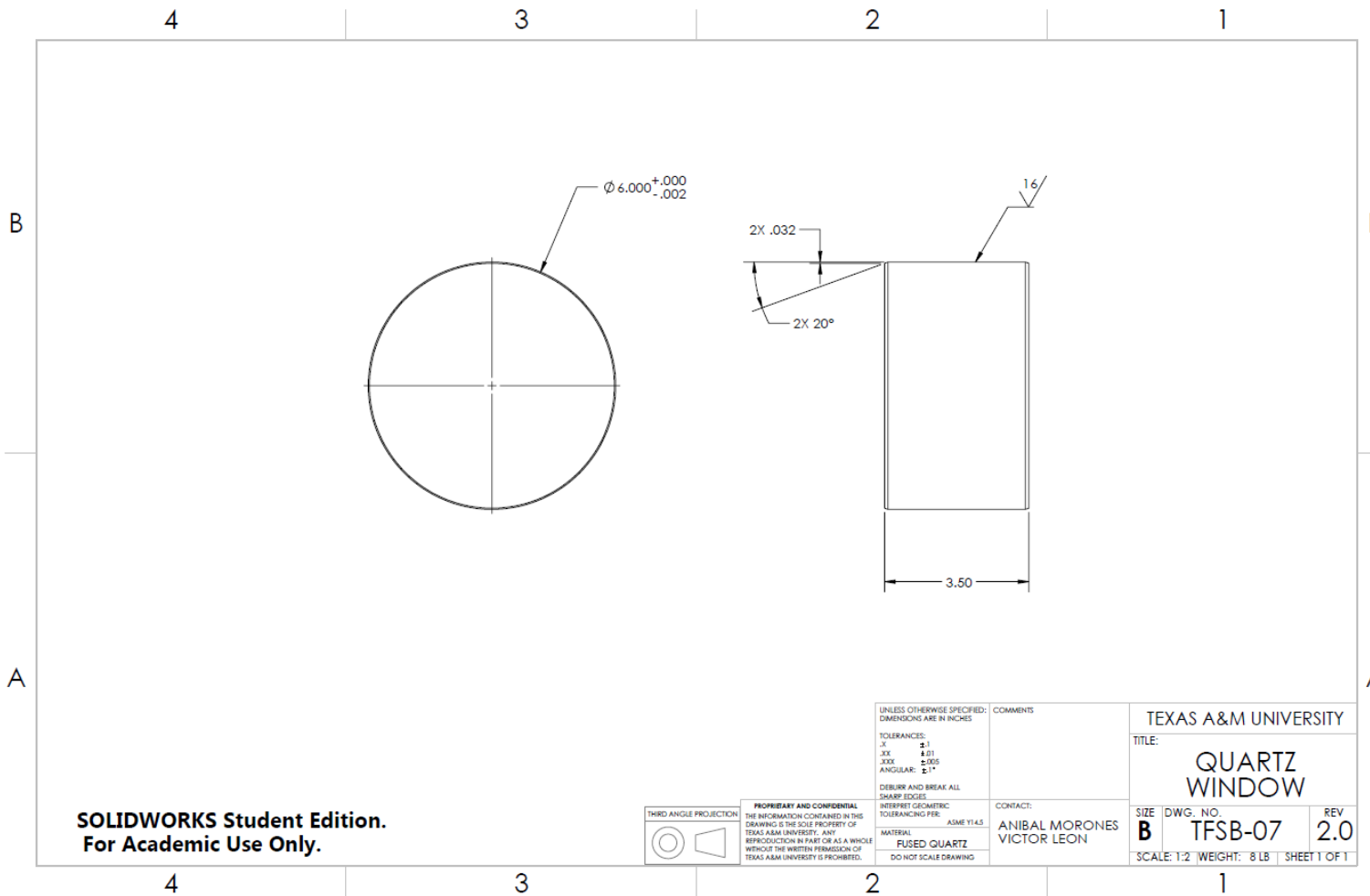
4
3
2
1
B
A
Ø 6.000 +.000 -.002
16
2X .032
2X 20°
3.50
SOLIDWORKS Student Edition.
For Academic Use Only.
UNLESS OTHERWISE SPECIFIED:
DIMENSIONS ARE IN INCHES
TOLERANCES:
.X ±.1
.XX ±.01
.XXX ±.005
ANGULAR: ±.1°
DEBURR AND BREAK ALL SHARP EDGES
INTERPRET GEOMETRIC TOLERANCING PER: ASME Y14.5
MATERIAL
FUSED QUARTZ
DO NOT SCALE DRAWING
COMMENTS
CONTACT:
ANIBAL MORONES
VICTOR LEON
THIRD ANGLE PROJECTION
PROPRIETARY AND CONFIDENTIAL
THE INFORMATION CONTAINED IN THIS DRAWING IS THE SOLE PROPERTY OF TEXAS A&M UNIVERSITY. ANY REPRODUCTION IN PART OR AS A WHOLE WITHOUT THE WRITTEN PERMISSION OF TEXAS A&M UNIVERSITY IS PROHIBITED.
TEXAS A&M UNIVERSITY
TITLE:
QUARTZ WINDOW
SIZE B
DWG. NO. TFSB-07
REV 2.0
SCALE: 1:2
WEIGHT: 8 LB
SHEET 1 OF 1

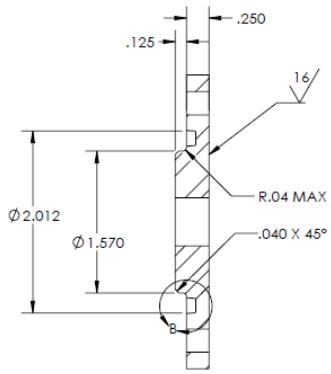

SECTION A-A

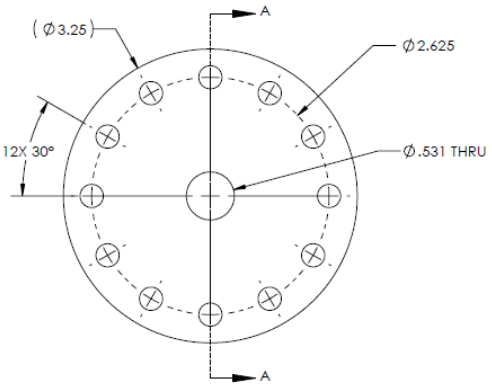

FRONT VIEW

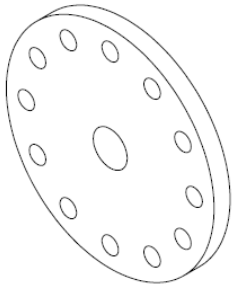

AUXILIARY VIEW (FRONT)

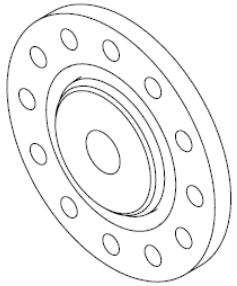

AUXILIARY VIEW (BACK)

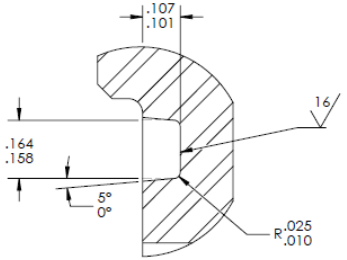

DETAIL B
SCALE 4 : 1
SEE NOTE 1

NOTES:
1. USES O-RING SIZE 224

SOLIDWORKS Student Edition.
For Academic Use Only.

UNLESS OTHERWISE SPECIFIED: DIMENSIONS ARE IN INCHES TOLERANCES: .X ±.1 .XX ±.01 .XXX ±.005 ANGULAR: ±1° DEBURR AND BREAK ALL SHARP EDGES INTERPRET GEOMETRIC TOLERANCING PER: ASME Y14.5 MATERIAL: 304 SS DO NOT SCALE DRAWING	COMMENTS QTY: 4 CONTACT: ANIBAL MORONES VICTOR LEON	TEXAS A&M UNIVERSITY TITLE: HOUSING COVER SIZE B | DWG. NO. TFSB-09 | REV 3.0 SCALE: 1:1 | WEIGHT: .6 LB | SHEET 1 OF 1

THIRD ANGLE PROJECTION

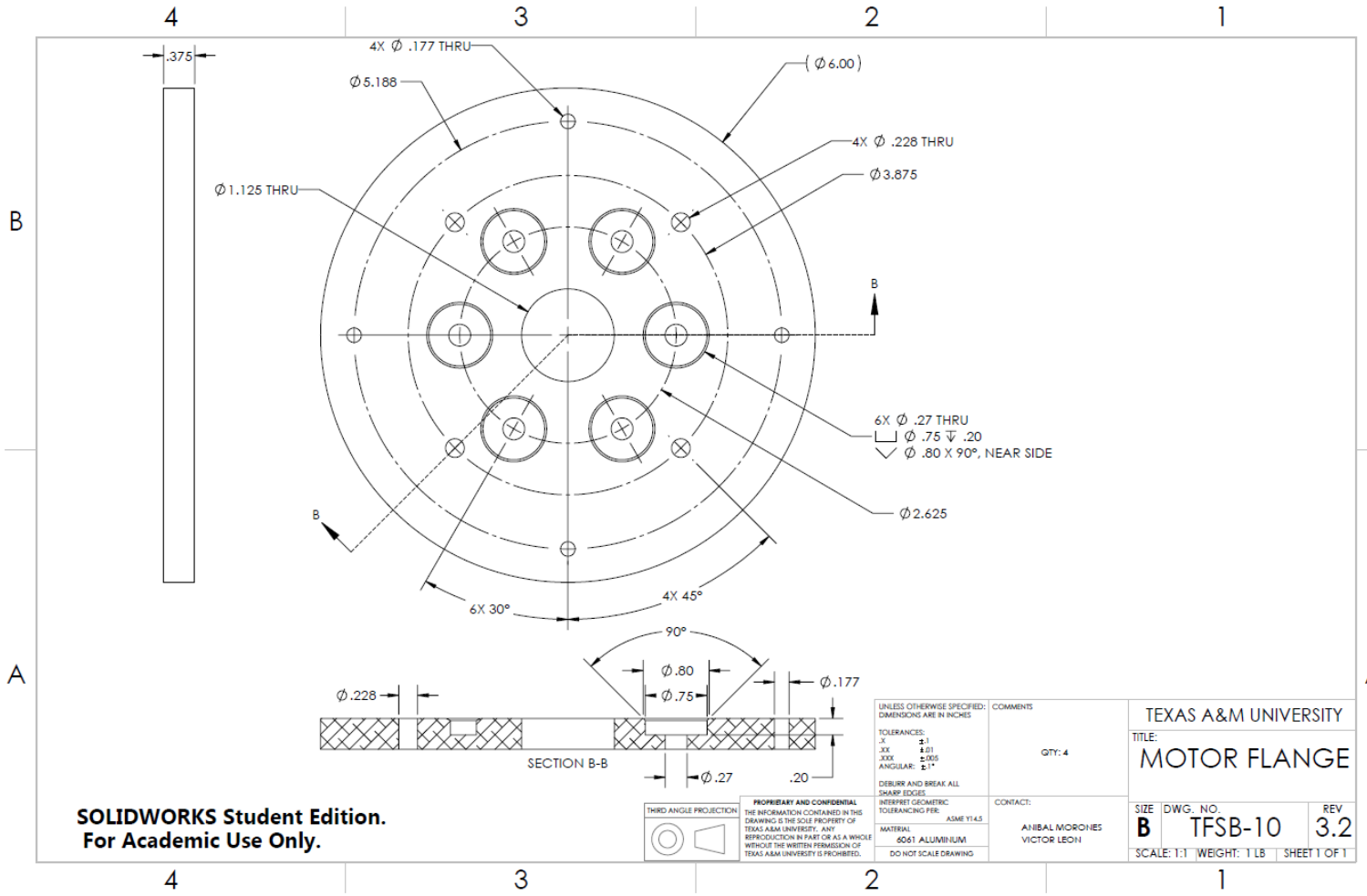
4
3
2
1
B
A
.375
4X Ø .177 THRU
Ø5.188
(Ø6.00)
4X Ø .228 THRU
Ø3.875
Ø1.125 THRU
B
6X Ø .27 THRU
Ø .75 ↧ .20
Ø .80 X 90°, NEAR SIDE
Ø2.625
6X 30°
4X 45°
90°
Ø.80
Ø.75
Ø.177
Ø.228
SECTION B-B
Ø.27
.20
SOLIDWORKS Student Edition.
For Academic Use Only.
THIRD ANGLE PROJECTION
PROPRIETARY AND CONFIDENTIAL
THE INFORMATION CONTAINED IN THIS DRAWING IS THE SOLE PROPERTY OF TEXAS A&M UNIVERSITY. ANY REPRODUCTION IN PART OR AS A WHOLE WITHOUT THE WRITTEN PERMISSION OF TEXAS A&M UNIVERSITY IS PROHIBITED.
UNLESS OTHERWISE SPECIFIED: DIMENSIONS ARE IN INCHES
TOLERANCES:
.X ±.1
.XX ±.01
.XXX ±.005
ANGULAR: ±1°
DEBURR AND BREAK ALL SHARP EDGES
INTERPRET GEOMETRIC TOLERANCING PER: ASME Y14.5
MATERIAL
6061 ALUMINUM
DO NOT SCALE DRAWING
COMMENTS
QTY: 4
CONTACT:
ANIBAL MORONES
VICTOR LEON
TEXAS A&M UNIVERSITY
TITLE:
MOTOR FLANGE
SIZE B
DWG. NO. TFSB-10
REV 3.2
SCALE: 1:1
WEIGHT: 1 LB
SHEET 1 OF 1

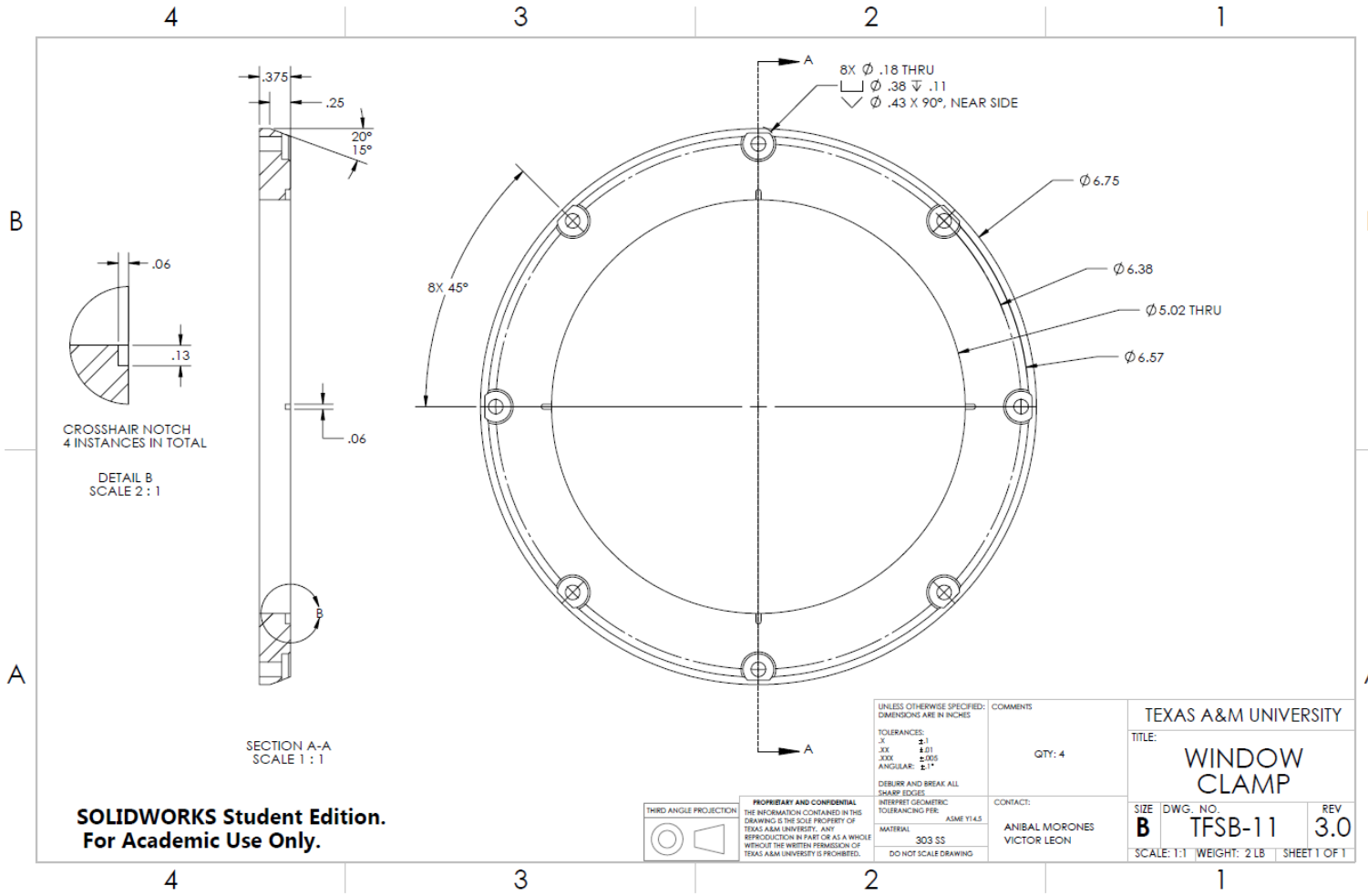
4
3
2
1
B
A
.375
.25
20°
15°
.06
.13
CROSSHAIR NOTCH
4 INSTANCES IN TOTAL
DETAIL B
SCALE 2 : 1
.06
B
SECTION A-A
SCALE 1 : 1
A
8X Ø .18 THRU
Ø .38 ↧ .11
Ø .43 X 90°, NEAR SIDE
8X 45°
Ø6.75
Ø6.38
Ø5.02 THRU
Ø6.57
A
SOLIDWORKS Student Edition.
For Academic Use Only.
UNLESS OTHERWISE SPECIFIED:
DIMENSIONS ARE IN INCHES
TOLERANCES:
.X ±.1
.XX ±.01
.XXX ±.005
ANGULAR: ±1°
DEBURR AND BREAK ALL SHARP EDGES
INTERPRET GEOMETRIC TOLERANCING PER: ASME Y14.5
MATERIAL
303 SS
DO NOT SCALE DRAWING
COMMENTS
QTY: 4
CONTACT:
ANIBAL MORONES
VICTOR LEON
THIRD ANGLE PROJECTION
PROPRIETARY AND CONFIDENTIAL
THE INFORMATION CONTAINED IN THIS DRAWING IS THE SOLE PROPERTY OF TEXAS A&M UNIVERSITY. ANY REPRODUCTION IN PART OR AS A WHOLE WITHOUT THE WRITTEN PERMISSION OF TEXAS A&M UNIVERSITY IS PROHIBITED.
TEXAS A&M UNIVERSITY
TITLE:
WINDOW CLAMP
SIZE B
DWG. NO. TFSB-11
REV 3.0
SCALE: 1:1
WEIGHT: 2 LB
SHEET 1 OF 1

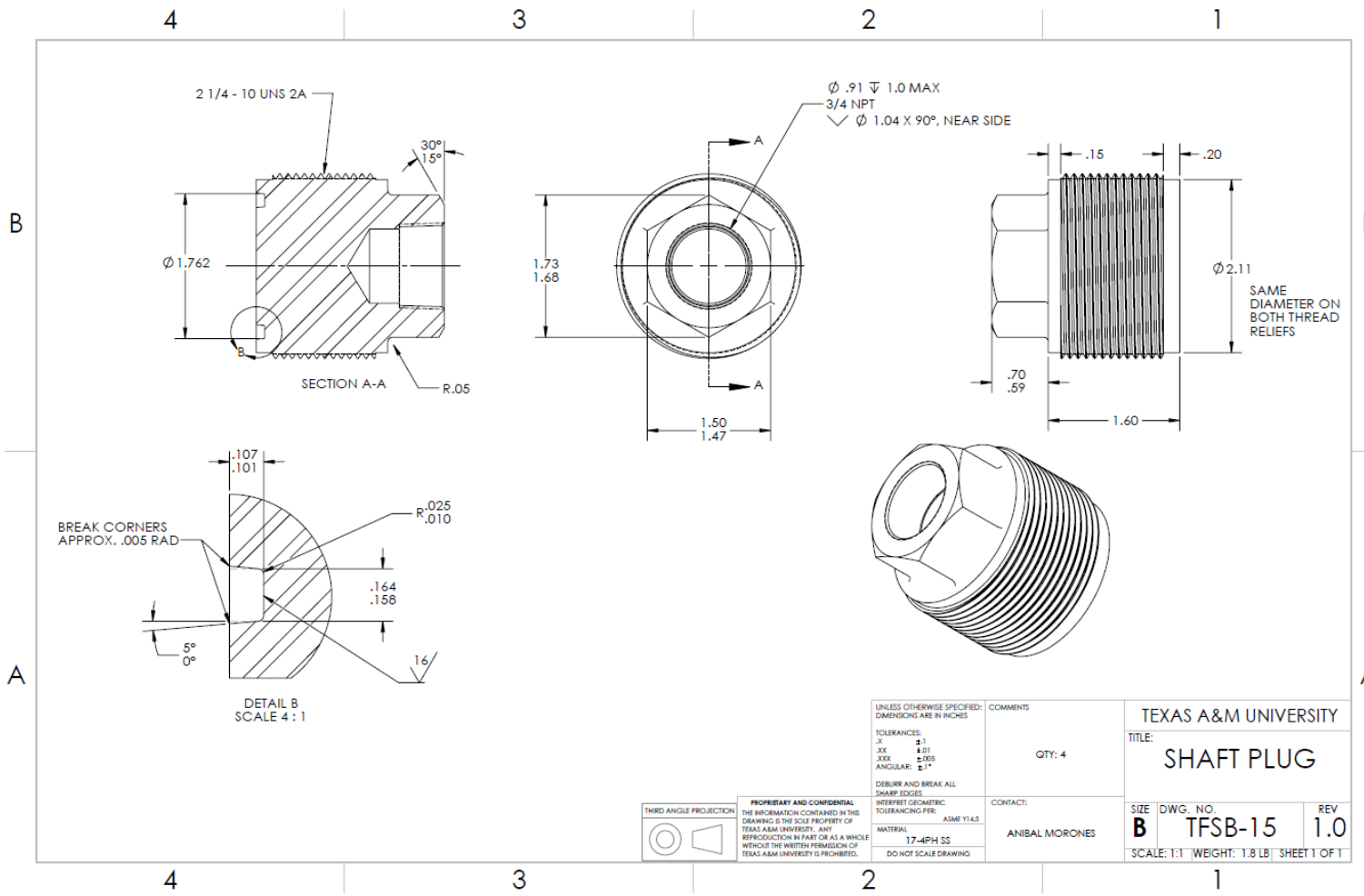
4
3
2
1
B
A
2 1/4 - 10 UNS 2A
30°
15°
Ø1.762
B
SECTION A-A
R.05
Ø .91 ↧ 1.0 MAX
3/4 NPT
Ø 1.04 X 90°, NEAR SIDE
A
1.73
1.68
A
1.50
1.47
.15
.20
Ø2.11
SAME DIAMETER ON BOTH THREAD RELIEFS
.70
.59
1.60
.107
.101
BREAK CORNERS APPROX. .005 RAD
R.025
.010
.164
.158
5°
0°
16
DETAIL B
SCALE 4 : 1
UNLESS OTHERWISE SPECIFIED: DIMENSIONS ARE IN INCHES
TOLERANCES:
.X ±.1
.XX ±.01
.XXX ±.005
ANGULAR: ±1°
DEBURR AND BREAK ALL SHARP EDGES
INTERPRET GEOMETRIC TOLERANCING PER: ASME Y14.5
MATERIAL: 17-4PH SS
DO NOT SCALE DRAWING
COMMENTS
QTY: 4
CONTACT:
ANIBAL MORONES
THIRD ANGLE PROJECTION
PROPRIETARY AND CONFIDENTIAL
THE INFORMATION CONTAINED IN THIS DRAWING IS THE SOLE PROPERTY OF TEXAS A&M UNIVERSITY. ANY REPRODUCTION IN PART OR AS A WHOLE WITHOUT THE WRITTEN PERMISSION OF TEXAS A&M UNIVERSITY IS PROHIBITED.
TEXAS A&M UNIVERSITY
TITLE:
SHAFT PLUG
SIZE B
DWG. NO. TFSB-15
REV 1.0
SCALE: 1:1
WEIGHT: 1.8 LB
SHEET 1 OF 1

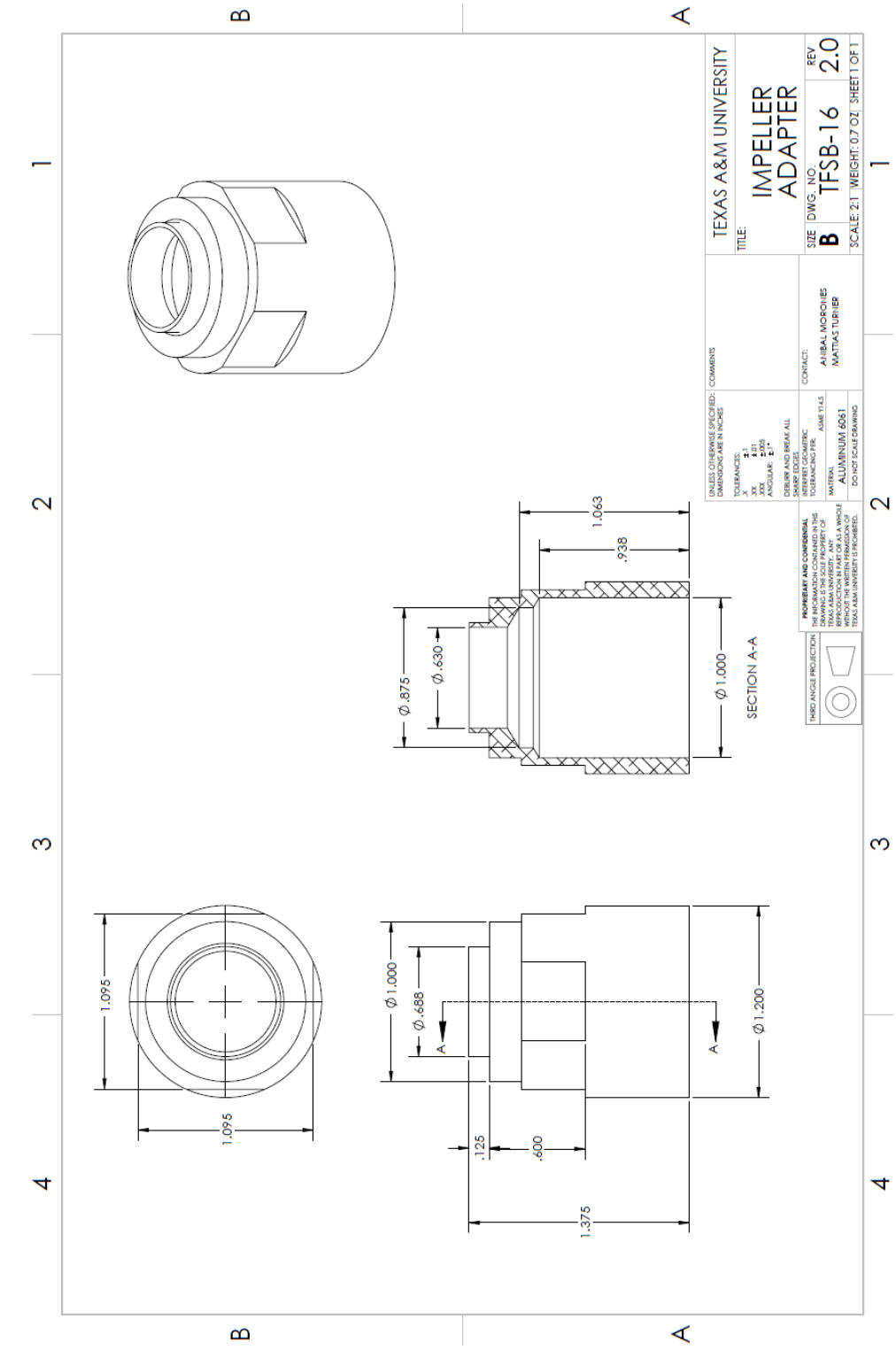
TEXAS A&M UNIVERSITY
IMPELLER ADAPTER
SIZE B
DWG. NO. TFSB-16
REV 2.0
SCALE: 2:1 WEIGHT: 0.7 OZ SHEET 1 OF 1
1.095
1.095
Ø1.000
Ø.688
.125
.600
1.375
Ø1.200
Ø.875
Ø.630
1.063
.938
Ø1.000
SECTION A-A